Title
Application-Tailored Accelerated Magnetic Resonance Imaging Methods

Author
Zhou, Ziwu

Publication Date
2018

Peer reviewed|Thesis/dissertation

UNIVERSITY OF CALIFORNIA

Los Angeles

Application-Tailored Accelerated Magnetic Resonance Imaging Methods

A dissertation submitted in partial satisfaction of the

requirements for the degree Doctor of Philosophy

in Bioengineering

by

Ziwu Zhou

2018

ABSTRACT OF THE DISSERTATION

Application-Tailored Accelerated Magnetic Resonance Imaging Methods

by

Ziwu Zhou

Doctor of Philosophy in Bioengineering

University of California, Los Angeles, 2018

Professor Peng Hu, Co-Chair

Professor Daniel B. Ennis, Co-Chair

Magnetic resonance imaging (MRI) is a powerful diagnostic medical imaging technique that provides very high spatial resolution. By manipulating the signal evolution through careful imaging sequence design, MRI can generate a wide range of soft-tissue contrast unique to individual application. However, imaging speed remains an issue for many applications. In order to increase scan output without compromising the image quality, the data acquisition and image reconstruction methods need to be designed to fit each application to achieve maximum efficiency. This dissertation concerns several application-tailored accelerated imaging methods through improved sequence design, efficient k-space traverse, as well as tailored image reconstruction algorithm, all together aiming to exploit the full potential of data acquisition and image reconstruction in each application.

The first application is ferumoxtyol-enhanced 4D multi-phase cardiovascular MRI on pediatric patients with congenital heart disease. By taking advantage of the high signal-to-

noise ratio (SNR) results from contrast enhancement, we introduced two methods to improve the scan efficiency with maintained clinical utility: one with reduced scan time and one with improved temporal resolution. The first method used prospective Poisson-disc under-sampling in combination with graphics processing unit accelerated parallel imaging and compressed sensing combined reconstruction algorithm to reduce scan time by approximately 50% while maintaining highly comparable image quality to un-accelerated acquisition in a clinically practical reconstruction time. The second method utilized a motion weighted reconstruction technique to increase temporal resolution of acquired data, and thus permits improved cardiac functional assessment. Compared with existing acceleration method, the proposed method has nearly three times lower computation burden and six times faster reconstruction speed, all with equal image quality.

The second application is noncontrast-enhanced 4D intracranial MR angiography with arterial spin labeling (ASL). Considering the inherently low SNR of ASL signal, we proposed to sample k-space with the efficient golden-angle stack-of-stars trajectory and reconstruct images using compressed sensing with magnitude subtraction as regularization. The acquisition and reconstruction strategy in combination produces images with detailed vascular structures and clean background. At the same time, it allows a reduced temporal blurring delineation of the fine distal arteries when compared with the conventional k-space weighted image contrast (KWIC) reconstruction. Stands upon on this, we further developed an improved stack-of-stars radial sampling strategy for reducing streaking artifacts in general volumetric MRI. By rotating the radial spokes in a golden angle manner along the partition-encoding direction, the aliasing pattern due to under-sampling is modified,

resulting in improved image quality for gridding and more advanced reconstruction methods.

The third application is low-latency real-time imaging. To achieve sufficient frame rate, real-time MRI typically requires significant k-space under-sampling to accelerate the data acquisition. At the same time, many real-time application, such as interventional MRI, requires user interaction or decision making based on image feedback. Therefore, low-latency on-the-fly reconstruction is highly desirable. We proposed a parallel imaging and convolutional neural network combined image reconstruction framework for low-latency and high quality reconstruction. This is achieved by compacting gradient descent steps resolved from conventional parallel imaging reconstruction as network layers and interleaved with convolutional layers in a general convolutional neural network. Once all parameters of the network are determined during the off-line training process, it can be applied to unseen data with less than 100ms reconstruction time per frame, while more than 1s is usually needed for conventional parallel imaging and compressed sensing combined reconstruction.

The dissertation of Ziwu Zhou is approved.

John Paul Finn

Michael Albert Thomas

Kyung Hyun Sung

Danny Jiong Jiong Wang

Daniel B. Ennis, Committee Co-Chair

Peng Hu, Committee Co-Chair

University of California, Los Angeles

2018

TABLE OF CONTENT

LIST OF FIGURES

LIST OF TABLES

ACKNOWLEDGEMENTS

First of all, I would like my advisor, Professor Peng Hu, who provide support, guidance as well as mentorship for the past five years of my Ph.D. journey. I cannot be who I am now without him being as a role model, showing how to approach research and life in such an intellectual, charismatic, and more crucially balance way. He not only demonstrates me correct ways to solve open-ended research questions, but also passes me the right angle to tackle challenges elegantly. No matter how busy he is, he always greets me with smile and warming welcome in the office whenever I need his help. Following the old Chinese proverb, Peng just like my father as my mentor.

Besides Professor Peng, I feel so lucky that I can join Dr. Paul Finn's clinical-oriented research team. His day-to-day actions clearly shows me how our research can benefit the patients' healthcare in such a profound way. Furthermore, his insights pave the way for my technical development, even if there is no direct application of it during the developing stage. Dr. Paul Finn uses his wisdom and foresight to help me grow during my Ph.D. study. I cannot imagine a better guidance that I would receive.

I would also like to extend my appreciation to my thesis committee, Professor Daniel Ennis, Professor Kyun Hyun Sung, Professor Thomas Albert, Professor Danny JJ Wang, as well as other faculties in UCLA, Professor Holden Wu, Dr. Kim-Lien Nguyen, Professor Yingli Yang, Professor Mingsong Cao, and Professor Wotao Yin. Their support and help throughout my Ph.D. study shape the framework of this thesis and generate numerous interesting discussions that I would benefit from even after my Ph.D. study.

It has been my pleasure to work with all the current and past members of Magnetic Resonance Research Lab (MRRL) at UCLA: Take, Jiaxin, Da, Shams, Vahid, Fadil, Yu, Matt, Suba, Zhe, Eric, Patrick, Mike, Kevin, Jessica, Novena, Isabel, Luigi, Lirong, Andres, Tess, Xinran and Jiahao. I would like to specially thank Dr. Stanislas Rapacchi, who was the most senior postdoc when I came to UCLA as a summer exchange student in Dr. Peng lab. Although I'm not an official member of the lab, Stan still provide numerous first-class introduction on MRI, especially on MR reconstruction to me. His enthusiasm about research and his love of life have had profound influences of my Ph.D. life and beyond. It is also an amazing experience to work closely with Fei Han, who is the most senior Ph.D. student in the lab. We spent countless late-nights or over-nights at research center and hospital, debugging the sequence, playing around with the scanner, and exchanging thoughts on random problems. In addition, our intersections on personal life made my study abroad extremely colorful.

Above all, this thesis and my PhD study would not have been possible without the continuous understanding and encouragement from my parents and my girlfriend, who share the happiness and suffer the bitterness together with me along the journey. It is their unchanged support that strengthens my willingness to take challenges one and another in my research. The fact that I can always have their back allows me to run freely and pursue the very purest dream of my research. More than I can admit, this thesis is co-authored with them, my beloved family and girlfriend. I dedicate this thesis to them, with my pride and affection.

Vita

Education:

- Ph.D. Candidate, Bioengineering, University of California, Los Angeles, CA (2013-18)
- B.S., Electrical Engineering, University of Science and Technology of China, China (2009-13)

Experience:

- Graduate Student Researcher, Hu Lab, Department of Radiological Sciences, University of California, Los Angeles, CA, 2013-present
- MR Physcist & Engineer Intern, ViewRay, Inc., Mountain View, CA, summer 2017

Awards:

- Potchen Award, Society of Magnetic Resonance Angiography, 2015
- Abstract Award, Cardiac Study Group, ISMRM annual meeting, 2015
- Magna Cum Laude Merit Award, 24th ISMRM annual meeting, 2016
- Student Stipend, ISMRM annual meeting, 2015-2017

Publications:

Journal Articles

- **Zhou Z**, Han F, Rapacchi S, Nyugen KL, Brunengraber DZ, Finn JP, Hu P. (2016), Accelerated Ferumoxytol- Enhanced 4D Multi-phase Steady State Imaging with Contrast Enhancement (MUSIC) Cardiovascular MRI: Validation in Pediatric Congenital Heart Disease, NMR in Biomedicine. doi: 10.1002/nbm.3663

- **Zhou Z**, Han F, Yan L, Wang D, Hu P. (2016), Golden-Ratio Rotated Stack-of-Stars Acquisition for Improved Volumetric MRI, Magn Reson Med. doi: 10.1002/mrm.26625

- **Zhou Z**, Han F, Yu S, Yu D, Rapacchi S, Song HK, Wang D, Hu P, Yan L. (2017), Accelerated Noncontrast-Enhanced 4-Dimensional Intracranial MR Angiography Using Golden-Angle Stack-of-Stars Trajectory and Compressed Sensing with Magnitude Subtraction, Magn Reson Med. doi: 10.1002/mrm.26747

- Han F, **Zhou Z**, Han E, Gao Y, Nguyen KL, Finn JP, Hu P. (2016), Self-gated 4D multiphase, steady-state imaging with contrast enhancement (MUSIC) using rotating cartesian K-space (ROCK): Validation in children with congenital heart disease, Magn Reson Med. doi: 10.1002/mrm.26376

- Han F, **Zhou Z**, Rapacchi S, Nguyen KL, Finn JP, Hu P. (2015), Segmented golden ratio radial reordering with variable temporal resolution for dynamic cardiac MRI. Magn Reson Med. doi: 10.1002/mrm.25861

- Han F, **Zhou Z**, Cao M, Yang Y, Sheng K, Hu P. (2016), Respiratory motion resolved, self-gated, 4D-MRI using Rotating Cartesian K-space (ROCK). Medical Physics. doi: 10.1002/mp.12139

- Gao Y, Han F, **Zhou Z**, Cao M, Kaprealian T, Kamrava M, Wang C, Neylon J, Low DA, Yang Y, Hu Peng. (2017), Distortion-Free Diffusion MRI using an MRI-Guided Tri-Cobalt 60 Radiotherapy System: Sequence Verification and Preliminary Clinical Experience. Medical Physics. doi: 10.1002/mp.12465

- Nyugen KL, Han F, **Zhou Z**, Brunengraber DZ, Ayad I, Levi DS, Satou GM, Reemtsen BL, Hu P, Finn JP. (2017), 4D MUSIC CMR: value-based imaging of neonates and infants with congenital heart disease. J Cardiovasc Magn Reson. 2017;19-40.

- Finn JP, Nyugen KL, Han F, **Zhou Z**, Salusky I, Ayad I, Hu P, (2016), Cardiovascular MRI using Ferumoxytol. Clinical Radiology, 71(8), 796-806

- Dregely I, Margolis DAJ, Sung K, **Zhou Z**, Rangwala N, Raman SS, and Wu HH, (2016), Rapid Quantitative T2 Mapping of the Prostate using Three-Dimensional Dual Echo Steady State MRI at 3T. Magn Reson Med, doi: 10.1002/mrm.26053

Chapter 1 Introduction

Magnetic Resonance Imaging (MRI) is a powerful medical imaging technique that provides rich source of diagnostic information. It has several advantages over some of other existing medical imaging modalities. For example, unlike modalities such as X-ray computed tomography (CT) or positron emission tomography (PET), MRI does not require the use of ionizing radiation. In addition, the sensitivity of MR signal to a wide range of physical behavior and the flexibility of MRI allows the generation of images with various tissue contrast through careful manipulation of intrinsic and extrinsic contrast mechanism. As a result, MRI is a compelling choice for clinical practice that can enable early detection of pathology, quantitative assessment of biological parameters, and even disclosure of functional changes in depth.

Despite its huge potential, imaging speed remains a major challenge of many MRI applications to be adapted in clinical environment. The number of measured data points in MRI is usually controlled by several factors, mainly the imaging duration, spatial/temporal resolution, image signal-to-noise ratio (SNR). In practice, there is always trade-offs between these factors. For example, images with higher spatial/temporal resolution would require extended Fourier encoding steps, which translates to a higher number of data points to be sampled. Similarly, images with higher SNR would require data averaging as the conventional strategy to reduce the effect of additive noise, which equally results in more data points. On the other hand, sample a small number of data points could drastically reduce the total acquisition time, or lead to increased temporal resolution in dynamic imaging application given a fixed imaging time.

The problem of recovering high quality images from inadequate sampled data points, which is usually too small to generate acceptable reconstruction using conventional inverse Fourier transform, has been studying for decades. Starting from late 90s, parallel imaging techniques (1–4), which utilized localized coil arrays with multiple receiver coils to provide additional encoding information in the image domain, were proposed to reconstruct under-sampled spatial-frequency domain (k-space) data. Later on in mid 00s, by implicitly compresses data within the signal acquisition process through obtaining fewer so-called incoherent measurements and then reconstructing the underlying images with iterative methods, compressed sensing (5,6) was successfully applied in MRI to further reduce acquisition time. However, these acceleration methods are mainly designed for general MR imaging application, despite the benefits and achievements of them shown in research development. For individual application that has unique contrast feature, uncommon signal level, or special requirement, most of these methods may not be able to reach full potential that allows a higher spatial/temporal resolution, better SNR or scan efficiency to be achieved.

Based upon previously described acceleration methods, this dissertation describes several application-tailored accelerated MRI methods that aims at exploiting the full potential of data acquisition and image reconstruction in each application through improved sequence design, efficient k-space traverse, as well as tailored image reconstruction algorithm. Specifically, approaches to accelerate three applications: 1). ferumoxtyol-enhanced 4D multi-phase cardiovascular MRI on pediatric patients with congenital heart disease; 2). noncontrast-enhanced 4D intracranial MR angiography with arterial spin labeling (ASL); and 3). low-latency real-time MR imaging were investigated.

These approaches are designed in such a way that signal characteristics or special application requirements were fully considered in the data acquisition and image reconstruction stages for each application. Furthermore, the feasibility of clinical usage of each acceleration method is well evaluated in implementation stage.

1.1 Outline

The structure of this dissertation is as follows:

Chapter 2: Principles of Magnetic Resonance Imaging

This chapter describes the principles of nuclear magnetic resonance and the concepts behind MR imaging. Widely used imaging trajectory (Cartesian and non-Cartesian) and accelerated imaging methods (parallel imaging, compressed sensing and deep learning) are also introduced to pertain to the rest of this dissertation.

Chapter 3: Accelerated 4D-MUSIC

Ferumoxytol-enhanced 4D multi-phase steady-state imaging with contrast enhancement (4D-MUSIC), using 7-10 minutes acquisition, allows superior delineation of both extra- and intra-cardiac structures compared with conventional first-pass contrast-enhanced MR angiography or 2D multi-slice cardiac cine imaging. This chapter introduces a clinical practical, graphics processing unit accelerated, compressed sensing and parallel imaging combined reconstruction method for 4D-MUSIC. Qualitative and quantitative comparison of the accelerated 4D-MUSIC and original 4D MUSIC were performed on 13 pediatric patients. This work has been published as a journal article (7).

Chapter 4: Motion Weighted 4D-MUSIC for Improved Functional Assessment

The original 4D-MUSIC and accelerated 4D-MUSIC introduced in chapter 3 allow incomparable clear and detailed examination of cardiac and vascular anatomy, but they fail to provide sufficient temporal phases for comprehensive cardiac functional assessment including volume calculation and wall motion evaluation. This chapter describes a motion weighted reconstruction strategy to allow doubled cardiac phases reconstructed based on the same dataset and within the same reconstruction time of original 4D-MUSIC. The image sharpness and left ventricle volume measurement results from a retrospective clinical study on 12 pediatric patients were presented.

Chapter 5: Accelerated Noncontrast-enhanced MR Angiography

Non–contrast enhanced dynamic MR angiography with arterial spin labeling (ASL) has become a promising approach for detailed characterization of intracranial dynamic flow patterns, because of its completely noninvasive nature. However, the inherently low SNR of ASL signal prevents high quality reconstruction from highly under-sampled data using conventional parallel imaging or compressed sensing reconstruction. This chapter presents a solution that uses golden-angle stack-of-stars acquisition in combination with magnitude subtraction regularized reconstruction for accelerated noncontrast-enhanced dynamic MR angiography. Both the spatial and temporal behavior of the proposed method were studied using 6 volunteer and 1 patient data. This work has been published as a journal article (8).

Chapter 6: Golden-ratio Rotated Stack-of-Stars

The conventional golden-angle stack-of-stars trajectory used in chapter 5 collects the same radial angle for every partition (slice) encoding. In an under-sampled acquisition, such an aligned acquisition generates coherent aliasing patterns and introduces strong

streaking artifacts 3D image domain. This chapter demonstrates an improved volumetric imaging method using stack-of-stars trajectory by simply rotating the radial spokes in a golden-angle manner along the partition-encoding direction. Computer simulations were performed and phantom as well as in vivo images for three different exemplary applications were acquired to show the efficacy of the proposed method. This work has been published as a journal article (9).

Chapter 7: Parallel Imaging and Convolutional Neural Network Combined Low-Latency Reconstruction for Real-Time Imaging

Real-time MRI is a powerful tool to assess physiological processes noninvasively at high temporal resolution. To achieve sufficient frame rate, it typically requires significant k-space under-sampling to accelerate the data acquisition. At the same time, many real-time application, such as interventional MRI, requires user interaction or decision making based on image feedback. This chapter introduces a parallel imaging and convolutional neural network combined image reconstruction framework for low-latency and high quality reconstruction. Cardiac and abdominal imaging on both high (3.0 T) and low (1.5 T) fields were demonstrated in comparison with clinical available linear reconstruction and more advanced non-linear compressed sensing based reconstruction.

Chapter 8: Summary and Future Work

The acceleration methods for different applications presented in this dissertation is summarized in this chapter. Also, potential directions for future research are briefly explored.

Chapter 2 Background

Magnetic resonance imaging is a medical imaging application based on the quantum mechanical phenomenon known as nuclear magnetic resonance (NMR). The discovery of NMR and its development to MRI were marked by several milestone in the history of science, including Felix Bloch and Edward M. Purcell, who shared the 1952 Nobel Prize in Physics for the discovery of NMR phenomenon, Paul C. Lauterbur, who was awarded the 2003 Nobel Prize in Physiology and Medicine for the introduction of spatial encoding using gradients, and Sir Peter Mansfield, who was also awarded the 2003 Nobel Prize in Physiology and Medicine for the mathematical description of MR imaging physics. Given its complexity, a full explanation of magnetic resonance phenomenon often requires a quantum mechanism description. In this chapter, we adopt a semi-classical high-level description of the basic principles of MR physics, and then the system model with Fourier encoding will be described to facilitate the introduction of image generation process in MRI. Moreover, more sophisticated encoding methods such as non-Cartesian imaging, and more advanced accelerated imaging methods such as parallel imaging, compressed sensing, and deep learning are reviewed. For more detailed description of MRI, the reader is referred to (10,11).

2.1 Nuclear Magnetic Resonance Physics

Atoms with odd atomic weighs (i.e. protons/neutrons) process a nuclear angular momentum, which can be modeled as spinning magnetic dipoles with a magnetic moment. Therefore, they are also called the “spins”. The single-proton hydrogen atom (^1H) is the most widely studied atom because of its sensitivity and abundance in human body as H_2O.

The spins take random directions at thermal equilibrium, resulting in zero net magnetization in a macroscopic view. In the presence of a strong external magnetic field $\boldsymbol{B_0}$ (main magnetic field), the spins are polarized and lined up in parallel and anti-parallel directions with respect to the main magnetic field, and with a slight excess in parallel. This generates a net magnetic moment $\boldsymbol{M_0}$ that is proportional to $\boldsymbol{B_0}$. Meanwhile, the spins precess at a well-defined frequency proportional to the applied $\boldsymbol{B_0}$:

$$\omega_0 = \gamma \boldsymbol{B_0} \qquad (2\text{-}1)$$

, where γ is the gyromagnetic ratio that is constant for a specific atom and ω_0 is known as the Larmor frequency.

A macroscopic bulk magnetic moment measured from a group of spins is described with a magnetization vector $\overrightarrow{\boldsymbol{M}} = (\boldsymbol{M_x}, \boldsymbol{M_y}, \boldsymbol{M_z})$. Its interaction with an external magnetic field $\boldsymbol{B}$, which comprised of the longitudinal and transverse components to the static magnetic fields, is phenomenologically governed by the Bloch equation:

$$\frac{d\boldsymbol{M}}{dt} = \boldsymbol{M} \times \gamma \boldsymbol{B} - \frac{\boldsymbol{M_z} - \boldsymbol{M_0}}{T_1} - \frac{\boldsymbol{M_{xy}}}{T_2} \qquad (2\text{-}2)$$

, where $\boldsymbol{M_{xy}} = (\boldsymbol{M_x}\vec{\boldsymbol{\imath}} + \boldsymbol{M_y}\vec{\boldsymbol{\jmath}})$ and $\boldsymbol{M_z}$ are defined as the transverse and longitudinal magnetization, respectively.

At thermal equilibrium state, the bulk magnetization $\overrightarrow{\boldsymbol{M}} = (\boldsymbol{0}, \boldsymbol{0}, \boldsymbol{M_0})$ aligns with $\boldsymbol{B_0}$. It can be perturbed by a radiofrequency (RF) magnetic field $\boldsymbol{B_1}$ that is tuned to ω_0 and perpendicular to the static $\boldsymbol{B_0}$ field. $\boldsymbol{B_1}$ will rotate $\overrightarrow{\boldsymbol{M}}$ into the transverse plane and being "excited". The tipped magnetization $\overrightarrow{\boldsymbol{M}}$ will continue to precess about $\boldsymbol{B_0}$ field, with its longitudinal magnetization component $\boldsymbol{M_z}$ recovers to its equilibrium state $\boldsymbol{M_0}$ with T_1,

and transverse magnetization component $\boldsymbol{M_{xy}}$ decays with T_2. The precession of $\overrightarrow{\boldsymbol{M}}$, also known as "free precession", results in a changing transverse magnetic field, which by Farady's Law, induces a measurable voltage in a coil element that is recorded as the MR signal. The recovery of longitudinal magnetization component with T_1 and decay of transverse magnetization component with T_2, together called "relaxation", generates the mechanism for tissue contrast, since each individual tissue exhibits different T_1 and T_2 relaxation constant.

2.2 Imaging Basics

As mentioned in the above section, measureable voltage in the coil element will be recorded as MR signal. However, the received signal is a cumulative signal from the entire imaging volume. In order to differentiate the magnetization from each spatial location $\vec{\boldsymbol{x}} = (\boldsymbol{x}, \boldsymbol{y}, \boldsymbol{z})$, an additional spatially varying magnetic field is required to spatially encode the MR signal, which permits an important task of modern MRI system: localization. Specifically, this is achieved by an additional 3D spatial variant, longitudinal linear magnetic field, $\vec{\boldsymbol{G}} = \left(\boldsymbol{G_x}, \boldsymbol{G_y}, \boldsymbol{G_z}\right)$, which is superimposed on the static $\boldsymbol{B_0}$ field. It makes the effective field, $\boldsymbol{B}(\boldsymbol{x}) = \boldsymbol{B_0} + \vec{\boldsymbol{G}} \cdot \vec{\boldsymbol{x}}$, a linear function of the spatial location. As a result, the precession frequency of $\overrightarrow{\boldsymbol{M}}$ also varies with $\boldsymbol{x}$ allowing for spatial information to be extracted.

Let $\boldsymbol{m}(\vec{\boldsymbol{x}})$ be the volume of interest. With the spatially-dependent field that alters the rate of precession of each magnetic dipole, received MR signal can be described as follows after de-modulation by ω_0:

$$s(t) = \int \boldsymbol{m}(\vec{\boldsymbol{x}}) exp\,(-i\omega(\vec{\boldsymbol{x}}, t))\, d\vec{\boldsymbol{x}} \qquad (2\text{-}3)$$

Spatially varying phase $\omega(\vec{\boldsymbol{x}}, t)$ corresponds to the net precession of each dipole, and can be calculated as:

$$\omega(\vec{x}, t) = \int_{t1}^{t2} \gamma \vec{G}(\tau) \cdot \vec{x} d\tau = 2\pi(\boldsymbol{k_x}(t)x + \boldsymbol{k_y}(t)y + \boldsymbol{k_z}(t)z) \qquad (2\text{-}4)$$

, where $\boldsymbol{k_x}(t), \boldsymbol{k_y}(t), \boldsymbol{k_z}(t)$ are the time integrals of the gradient waveforms:

$$\boldsymbol{k_x}(t) = \frac{\gamma}{2\pi} \int_{t1}^{t2} \boldsymbol{G}_x(\tau)\, d\tau \qquad (2\text{-}5)$$

$$\boldsymbol{k_y}(t) = \frac{\gamma}{2\pi} \int_{t1}^{t2} \boldsymbol{G}_y(\tau)\, d\tau \qquad (2\text{-}6)$$

$$\boldsymbol{k_z}(t) = \frac{\gamma}{2\pi} \int_{t1}^{t2} \boldsymbol{G}_z(\tau)\, d\tau \qquad (2\text{-}7)$$

$\boldsymbol{G_x}(\boldsymbol{t}), \boldsymbol{G_y}(\boldsymbol{t}), \boldsymbol{G_z}(\boldsymbol{t})$ are time varying magnetic gradients, $t1$ is the time right after excitation and $t2$ is the time of data acquisition. Denote $\vec{\boldsymbol{k}}(t) = (\boldsymbol{k_x}(t), \boldsymbol{k_y}(t), \boldsymbol{k_z}(t))$, which are spatial frequencies, Equation (2-3) can be formulated as:

$$s(t) = \int \boldsymbol{m}(\vec{\boldsymbol{x}}) exp\,(-i2\pi\vec{\boldsymbol{k}}(t) \cdot \vec{\boldsymbol{x}}) d\vec{\boldsymbol{x}} \qquad (2\text{-}8)$$

As Equation (2-8) shows, the acquired signal $s(t)$ is the Fourier transform of target volume of interest $\boldsymbol{m}(\vec{\boldsymbol{x}})$. Data acquisition can be interpreted as sampling in the spatial-frequency space with trajectory determined by $\vec{\boldsymbol{k}}(t)$. In the field of MRI, this spatial-frequency domain is also referred as k-space domain. Using Equations (2-5), (2-6), and (2-7), the k-space of the excited spins can be arbitrarily sampled by applying properly calculated gradient fields.

2.3 Cartesian and Non-Cartesian Sampling

The most common way to sample the k-space is sampling along rectilinear lines falling onto a Cartesian grid, as shown in Figure 2-1a. With all lines in the raster and all samples in each line are equally spaced, underlying image can be easily reconstructed using inverse Fast Fourier Transform (FFT), a very efficient implementation of the computational intensive Fourier Transform. In addition, Cartesian sampling is very robust to many sources of system imperfections such as off-resonance, eddy currents (12,13). This is because many of these systemic errors are simply encoded as an additional linear phase across k-space.

There are many other trajectories that employs the non-equispaced sampling scheme. One of the popular choices is the radial trajectory, or projection acquisition, as shown in Figure 2-1b. Comparing with Cartesian trajectory, radial trajectory usually requires more samples to achieve Nyquist criteria ($\frac{\pi}{2} * N_{base}$ for radial trajectory, N_{base} for Cartesian trajectory, N_{base} is the base resolution). This is simply because in radial trajectory, the central k-space region is more frequently visited than the outer k-space region. Such non-uniformity causes a reduced efficiency from the sampling theory point of view. However, the frequent visit of k-space center also serve as an averaging effect for the trajectory, makes it less sensitive to motion artifacts. This motion insensitivity is further reinforced by another fact: radial trajectory does not have phase encoding (14). In addition, artifacts from incomplete k-space sampling (i.e. under-sampling) in radial trajectory are mainly streaking in azimuthal direction instead of the replication ghosting that result from under-sampling Cartesian trajectory. If the streaking are not objectionable, this can result in shorter scans without sacrificing spatial resolution compared to Cartesian trajectory (15).

Besides Cartesian and radial trajectories that acquire only one k-space line in each RF excitation, there are many other trajectories that cover the entire or partial k-space with a single or a few RF excitations. Examples are spiral sampling trajectory (Figure 2-1c) and PROPELLER trajectory (16, Figure 2-1d). These trajectories have a higher sampling efficiency due to the larger portion of repetition time being used for data acquisition (ADC on time). Also, they carry the same feature of radial trajectory, such as motion insensitivity and benign under-sampling behavior. As a result, they are widely used in rapid imaging applications to resolve underlying motion. However, these methods are also sensitive to off-resonance spins, which may result in geometric distortion or resolution loss (blurring) in the reconstructed images.

Although most of the non-Cartesian trajectories mentioned above bear nice features for motion and under-sampling, a main drawback of non-Cartesian trajectories, besides their sensitivity to system errors, is the computational cost of image reconstruction when compared with Cartesian trajectory. Since the data are acquired on a non-uniform grid, the computational efficient FFT operation, which requires evenly spaced sampling, is no longer applicable in non-Cartesian trajectories. Although it is feasible to apply an inverse non-uniform discrete Fourier transform (NUDFT) to reconstruct non-Cartesian sampled k-space data, in practice such inversion is extremely time-consuming since it requires the inversion of a large dense matrix. A much faster and computationally economic way is to resample the data onto a uniform rectilinear grid to enable FFT reconstruction. This process is frequently referred to as gridding algorithm or adjoint non-uniform FFT (17, NUFFT). Specifically, gridding algorithm involves convolving of k-space data with a pre-defined finite kernel, sampling onto an oversampled uniform grid, performing an inverse FFT, and

multiplying by a deapodization function. Typically, in order to approximate the inverse NUDFT, the gridding algorithm requires density compensation as an initial step to compensate for the non-uniform sampling density. However, in iterative reconstruction, which will be introduced in the next section, forward and adjoint NUFFT operations can be performed without any density compensation (18) to iteratively approximate the inverse NUDFT.

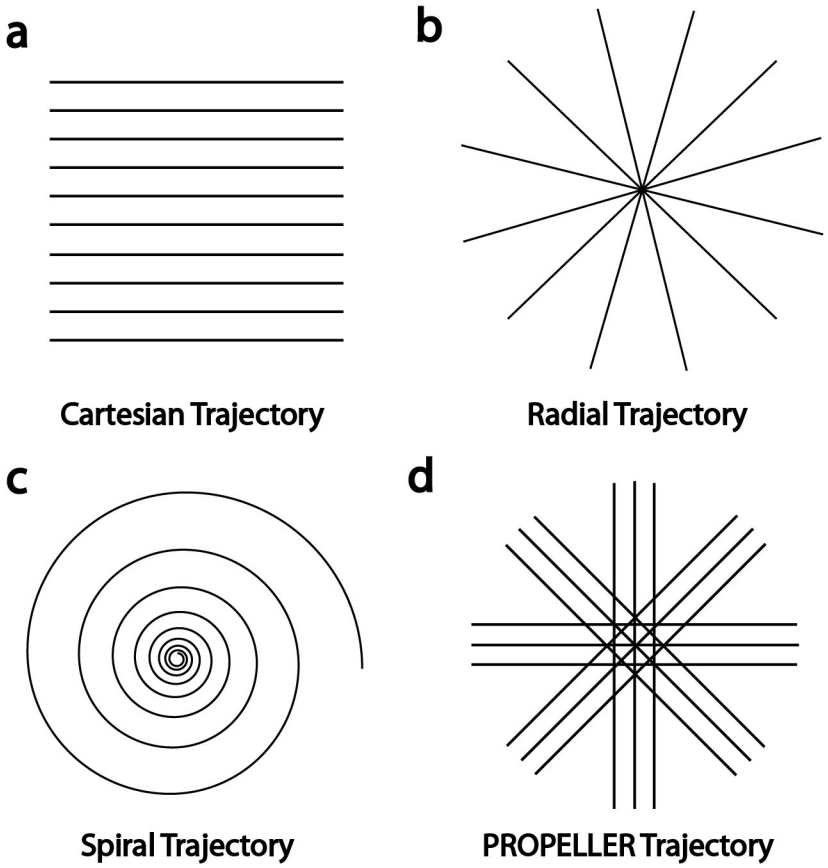

Figure 2-1 Examples of Cartesian and non-Cartesian sampling trajectories.

2.4 Extended Fourier Encoding

For convenience of discussion, Equation (2-8) can be written as a compact linear system in discrete form:

$$\boldsymbol{y} = \boldsymbol{DFm} \tag{2-9}$$

, where $m(\vec{\boldsymbol{x}})$ is discretized as a vector $\boldsymbol{m}$, $\boldsymbol{F}$ is the forward DFT operation, $\boldsymbol{D}$ is the operator that selects and orders acquired data, and $\boldsymbol{y}$ contains $s(t)$ in discrete form.

In most cases, the Fourier analysis in Equation (2-8) or its discretized form Equation (2-9) is sufficient. However, to further push MRI for higher imaging speed, it is necessary to extend this Fourier encoding with additional component. In this section, two widely used acquisition and encoding models and one recently proposed signal processing model are explained to demonstrate the potential of extended Fourier encoding for accelerated acquisition.

2.4.1 Parallel Imaging

Parallel imaging is the technique that utilizes additional spatial encodings provided by multichannel coil arrays to reduce the number of sampling that goes below the Nyquist rate. In essence, the spatially localized coil arrays, which usually have reduced recorded noise and increased SNR when compared with single surface coil, are individually sensitive to a particular region of the imaging object. As a result, the p^{th} coil element "sees" $S_p(\vec{\boldsymbol{x}})\boldsymbol{m}(\vec{\boldsymbol{x}})$ instead of original $\boldsymbol{m}(\vec{\boldsymbol{x}})$ as the object, where $S_p(\vec{\boldsymbol{x}})$ is the sensitivity map that describes the spatial sensitivity of the p^{th} coil element. Consequently, the signal received on the p^{th} coil element, according to Equation (2-8), becomes:

$$s_p(t) = \int S_p(\vec{\boldsymbol{x}})\boldsymbol{m}(\vec{\boldsymbol{x}}) exp\,(-i2\pi\vec{\boldsymbol{k}}(t)\cdot\vec{\boldsymbol{x}})d\vec{\boldsymbol{x}} \tag{2-10}$$

An example of received signal (image) on each coil element $S_p(\vec{\boldsymbol{x}})\boldsymbol{m}(\vec{\boldsymbol{x}})$, coil sensitivity maps $S_p(\vec{\boldsymbol{x}})$, as well as the original imaging object $\boldsymbol{m}(\vec{\boldsymbol{x}})$ is shown in Figure 2-2.

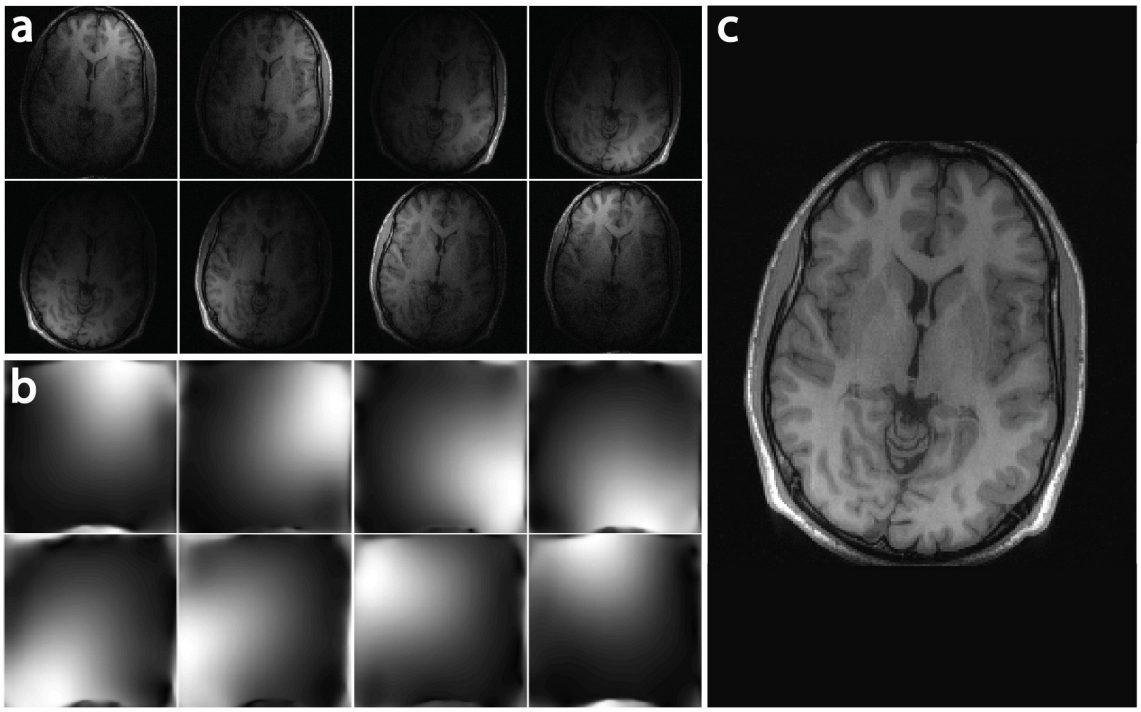

Figure 2-2 a). Multi-channel images from an eight-channel head coil; b). Coil sensitivity maps; c). Original image of interest.

In accelerated acquisition, the goal is to reconstruct an image with M pixels using N samples, where N is always smaller than M, and such problem is usually ill-posed. Parallel imaging exploits the redundant information of localized multiple phased array coils as additional encoding in the image domain to solve the ill-posed reconstruction problem. Under-sampling k-space will lead to image aliasing/ghosting artifact normally. However, in a multi-coil MRI experiment setup, each coil element measures the same imaging object $\boldsymbol{m}(\vec{\boldsymbol{x}})$ with a different coil sensitivity maps $S_p(\vec{\boldsymbol{x}})$. These "repeated measurements" provides means to recover the aliased image. Mathematically, Equation (2-9) can be extended to incorporate the multi-coil measurements as follows:

$$\begin{bmatrix} \boldsymbol{y_1} \\ \dots \\ \boldsymbol{y_C} \end{bmatrix} = \begin{bmatrix} \boldsymbol{DFS_1} \\ \dots \\ \boldsymbol{DFS_C} \end{bmatrix} \boldsymbol{m} \qquad (2\text{-}11)$$

, where $\boldsymbol{y_1}, \ldots \boldsymbol{y_C}$ are measured k-space data from each of the total C coil arrays. Because of the data redundancy, Equation (2-11) is over-determined, allowing the recovery of $\boldsymbol{m}$ when k-space is under-sampled. It can be compacted as follows:

$$\boldsymbol{Y} = \boldsymbol{Am} \qquad (2\text{-}12)$$

, where $\boldsymbol{Y}$ contains all the measured data, and $\boldsymbol{A}$ includes the whole multi-coil encoding process. Image $\boldsymbol{m}$ can be determined by solving the following optimization problem:

$$argmin\ ||\boldsymbol{Y} - \boldsymbol{Am}||_2^2 \qquad (2\text{-}12)$$

Many algorithms have be proposed, and can generally be categorized as either k-space methods such as SMASH (1) and GRAPPA (4), in which missing k-space samples are restored through the estimation of sensitivity maps implicitly, or image space methods such as SENSE (3), in which under-sampling artifacts is removed in image space using known sensitivity maps explicitly. Both methods are compatible with Cartesian or non-Cartesian trajectory, although image-based methods are easier to implement and more general.

In parallel imaging methods, the degree of acceptable acceleration factor depends on multiple factors. The most obvious factor, from mathematics point of view, is the number of independent (orthogonal) components in matrix $\boldsymbol{A}$ (i.e. how different the sensitivity map of each coil element compared to other coil elements). Besides this, SNR is always a factor worth considering. Parallel imaging always sacrifice SNR for the trade of acceleration. The SNR of reconstructed image using parallel imaging is linked to the SNR of fully sampled image as follows:

$$SNR_{Parallel\ Imaging} = \frac{SNR_{Fully\ Sampled}}{g*\sqrt{R}} \quad (2\text{-}13)$$

, where R is the acceleration factor and g is a spatially dependent term called geometry factor (g-factor). G-factor is related to the coil geometry, under-sampling pattern, as well as the k-space trajectory design. A higher g-factor results in a higher condition number of Equation (2-12), and will make it more "difficult" to solve the system of equations. This equivalents to noise amplification in reconstructed image. Therefore, the performance of parallel imaging will reach its maximum when the underlying imaging application has relative high SNR. An example of g-factor effect on reconstructed image is shown in Figure 2-3.

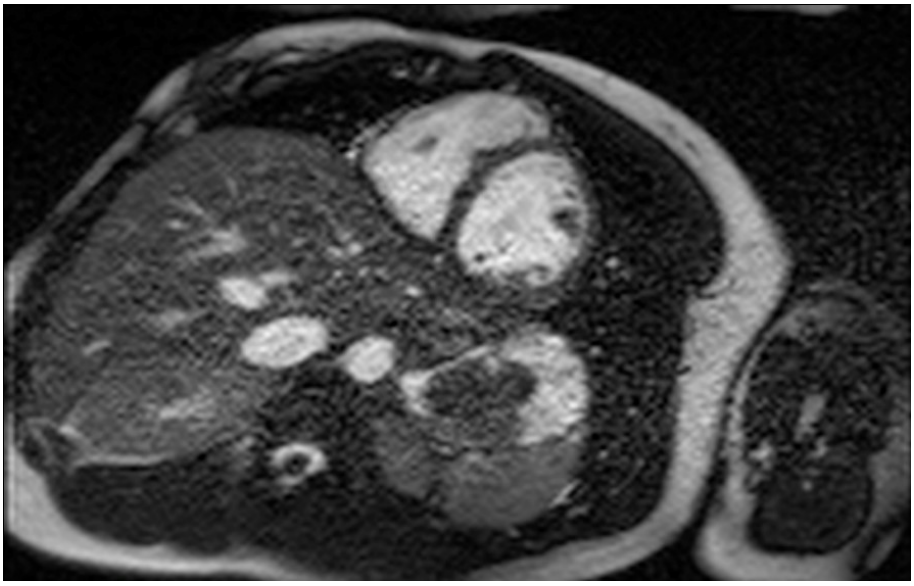

Figure 2-3 Example cardiac image reconstructed with GRAPPA when R=4. Note non-uniform distribution of noise across the image related to a spatially varying g-factor.

2.4.2 Compressed Sensing

Another approach to accelerate data acquisition and recover decent image is by obtaining fewer so-called incoherent k-space samples and reconstruct it through a regularized optimization with iterative methods. Specially, additional image priori-

knowledge (i.e. spatial smoothness, piece-wise linear, sparsity, etc.) can be imposed through regularization terms, together with the so-called data consistency term in Equation (2-12), to balance between the likelihood of existing samples and the accordance with priori-knowledge. This approach is often described using the following equation:

$$argmin\ ||\boldsymbol{Y} - \boldsymbol{Am}||_2^2 + \alpha R(\boldsymbol{m}) \qquad (2\text{-}14)$$

, where $R(\boldsymbol{m})$ is the regularization term that incorporates priori-knowledges on the image, and α is its associated regularization parameter. Common choices of $R(\boldsymbol{m})$ include L1 norm of wavelets transform or total variation. The use of L1 norm to exploit data sparsity in conjunction with random k-space sampling are commonly referred as compressed sensing (5). There are three key components for a successful application of compressed sensing: 1). Compressible sparse coding in transform domain of underlying MR images; 2). Incoherent random k-space sampling; 3). Sparsity enforced reconstruction algorithm. The two main focus for most of research using compressed sensing are the first two components, with the goal of developing better sparsifying transform for more efficient data representation and better sampling pattern for more incoherent measurements. Specifically, researchers have developed and validated different forms of priori-knowledge as regularization terms in Equation (2-14). They started with spatial domain (5,6), and then extended to temporal domain (19–21), and more recently, in motion domain (22,23). In terms of sampling trajectory, early efforts started from pure random sampling, to variable density sampling. An example of different sampling patterns and their under-sampling effect on image is shown in Figure 2-4.

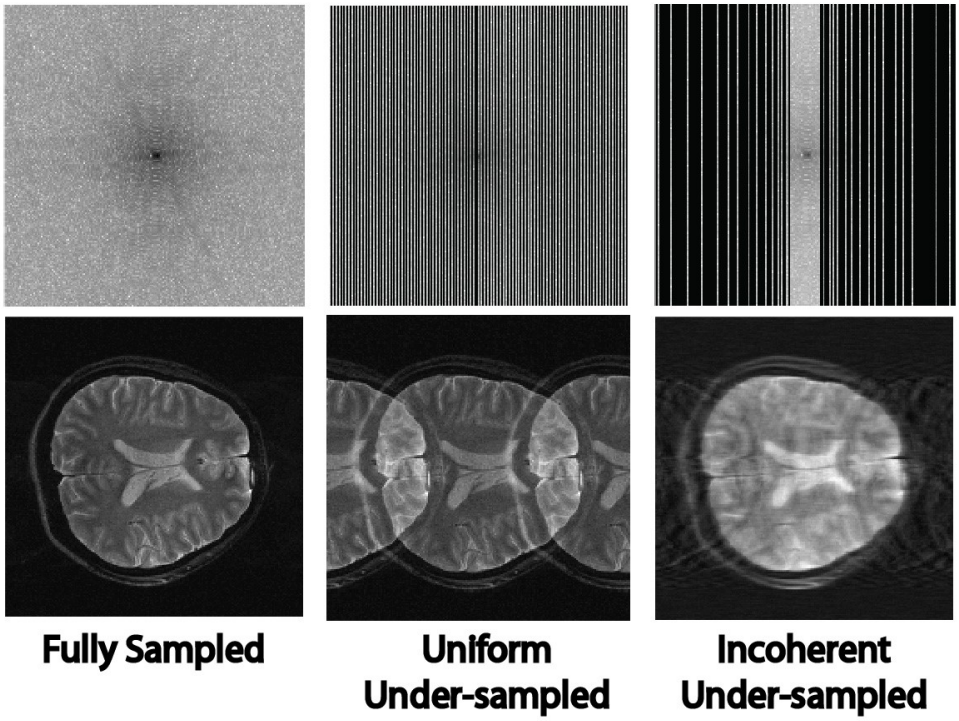

Figure 2-4 Different under-sampling schemes and the resulting image reconstructions.

In compressed sensing type reconstruction, the choice of regularization term is a major concern. The selected regularization represents a particular prior model for the underlying image to be recovered. This also implies that as the optimization converges to the optimal solution (either local or global optimal), the specific feature of the chosen model embodied by the regularization term will be enforced and therefore reflected in the reconstructed image. For example, total variation regularization assumes the underlying image to be piece-wise smooth (24). As a result, if the regularization parameter is not carefully chosen, or the underlying image has convoluted structures, staircase-like over-smoothing artifacts may appear on the final reconstructed image.

Another concern for compressed sensing reconstruction is SNR. During the iterative solution process, one major step is called soft-thresholding, which performs a simple operation of setting the pixels with values smaller than a certain threshold to be zeros, and

the resting pixel to be their values offset by a constant deviation. In essence, this soft-thresholding process will eliminate signal below the threshold, which has the similar effect of denoising. In this case, SNR plays an important role in the performance of such operation. For example, if the signal of target imaging object or underlying physiological phenomenon has level comparable to that of noise, which indicates low SNR, then the soft-thresholding operation will eliminate both true signal of interest and noise at the same time. This renders the poor performance of compressed sensing in low SNR scenario. Therefore, compressed sensing is most useful for applications that have abundant SNR.

It is also noteworthy to point out that, since the reconstruction process in compressed sensing is always non-linear, the description of SNR characteristics of compressed sensing reconstruction is not as straightforward as linear-based reconstruction methods, such as direct inverse Fourier transform or parallel imaging. By adjusting the regularization parameter, which directly links to the threshold value in soft-thresholding operation, the SNR values of compressed sensing reconstructed images can be manipulated to arbitrary number. As a result, care should be taken for the interpretation and evaluation of the SNR measurements from the compressed sensing approach.

2.4.3 Deep Learning

Imitating human learning with deep learning (25,26) has become an enormously important area of research and development, starting from computer vision domain, and gradually being picked up by medical imaging society recently. For most of applications in both fields, such as image classification (27), image restoration (28), q-space image processing (29) and skull striping (30), deep learning was mainly used as a tool for image post-processing and interpretation tool. In the past few years, deep learning, however, is

started to be incorporated in the early image formation stage and serves as an image reconstruction tool for accelerated acquisition.

As discussed in the previous two sections, parallel imaging and compressed sensing are the main techniques to accomplish image reconstruction for accelerated acquisition. However, the acceleration factor achievable with parallel imaging is often limited by g-factor as well as underlying SNR. While compressed sensing outperforms parallel imaging at high acceleration factor, its performance is greatly affected by the choice of regularization term, regularization parameter. An improper choice of either of these will create reconstruction artifacts on the reconstructed image. Specially, pre-defined regularization term may be too simple to capture the complex image content associated with biological tissues, which results in unnatural looking of reconstructed images. At the same time, a poor choice of regularization parameter can either cause over-regularization, which leads to over-smoothing images, or under-regularization, which leads to residual under-sampling artifacts contaminated images. A final challenge for advanced reconstruction methods, no limited to compressed sensing, is their long reconstruction time due to the nonlinear iterative reconstruction process. This greatly impact their clinical adoption even if most of them have superior performance in terms of reconstruction quality.

Deep learning based reconstruction mimics human learning that shifts the online optimization procedure of each individual problem for every new data to an up-front offline training/learning process on a large amount of datasets. Early attempts started with dictionary learning approach (31,32), which learns an online reconstruction as a combination of dictionary elements from the individual under-sampled data itself. The learned dictionary can be treated as a data-driven regularization term, which avoids the use

of pre-defined regularization. However, the dictionary has been learned for every under-sampled data, which still requires online optimization for new problem and results in similar high computational burden and time for conventional compressed sensing algorithm. Later on, several works have been proposed (33–37), based on various network structures, to learn the relationship between zero-filled solution and high-quality images that can be either incorporated as the regularization term in a non-linear reconstruction or used directly for the reconstruction of un-seen under-sampled data. Specifically, a technique called "supervised learning" is employed in these work, where a paired zero-filled solution and corresponding high-quality image is provided to the network. The training process is essence the procedure of finding the optimal parameter sets (i.e. the mathematical description of network) that can minimize the difference between the output of the network, given the zero-filled solution as input, and the high quality image, using a provided error measurement metric. A schematic plot of such procedure is shown in Figure 2-5.

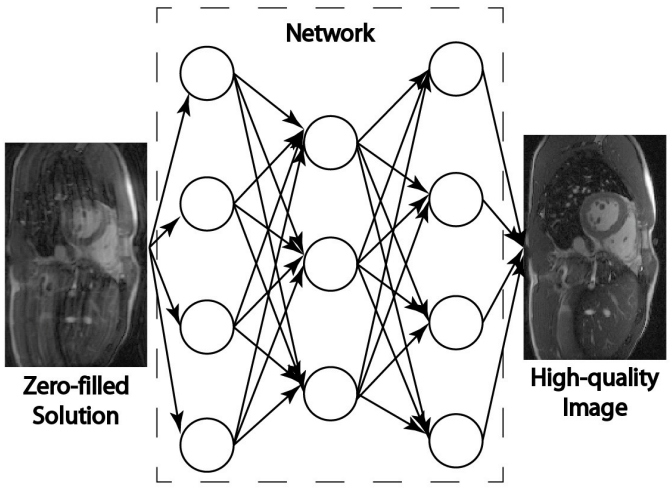

Figure 2-5 Schematic plot of network based reconstruction via deep learning approach.

2.4.4 Conclusion

Limited by the device design and fundamental physics behind MRI, imaging speed still remains an issue for many applications. The reconstruction methods introduced in the previous section were originally designed for general accelerated MR acquisitions. Throughout the development and investigation of each method, they have been shown to be effective for various applications.

However, it should be noted that besides the pros and cons mentioned above for each method alone, they are several common concerns and general challenges, regardless of method chosen, that should be taken into consideration when accelerated acquisition is desirable. These concerns and challenges are more related to the MR application itself instead of the reconstruction method.

One of the major concern is SNR. Like all systems, the measurements made by MRI contain both the NMR signal and the noise originated from the imaging object as well as the electrical components. SNR of acquired image depends on multiple factors, namely physical and instrumental parameters as well as imaging sequence parameters. With a given SNR level for a given MR application, the suitable acceleration techniques should be the ones that can fully exploit the given SNR level to allow effective artifacts removal and noise suppression. In addition, associated imaging trajectory should be designed so that maximal amount of signal can be extracted during ADC turn-on time.

The other often ignored concern is the practical clinical requirement, in terms of reconstruction speed and computation burden, of individual MR application. There are certain MR applications that not only require high quality images, but also benefits from the low latency feedback of image as information for downstream processing or decision

making. It is expected that with careful design of acquisition sequence, trajectory, as well as reconstruction algorithm, desirable spatial and temporal resolution can be achieved. However, at the same time, it is also highly possible that such high quality images requires huge computation resources and long reconstruction time that would not fit into the standard clinical flow. Consequently, developed method loses the practical clinical utility and stays at research stage.

In the following sections, we will examine several well-accepted clinical MR applications that can benefit from accelerated acquisition. Our focus will be application-tailored sequence design with effect k-space traverse, as well as carefully crafted image reconstruction algorithm with high performance in terms of both reconstruction quality and clinical utility.

Chapter 3 Accelerated CS-MUSIC

In this chapter, we look at the first application: ferumoxytol-enhanced 3D multi-phase cardiovascular MRI on pediatric patients with congenital heart disease, and introduce one method to reduce the scan time by approximately 50% while maintaining the image quality and its clinical utility.

3.1 Introduction

Contrast-enhanced magnetic resonance angiography (CE-MRA) is increasingly being used to complement echocardiography or replace digital subtraction angiography for anatomic assessment of cardiac and vascular structures in both adults and children (38,39). CE-MRA is typically performed in a breath-hold during the first-pass of a gadolinium-based contrast agent (GBCA) and provides excellent definition of extra-cardiac vascular anatomy (40). Cardiac gating is typically not performed and requires a substantial compromise in resolution due to the time constraints imposed by breath-holding and the need to capture the first-pass of the GBCA. As a result, conventional first-pass CE-MRA provides insufficient definition of pulsatile structures, such as the ventricular outflow tracts, cardiac chambers and coronary arteries. Therefore, supplemental multi-slice 2D cine imaging is required for assessment of cardiac anatomy and volumes. However, 2D cine employs relatively thick slices (3-4 mm), limiting resolution in potentially tiny hearts and precluding useful multi-planar reformatting.

To address these issues, a recent study proposed a 4D multiphase, steady-state imaging (MUSIC) (41) technique in pediatric patients undergoing cardiovascular MRI under general anesthesia and mechanical ventilation. The 4D MUSIC technique acquires multiple

cardiac-phase-resolved volumetric images without breath-holding during the steady-state intravascular distribution of ferumoxytol, using the ventilator pressure waveform for respiratory gating. Ferumoxytol, an ultrasmall superparamagnetic iron-oxide (USPIO) particle that is approved by the U.S. FDA for parenteral treatment of iron deficiency anemia in adults with chronic kidney disease, was used off-label to enhance the MUSIC acquisition due to its high R1 relaxivity (r_1 = 9.0 $mM^{-1}s^{-1}$ at 3.0T) and long intra-vascular half-life of 10-14 hours (42). Using 4D MUSIC, a 7-10 minute cardiac- and respiratory-gated scan provides images with improved resolution parameters for both intra- and extra-cardiac anatomy than conventional cardiac magnetic resonance (CMR) techniques such as first-pass CE-MRA or 2D multi-slice cardiac cine imaging (41). In this work, we sought to further accelerate the 4D MUSIC acquisition without compromising image quality.

A variety of fast imaging techniques have been developed for accelerating MR data acquisition. Traditional parallel imaging (PI) methods such as sensitivity encoding (SENSE) (3) and generalized auto-calibrating partially parallel acquisitions (GRAPPA) (4) acquire under-sampled k-space by regularly skipping phase encoding lines. These techniques are widely used clinically due to the reasonable image reconstruction time and their robustness at moderate acceleration factors (3-4X). However, as the acceleration factor increases, poor conditioning of the encoding matrix results in progressively more severe artifacts and noise amplification in the reconstructed image. Recent developments in compressed sensing (CS) (43) provide another strategy to accelerate data acquisition (6,44). CS theory states that the image can be recovered from randomly under-sampled k-space data points by using an optimization-based nonlinear reconstruction algorithm with regularization terms incorporated (24,45). With proper choice of regularization terms, the

image may be recovered from a higher acceleration factor than using conventional parallel imaging alone. Although long reconstruction times currently limit the widespread clinical use of CS, progress has recently been reported (46,47) in speeding up certain types of CS image reconstruction algorithms.

In this study, we aimed to take advantage of the high signal-to-noise ratio (SNR) of the ferumoxytol-enhanced 4D MUSIC data by accelerating the MUSIC acquisition with prospective random k-space under-sampling and a joint CS-PI reconstruction technique. The image reconstruction algorithm was implemented in a custom-built parallelized MR image reconstruction system that allowed for clinically acceptable reconstruction time.

3.2 Methods

3.2.1 Data Acquisition

The original spoiled gradient recalled echo (GRE)-based 4D MUSIC sequence (41) was modified in such a way that the center 23×17 k-space region of the ky - kz encoding plane was fully sampled while the outer region was under-sampled using a variable-density Poisson-Disk distribution (48), as shown in Figure 3-1. Each sampled point generated a disk around itself where the probability of a new sample was decreased to ensure maximum spread of the sampling over the ky - kz plane. To simulate the variable density sampling, the disk radius was defined as a function of the distance to the center of k-space (kyc, kzc):

$$Radius_{PDisk}(ky, kz) = 0.3 * \sqrt{(ky - kyc)^2 + (kz - kzc)^2} \qquad (3\text{-}1)$$

To mitigate imaging artifacts and signal interference caused by sudden changes in the sampled k-space location, the ky - kz plane sampling trajectory started from the most central portion of k-space and extended outwards. Samples were sorted and ordered

according to their radii and angles to generate a smooth spiral-like, elliptical centric pattern in the ky - kz plane. This design allowed for sampling of the low frequency data at the beginning of the acquisition, reducing motion sensitivity (49) and eddy-currents effects from high amplitude phase-encoding gradients.

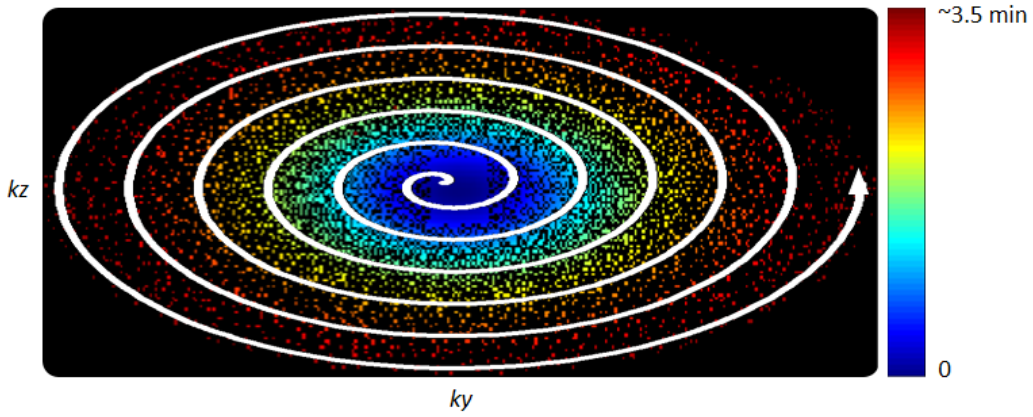

Figure 3-1 Acquisition trajectory in k-space. A variable density Poisson-Disk k-space under-sampling pattern is used to accelerate MUSIC. The fully-sampled center and under-sampled outer k-space result in net acceleration factor of 7X. The trajectory for a single cardiac phase is depicted with samples colored according to their time of sampling from the start time of the acquisition. A center-out spiral arrow is added to reflect sampling order.

3.2.2 Imaging Reconstruction

Prospectively under-sampled data were reconstructed separately for each cardiac phase by ℓ_1-ESPIRiT (50):

$$\hat{d} = \arg\min \sum_{i=1}^{N} ||D\mathcal{F}S_i d - m_i||_2^2 + \lambda||Wd||_1 \qquad (3\text{-}2)$$

where $\mathcal{F}$ is the Fourier transform; S_i are the sensitivity maps estimated from the center region using ESPIRiT (50); D is the operator that selects the locations where data have been acquired; d is the image to be reconstructed; m_i is the acquired under-sampled k-space data from each of the N receiver coil elements; W is the randomized shifting Daubechies wavelets used to approximate translation invariant wavelets that avoids blocky

structural artifacts; and λ is the regularization weight that trades-off between PI data fidelity and the sparsity constraint. In our study, λ was optimized in a pilot study of prospectively under-sampled in vivo data sets acquired on four pediatric congenital heart disease (CHD) patients. We normalized the data sets prior to reconstruction and varied λ from 0.1 to 0.001 in step size of 0.002 to identify the optimal λ value that would provide the best image quality by visual assessment among the reconstructed images. Based on our pilot study, λ was set to 0.004 in our study.

To achieve clinically acceptable reconstruction time, the algorithm was implemented in the C/C++ language based on the Berkeley Advanced Reconstruction Toolbox (51) and integrated within a custom-built MR image reconstruction framework in which external computer nodes are connected to the MR scanner directly. K-space data are sent to the nodes for image calculation and reconstructed images are sent back to the scanner system. Figure 3-2a shows the schematic outline of the framework. Several algorithmic optimizations were incorporated into the reconstruction process to minimize reconstruction time (Figure 3-2b). First, the coil compression coefficient matrix calculation and 3D coil sensitivity map estimation were performed immediately after the fully-sampled k-space center was acquired, while the sequence continued to acquire the peripheral k-space data. Second, to achieve a nearly linear reduction of reconstruction time with the number of threads, the non-linear image reconstruction was parallelized across all of the ky - kz slices using the OpenMP framework (52) with eight threads after an initial fast Fourier transform (FFT) was performed in the readout direction.

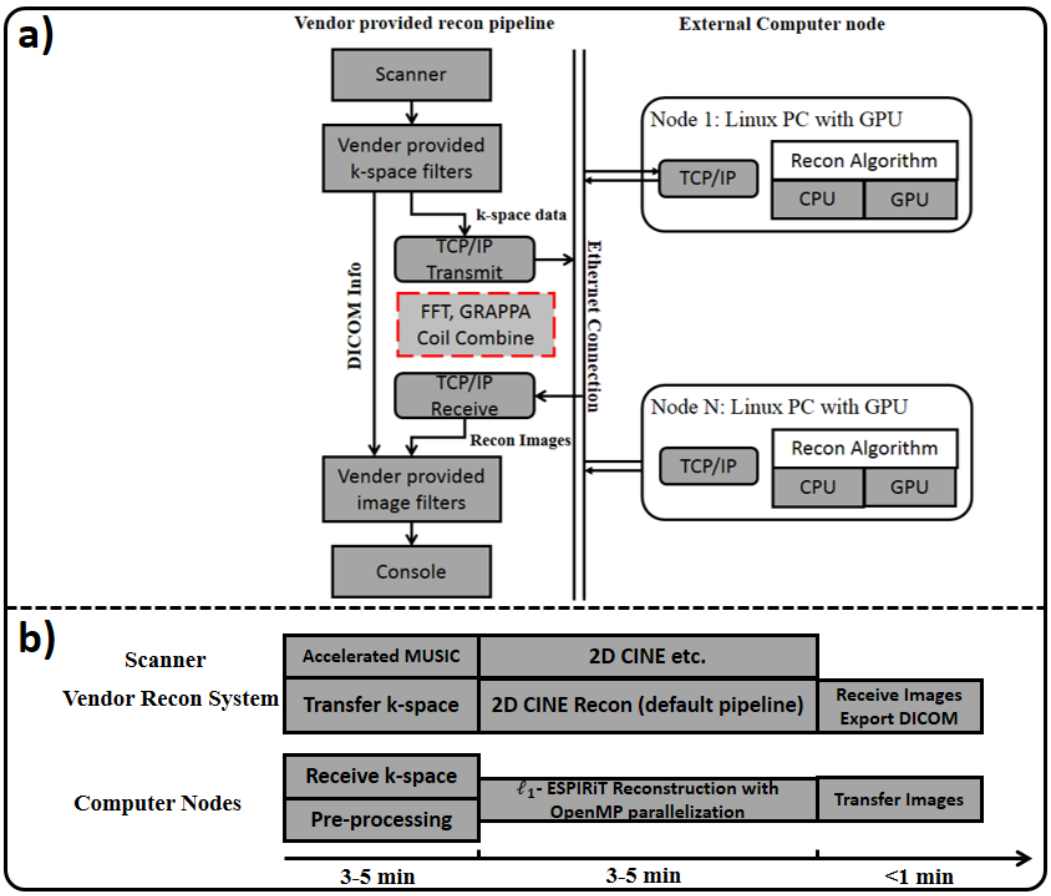

Figure 3-2 a) Custom-built image reconstruction framework where one or more external computer nodes can be connected to the default vendor-provided reconstruction pipeline via TCP/IP. In current implementation, only one external Linux-based computer is connected to pipeline. b) Timeline of the CS-PI 4D MUSIC reconstruction process. K-space data are sent out to the external computer nodes once it is acquired during the scan. Immediately after center k-space region is acquired, pre-processing including coil compression coefficient matrix calculation and coil sensitivity maps estimation starts. Both are calculated in parallel with data receiving on external computer, and are usually done before the finish of data acquisition. It takes 3-5 minutes to reconstruct one 4D dataset (matrix size: 500*300*120*8) and additional 1 minute to send back the images. During the 3-5 minutes when the external computer processes the data, additional scans such as 2D CINE, 2D phase-contrast flow imaging may be acquired in parallel because the ℓ_1-EPSIRiT reconstruction does not use any resources of the vendor provided reconstruction system.

3.2.3 Phantom Study

In order to evaluate the performance of ℓ_1-ESPIRiT (50) within our custom-built reconstruction framework, fully-sampled and regularly under-sampled data were acquired using the original 4D MUSIC sequence (41). Prospective randomly under-sampled data were also acquired using the CS-PI 4D MUSIC sequences on a 1.5 Tesla (T) MRI scanner

(Magnetom TIM Avanto, Siemens Medical Solutions) with a 12-channel body array coil on a standard American College of Radiology (ACR) MRI phantom. Sequence parameters were: repetition time/echo time (TR/TE) = 2.9/0.9 ms; flip angle, 25°; bandwidth = 814 Hz/pixel; matrix size, 256*256*96; resolution, 1mm isotropic. The fully-sampled data was used as a reference. Three regularly under-sampled data were acquired using three different acceleration schemes: one dimensional acceleration 3X for the in-plane phase-encoding direction and two dimensional accelerations of 2×2 and 3×2 in both in-plane and through-plane phase-encoding directions. Actual acceleration factors for these three strategies were 2.6X, 3.7X and 5.4X, respectively, due to the fully-sampled center auto-calibration signal. All three regularly under-sampled data were reconstructed with GRAPPA in the vendor-provided reconstruction pipeline. The prospective randomly under-sampled data were acquired in such a way that the acceleration factor was chosen to match the net acceleration factors of the regularly under-sampled acquisitions with consideration of fully sampled center reference lines.

3.2.4 *In-vivo* Study

Thirteen pediatric CHD patients (aged 4 days to 13 years, six male, heart rate: 95-140 bpm, 118.2 ± 19.5 bpm) who were referred for clinically indicated cardiovascular MRI independent of our research study were included in our study. Clinical indications included preoperative surgical planning or postoperative evaluation. This HIPAA-compliant study was approved by our institutional review board and written informed consent was obtained from each patient's legal guardian(s). As our study requires off-label use of ferumoxytol as an MRI contrast agent, we submitted an Investigation New Drug (IND) application (IND # 129441) to the U.S. Food and Drug Administration (FDA) after the FDA boxed regarding

ferumoxytol administration in March 2015 and subsequently obtained clearance from the FDA to proceed with our study (NCT02752191). Out of the 13 patients, 1 patient, who was more recently enrolled in our study, underwent imaging under our FDA IND. Each patient either underwent general anesthesia in the MRI suite or was transported directly from the neonatal intensive care unit (NICU) already intubated and sedated. Anesthesia was maintained using a mixture of oxygen and sevoflurane while patients from the NICU were sedated with fentanyl. In all cases, patients were injected with rocuronium bromide as a muscle relaxant. An MR compatible ventilator (Fabius MRI, Drager Medical, Telford, PA) was used with positive end expiratory pressure as clinically appropriate.

All 13 patients were scanned on a 3.0 T MRI scanner (Magnetom TIM Trio, Siemens Medical Solution). Depending on the size of patient, a combination of head coil, flexible coil, body array coil or knee coil was used to provide optimal anatomical coverage. Based on previous studies (41,53–55), ferumoxytol (Feraheme, AMAG Pharmaceuticals, Lexington, MA) at a dose of 4 mg elemental iron/kg body weight was used in this study. The agent was diluted by 4X-8X and injected at a rate of 0.1-1.0 mL/s. The rate was adjusted so that the bolus duration was approximately 15s, except for one patient who underwent slow infusion of ferumoxytol over 10 min following the recent FDA recommendations in March 2015. To determine the delay time between initiation of the contrast injection and the arrival of the contrast agent in the region of interest, a small bolus of ferumoxytol (0.5 mg/kg) was injected first and the remaining bolus was injected over 15s followed by a chasing saline bolus injected at the same rate. For the patients who underwent bolus injection of ferumoxytol, breath-held CE-MRA was performed under ventilator-controlled breath-holding (VCBH) during the first-pass of ferumoxytol. The

same VCBH CE-MRA acquisition was repeated during the steady state distribution phase of ferumoxytol, typically 2-3 min after ferumoxytol injection. Parameters for the first-pass and delayed phase CE-MRA included: TR/TE=2.9/0.9ms; flip angle, 15°; in-plane resolution, 0.9-1.2mm; FOV, 500*300*150 mm; slice thickness, 1.1-1.5mm; GRAPPA acceleration 3X-4X; partial Fourier acquisition (75%) for in-plane and through-plane phase encoding directions; total acquisition time: 18-22s. Subsequently, for all 13 patients, the original 4D MUSIC (41) and the proposed CS-PI 4D MUSIC sequences were performed during the steady state distribution of ferumoxytol without VCBH using the air pressure signal from the ventilator circuit for respiratory gating. The data acceptance window was set to the end-expiration phase and the gating threshold was set to 40% of the respiratory signal's dynamic range.

To facilitate qualitative and quantitative comparison with the original 4D MUSIC in this validation study, the CS-PI 4D MUSIC had the same number of cardiac phases as the original 4D MUSIC, but approximately half of the total acquisition time. Scanning parameters were: TR/TE= 2.9/0.9ms; flip angle, 25°; 0.6-0.9 mm true isotropic resolution without interpolation; FOV, 500*300*150 mm; 6-9 cardiac phases depending on heart rate; GRAPPA 2X-3X and 75% partial Fourier in both the phase encoding and partition encoding directions for the original 4D MUSIC, and 7X prospective variable density Poisson-Disk under-sampling for the CS-PI 4D MUSIC. Images from the original 4D MUSIC acquisition were reconstructed immediately with the vendor-provided image reconstruction pipeline, while data from the CS-PI 4D MUSIC acquisition were reconstructed on an external computer in less than 5 minutes using our custom image reconstruction framework shown in Fig 3-2. During the 5 minutes where CS-PI 4D MUSIC

images were being reconstructed offline, conventional multi-slice, multi-planar 2D cardiac cine images (20-25 cardiac phases, temporal resolution: 20-40ms) were acquired per our clinical protocol with VCBH using a spoiled gradient echo sequence.

3.2.5 Quantitative Measurements and Subjective Score

For our phantom study, both normalized root mean square errors (nRMSE) and structural similarity index (SSIM) (56) were calculated between each slice of the reference images and images reconstructed from the under-sampled data. The calculated nRMSE and SSIM were averaged across all slices. Whereas reduction in nRMSE indicates greater fidelity to the original image, perfect identicality is represented by a SSIM value of 1 and the SSIM value decreases as the images differ.

For our in-vivo study, subjective image quality scores of 13 different anatomical region of interests (ROIs) were assessed: left/right atria, left/right ventricles, interatrial septum, interventricular septum, tricuspid valve, mitral valve, left/right ventricular outflow tracts, pulmonary arteries, ascending aorta and coronary arteries. Anonymized and randomized first-pass VCBH CE-MRA images, original 4D MUSIC images, and the CS-PI 4D MUSIC images were graded by two experienced cardiovascular MRI readers with greater than 2 years of experience in clinical cardiovascular MRI interpretation using a 4-point scale as outlined in Table 3-1. Evaluators were blinded to patient information and imaging techniques. Scores were independently provided by the two readers.

Vessel sharpness was quantitatively measured in the left ventricle and ascending aorta of the conventional first-pass CE-MRA, the original 4D MUSIC, and the CS-PI 4D MUSIC images by drawing a linear signal profile, as previously described (41). Specifically, sharpness is defined as the inverse of the distance (in mm) between the two

points at 20% and 80% of the dynamic range. The end-systolic (ESV), end-diastolic (EDV) left ventricular volumes and ejection fractions (EF) based on the contrast-enhanced 2D cine short-axis images, the original 4D MUSIC and the CS-PI 4D MUSIC images were measured using a commercially available software (QMass, Medis, Netherlands). Note that these three sets of images were all acquired at end-expiration.

Table 3-1 Image quality scoring criteria.

Atria and Ventricle	1: Not evaluable due to gross motion artifact and borders not defined 2: Non-uniform blood pool signal and wall motion artifact precludes confident evaluation of luminal contents 3: Uniform blood pool signal with mild wall motion artifact adequate for confident visualization of luminal contents 4: Uniform blood pool signal with no motion artifact such that the ventricular walls, septum, papillary muscles and trabeculae are sharply defined
Interatrial and Interventricular septum	1: Not visualized 2: Presence of septal tissue is seen 3: Probable septal continuity but small defects cannot be confidently excluded 4: Definite septal continuity and small defects can be confidently excluded
Tricuspid valve and Mitral valve	1: Not visualized due to gross motion artifact 2: Annulus visualized but borders poorly defined and cannot be confidently measured 3: Annulus clearly visualized and can be confidently measured but leaflets blurred 4: Annulus sharply defined and can be confidently measured and leaflets clearly visualized
LVOT, AV, and proximal aortic root RVOT, PV, and proximal MPA	1: Not evaluable due to gross motion artifact and borders not defined. 2: Outflow tract and annulus visualized but borders poorly defined and cannot be confidently measured 3: Outflow tract and annulus sharply defined and can be confidently measured but leaflets blurred 4: Outflow tract and annulus sharply defined and can be confidently measured and leaflets clearly visualized
Ascending aorta and Pulmonary artery	1: Not evaluable due to gross motion artifact with non-uniform luminal signal 2: Uniform luminal signal with poor definition of the wall due to motion 3: Uniform luminal signal with mild blurring of the wall due to motion 4: Uniform luminal signal with no motion blurring and sharply defined wall
Coronaries	1: Not evaluable due to gross motion artifact with visualization 2: Only origin of RCA and left main coronary can be identified 3: Origin and proximal course of RCA and LAD can be confidently visualized 4: Origin, proximal, and mid course of the RCA and LAD and proximal takeoff of LCx can be confidently visualized
__AV__ aortic valve; __LAD__ left anterior descending artery; __LCx__ left circumflex artery; __LVOT__ left ventricular outflow tract; __MPA__ main pulmonary artery; __PV__ pulmonic valve; __RCA__ right coronary artery; __RVOT__ right ventricular outflow tract **Scores of 1 or 2 are considered non-diagnostic whereas scores of 3 or 4 are considered diagnostic*	

3.2.6 Statistical Analysis

All statistical analyses were conducted using the R software and Excel (Microsoft, Redmond, WA). The three techniques (CE-MRA, MUSIC and CS-PI MUSIC) were

compared using visual subjective image quality scores (ranging 1-4) in 13 ROIs and quantitative image sharpness in 2 ROIs. The weighted kappa coefficient was used to evaluate the inter-observer agreement for the subjective image quality score. The EDV, ESV and EF measurements were compared using Lin's concordance correlation coefficient and Bland-Altman analysis (57). Subjective quality scores from the average of two readers were compared in two steps per ROI: First, a Kruskal-Wallis test was used to compare among all three techniques; Second, if there was significant difference among the three techniques, post-hoc Dunn's tests would be performed to compare each of the three pairs of techniques (MUSIC vs. CS-PI MUSIC, CE-MRA vs. MUSIC, CE-MRA vs. CS-PI MUSIC). Both tests were performed for each of the 13 ROIs using a Bonferroni correction ($P<0.05/13=0.0038$). Similarly, quantitative image sharpness were compared in two steps after satisfying normality assumption: First, a one-way ANOVA test was used to test the differences among all three techniques; Second, if significant difference was found among the techniques, a post-hoc Tukey's honest significant difference (HSD) test would be performed for each of the three pairs of techniques. Both one-way ANOVA test and Tukey's HSD test were performed separately for the two ROIs (left ventricle and the ascending aorta) using a Bonferroni correction ($P<0.05/2=0.025$).

3.3 Results

3.3.1 Phantom Study

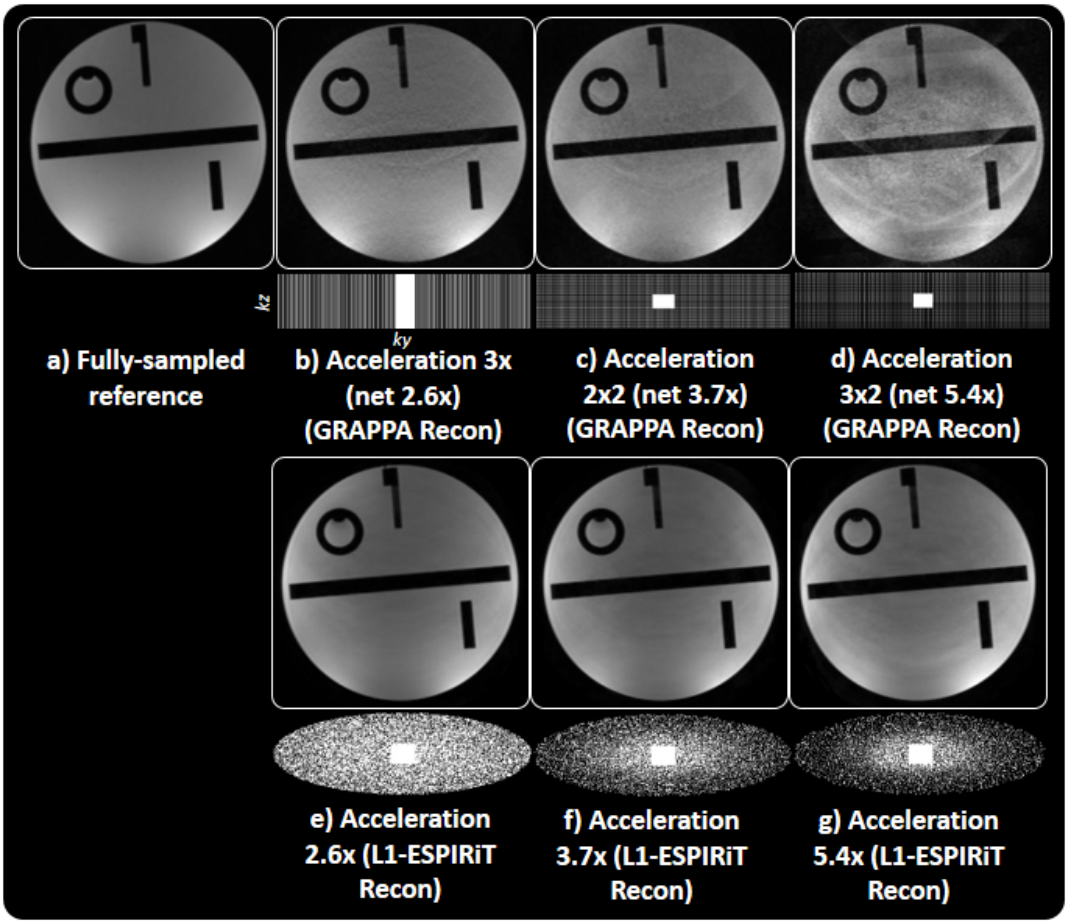

Figure 3-3 Selected slice of reconstructed images from fully-sampled (a), regular under-sampled (b-d) and prospective randomly under-sampled data (e-g) with different acceleration factors. ky - kz under-sampling patterns are shown at the bottom of each selected slice. It can be seen that coherent aliasing artifacts and noise amplification increase as acceleration factor increases with traditional GRAPPA reconstruction, while image quality maintains with the use of ℓ_1-ESPIRiT reconstruction on prospective randomly under-sampled data.

Table 2 shows comparative results of the SSIM and nRMSE between the regularly under-sampled data reconstructed using GRAPPA and the prospective randomly under-sampled data of similar acceleration factors reconstructed using ℓ_1-ESPIRiT (50). The use of PI and CS together reduced the error between the fully-sampled reference and the under-sampled data. Figure 3-3 shows a slice of the reconstructed images using GRAPPA and

ℓ_1-ESPIRiT (50) at different acceleration factors. Substantial aliasing artifact is shown in the GRAPPA reconstructed images; ℓ_1-ESPIRiT (50) offered reduced reconstruction error, even at higher acceleration factors.

Table 3-2 Normalized root-mean square errors (nRMSE) and structural similarity index (SSIM) average values between fully-sampled reference image and images reconstructed from GRAPPA-accelerated/prospectively random under-sampled data. The background noise was excluded from measurement by using only pixels within the upper 90% intensity scale for both calculations.

	nRMSE	SSIM
GRAPPA 3x	0.045	0.877
GRAPPA 2x2	0.069	0.802
GRAPPA 3x2	0.098	0.737
L1-EPSIRiT 2.6x	0.029	0.982
L1-EPSIRiT 3.7x	0.035	0.945
L1-EPSIRiT 5.4x	0.048	0.902

3.3.2 *In-vivo* Study

All image acquisitions were successfully performed, with the scan time ranging from 7 to 10 minutes (8.9±1.2 min) for the original 4D MUSIC, and 4 to 6 minutes (4.6±0.4 min) for the CS-PI 4D MUSIC. Contrast-enhanced 2D multi-slice cardiac cine images were not acquired in 5 patients due to cardiopulmonary instability and concerns about possible blood oxygen desaturation during repeated VCBH.

Figure 3-4 shows a comparison of four images (first-pass, delayed-phase VCBH CE-MRA, the original 4D MUSIC and CS-PI 4D MUSIC) from a 12-month-old male patient. Intra-cardiac structures such as the cardiac chambers, trabeculae, and the aortic root were blurred by cardiac motion due to the lack of cardiac gating in first-pass and delayed-phase

CE-MRA. These structures and other fine structures such as the aortic valve leaflets (dashed black arrow) were well delineated by both the original 4D MUSIC and the CS-PI 4D MUSIC. Note that the acquisition time for CS-PI 4D MUSIC was half of the original 4D MUSIC acquisition. The original 4D MUSIC and the CS-PI 4D MUSIC acquisitions enabled clear delineation of the left anterior descending coronary artery (Figure 3-4, bottom row), which was not possible with conventional first-pass CE-MRA.

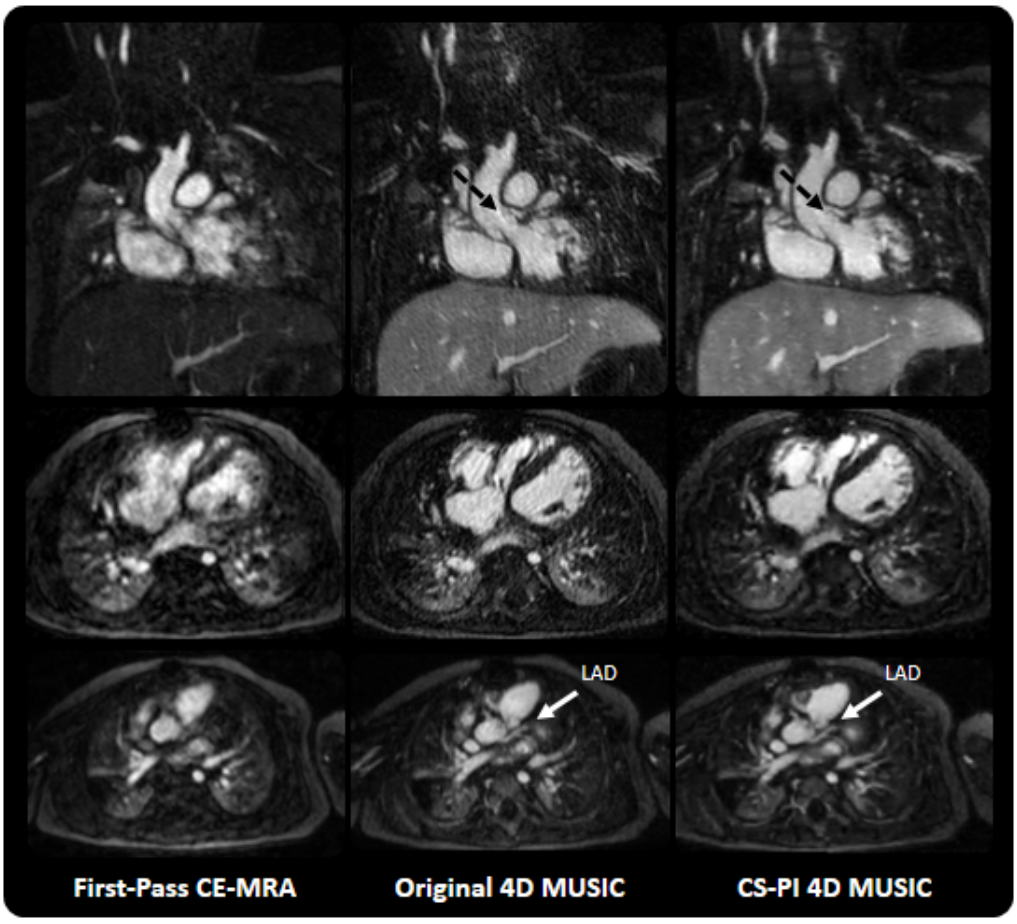

Figure 3-4 First-pass, delayed-phase CE-MRA under VCBH (first and second column) versus original 4D MUSIC (third column) and the proposed CS-PI 4D MUSIC (fourth column) (phase #4 is chosen out of 7 cardiac phases for display) of a 12-month-old, 5.7kg boy. Acquisition times for the original 4D MUSIC and the CS-PI 4D MUSIC were 7 minutes and 3.75 minutes, respectively. CS-PI 4D MUSIC has less structural artifact compared to the original 4D MUSIC, despite its 50% reduced acquisition time. The artifact observed on original 4D MUSIC images is caused by high parallel imaging acceleration (GRAPPA 3X with 75% partial Fourier in ky,kz directions). The cardiac chambers, great vessels, as well as the aortic valve and the coronary arteries (white arrows) can be visualized in the original and CS-PI MUSIC acquisitions, but was poorly defined in the

conventional first-pass and delayed-phase CE-MRA. The delayed-phase image was similar to the first-pass acquisition. The lack of structural artifacts in the CS-MUSIC image enable improved delineation of the aortic valve leaflets (black dashed arrows) compared to the original MUSIC.

The isotropic spatial resolution of both original 4D MUSIC and CS-PI 4D MUSIC allowed reformatting of acquired images into arbitrary 2D cine plane orientations, such as the four-chamber views and short-axis views (Figure 3-5). Comparing with conventional 2D cine images, both original 4D MUSIC and CS-PI 4D MUSIC images provided uniform blood-myocardium contrast, which is important for accurate and robust cardiac chamber segmentation and ventricular volume quantification.

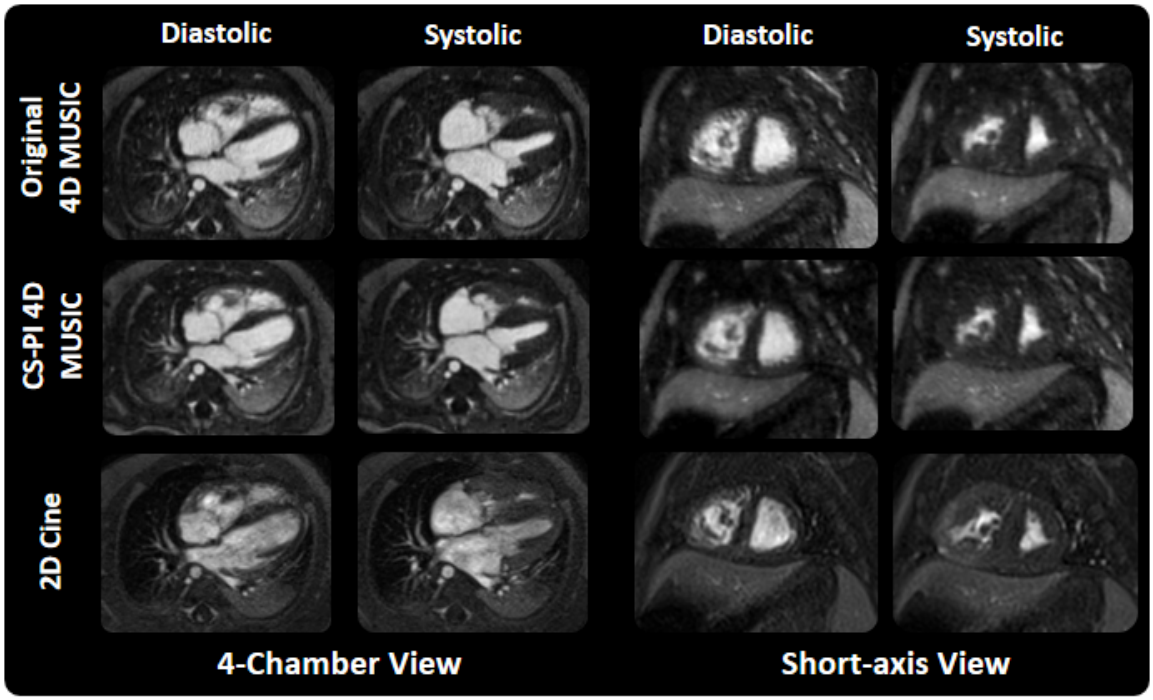

Figure 3-5 Diastolic and systolic phase of reformatted cardiac four-chamber (left two columns) and short-axis (right two columns) views based on original 4D MUSIC (first row) and CS-PI 4D MUSIC (second row) in a 6-month-old, 3kg boy. The cardiac chambers were well delineated for both systole and diastole phases of the cardiac cycle using both the original 4D MUSIC and the CS-PI 4D MUSIC images, despite the shorter acquisition time of CS-MUSIC (4.8 min vs. 9 min). The 0.9 mm isotropic resolution in this patient enabled selection of arbitrary visualization plane without the loss of detailed structure.

3.3.3 Statistical Comparisons of Three Techniques

Two evaluators had moderate to excellent agreement for subjective image quality score, depending on the anatomical site (κ, range 0.46-0.96, Table 3-3). The average image quality scores were used in testing. In right atrium, for example, means (±SE) of the averaged quality image score were 1.8 (±0.2) for the first-pass CE-MRA, 3.9 (±0.2) for 4D MUSIC, and 3.9 (±0.2) for CS-PI MUSIC. The average image quality score provided by the two readers was significantly different among three techniques in all 13 regions of interest (all $P \leq 0.000042$). The subjective image quality scores of both the original 4D MUSIC and the CS-PI 4D MUSIC were significantly higher than first-pass CE-MRA in all 13 regions of interest ($P \leq 0.0014$ for all comparisons). No significant difference was detected between the CS-PI 4D MUSIC and the original 4D MUSIC ($P \geq 0.42$ for all comparisons) despite the much shorter image acquisition time of the CS-PI 4D MUSIC sequence.

Table 3-3 Subjective image quality scores provided by two readers and weighted kappa coefficients κ for different anatomic sites and imaging techniques. (*) denotes statistical significance (P<0.05/13=0.0038) when compared with ferumoxytol-based first-pass CE-MRA.

κ														
	First-pass CE-MRA	**0.88**	**0.88**	**0.88**	**0.88**	**0.88**	**0.88**	**0.88**	**0.88**	**0.88**	**0.88**	**0.88**	**0.88**	**0.88**
	CS-PI MUSIC	**0.87**	**0.85**	**0.8**	**0.85**	**0.84**	**0.82**	**0.81**	**0.81**	**0.53**	**0.51**	**0.86**	**0.85**	**0.52**
	4D MUSIC	**0.87**	**0.84**	**0.85**	**0.86**	**0.96**	**0.85**	**0.78**	**0.78**	**0.48**	**0.49**	**0.85**	**0.86**	**0.46**

Cardiac Structure	Reader 1/Reader 2 (Mean ± SE)			Average Score		
	4D MUSIC	*CS-PI MUSIC*	*First-pass CE-MRA*	*4D MUSIC*	*CS-PI MUSIC*	*First-pass CE-MRA*
Right Atrium	**3.8±0.4/**	**3.8±0.4/4.**	**1.9±0.3/1.8**	**3.9±**	**3.9±0.2**	**1.8±0.2**
Left Atrium	**4.0±0/3.**	**4.0±0/3.8**	**2.2±0.4/2.4**	**3.9±**	**3.9±0.2**	**2.3±0.5**
Right Ventricle	**4.0±0/3.**	**4.0±0/3.6**	**2.0±0/2±0.**	**3.8±**	**3.8±0.3**	**2±0.2**
Left Ventricle	**3.9±0.3/**	**3.9±0.2/3.**	**2.0±0/2.3±**	**3.8±**	**3.8±0.2**	**2.1±0.2**
Interatrial Septum	**3.8±0.5/**	**3.9±0.3/3.**	**2.1±0.9/2.2**	**3.8±**	**3.9±0.2**	**2.1±0.7**
Interventricular	**3.9±0.2/**	**3.8±0.4/4.**	**2.5±0.5/3.0**	**4±0.**	**3.9±0.2**	**2.8±0.5**
Tricuspid Valve	**4.0±0/3.**	**4.0±0/3.7**	**1.4±0.5/2.0**	**3.8±**	**3.8±0.3**	**1.7±0.3**
Mitral Valve	**4.0±0/3.**	**4.0±0/3.7**	**1.4±0.5/2.0**	**3.8±**	**3.8±0.3**	**1.7±0.3**
LVOT	**3.9±0.2/**	**3.9±0.3/3.**	**3.0±0.2/2.3**	**3.7±**	**3.7±0.2**	**2.5±0.2**
RVOT	**3.9±0.1/**	**3.9±0.5/3.**	**3.1±0.4/2.5**	**3.7±**	**3.7±0.2**	**2.5±0.4**
Pulmonary Artery	**3.8±0.4/**	**4.0±0/3.9**	**3.3±0.3/3.5**	**3.8±**	**4±0.1(*)**	**3.2±0.3**
Ascending Aorta	**3.9±0.3/**	**4.0±0/3.9**	**3.1±0.3/3.7**	**3.9±**	**4±0.1(*)**	**3.3±0.3**
Coronary	**3.6±0.9/**	**3.6±0.9/3.**	**1.1±0.3/1.2**	**3.2±**	**3.3±0.9**	**1.1±0.2**

In the quantitative image sharpness, means (±SE) of first-pass CE-MRA, original 4D MUSIC and CS-PI 4D MUSIC were 0.36 (±0.08), 0.56 (±0.17), and 0.54 (±0.17) in ascending aorta and 0.22 (±0.07), 0.38 (±0.11), and 0.35 (±0.11) in the left ventricle, respectively. Image sharpness was significantly different among three techniques in both ascending aorta and left ventricle (P= 0.021 and P=0.003, respectively). Furthermore, both

original 4D MUSIC and CS-PI 4D MUSIC showed significantly improved image sharpness than conventional first-pass CE-MRA at the ascending aorta and the LV chamber ($P \leq 0.023$ for all comparisons, Table 3-4). No significant difference was found between the original 4D MUSIC and the CS-PI 4D MUSIC at both the ascending aorta as well as the LV chamber ($P \geq 0.68$ for all comparisons).

Table 3-4 Vessel sharpness (mm^{-1}) measured in the ascending aorta and left ventricle of the conventional first-pass CE-MRA, the original 4D MUSIC, and the CS-PI 4D MUSIC. (*) denotes statistical significance when compared with ferumoxytol-based first-pass CE-MRA.

	Ascending Aortic (Mean ± SE)	**Left Ventricle Chamber (Mean ± SE)**
First-pass CE-MRA	0.36±0.08	0.22±0.07
Original 4D MUSIC	$0.56\pm0.17^{(*)}$	$0.38\pm0.11^{(*)}$
CS-PI 4D MUSIC	$0.54\pm0.17^{(*)}$	$0.35\pm0.11^{(*)}$

Figure 3-6 shows the LV volume measurements and ejection fractions calculated based on conventional contrast-enhanced 2D cardiac cine, the original 4D MUSIC and CS-PI 4D MUSIC on 8 patients in whom short-axis 2D cine images were acquired. 4D MUSIC and CS-PI 4D MUSIC-derived volume measurements and ejection fractions correlated well with 2D cine MRI-derived measurements (all $r>0.90$ ad $r>0.85$, respectively).

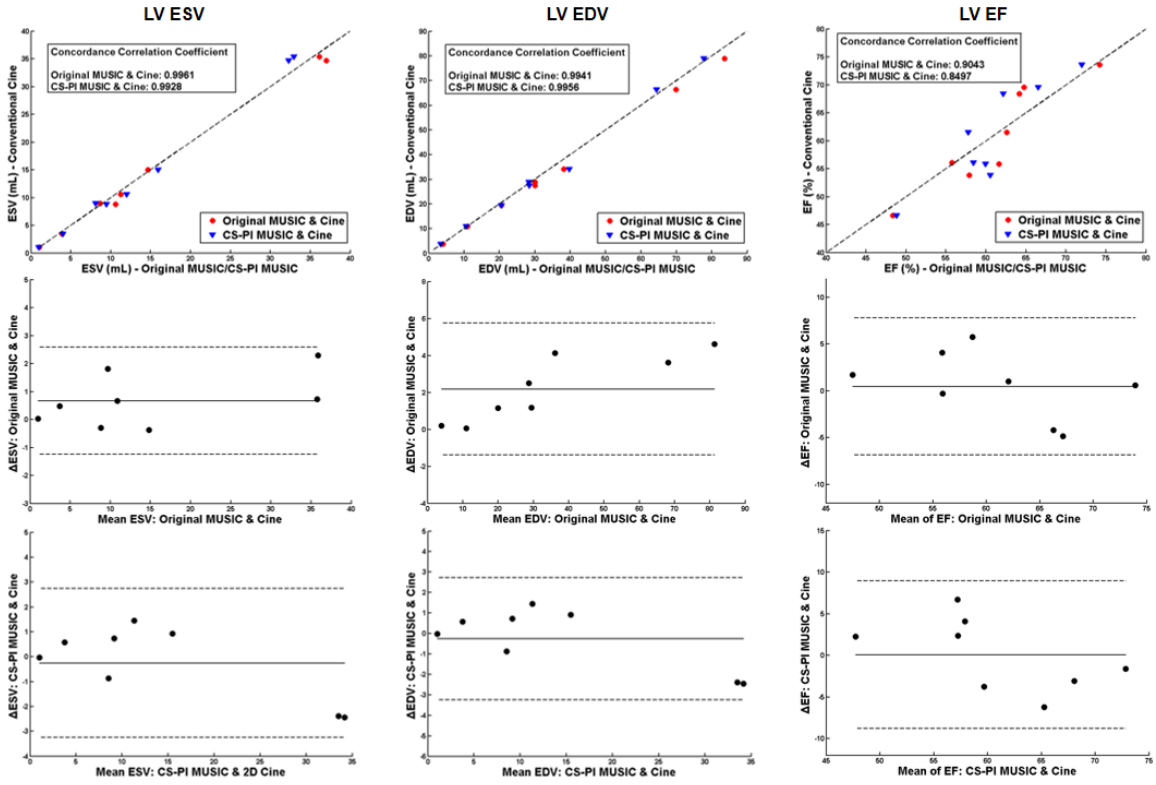

Figure 3-6 Comparison of the left ventricle (LV) a): end-systolic volume (ESV), b): end-diastolic volume (EDV) and c): ejection fraction (EF) derived from conventional 2D cardiac cine, original 4D MUSIC and CS-PI 4D MUSIC on eight patients. Good correlation and agreement were found, as shown in the regression plot (top) and Bland-Altman analysis (middle and bottom).

3.4 Discussion

In this study, we demonstrated the feasibility of halving the acquisition time for high spatial resolution 4D (3D cine) ferumoxytol-enhanced MRI, without compromising image quality. Using a prospective random k-space under-sampling scheme, our CS-PI combined reconstruction method allowed for the acquisition of complete 4D datasets in less than 5 minutes, with a similar image reconstruction time. This technique offers the potential to replace the original 4D MUSIC and may be used to provide temporal resolution that is closer to standard 2D cine MRI.

With CS-PI 4D MUSIC, we were able to achieve similar, or sometimes better, image quality compared with the original 4D MUSIC due to several reasons. First, image artifacts

caused by random under-sampling were incoherent rather than structured. This enabled higher acceleration factors without the structural artifacts that were sometimes observed in the original 4D MUSIC at higher acceleration factors. With a properly chosen regularization parameter λ that reflects the type of data acquired (MRA in our case) and number of iterations, the incoherent artifact induced by random under-sampling is gradually reduced as the iterative reconstruction proceeds. Second, due to the 50% reduction of acquisition time, drifts in the respiratory waveform as the effects of muscle relaxant wear off are less likely to occur. Third, the higher SNR provided by ferumoxytol allowed for more accurate coil sensitivity estimation (50) and effective noise removal with soft-thresholding (5), both of which support high acceleration factors while maintaining image quality.

Our custom-built, on-line image reconstruction system also improves the practicality of the proposed CS-PI 4D MUSIC technique in a clinical environment. The in-house system provided a platform for performing computationally intensive PI and CS combined image reconstruction algorithms outside vendor provided pipelines. At the same time, the default pipeline that includes vendor provided filters enabled reconstructed images to be sent back to the console with DICOM header information intact. Vendor provided k-space filters and image space correction ensured an accurate and unbiased comparison between original and CS-PI 4D MUSIC images, since some of the image correction algorithms, if not performed properly, may result in noticeable distortion of anatomy. Compared with (58), our iterative reconstruction was performed on an external computer instead of on the scanner. With our setup, reconstructions of subsequent clinical acquisitions are not delayed,

and images reconstructed from iterative methods are provided inline and in a clinically acceptable timeframe (<5 minutes).

Balanced steady-state free precession (bSSFP) is the standard technique for 2D cardiac imaging at 1.5T due to excellent blood-myocardium contrast (59). Several attempts have been made to extend its utilization for 3D (60) or 4D (33) cardiac imaging. However, relative low SNR due to diminished in-flow enhancement in non-contrast bSSFP 3D/4D acquisitions limits achievable spatial resolution (e.g nominal resolution: 1.5x1.5x3.5 mm^3 in (32)) or prolongs acquisition time (e.g nominal acquisition time: 14 minutes in (33)). In contrast, the proposed CS-PI 4D MUSIC technique can generate 0.6-0.9mm isotropic, non-interpolated resolution in a 4-5 minute acquisition by taking advantage of the higher available signal at 3.0T and strong R1 relaxivity of ferumoxytol.

In our CS-PI MUSIC data set, only 6-9 cardiac phases are reconstructed. For a typical heart rate of 120 bpm in our patient cohort, this corresponds to a temporal resolution of 50-80ms. Although such a temporal resolution might not be sufficient for accurate assessment for myocardial wall motion abnormalities, it appears to be sufficient for cardiac chamber volume measurements. As chamber volume quantification typically has higher priority than assessment of wall motion abnormality for our pediatric CHD patient population, we did not prolong our scan time in this study to achieve more cardiac phases. In this regard, incorporating k-t constraints in our image reconstruction could further accelerate our scanning and enable more cardiac phases without prolonging the scan time.

The high R1 relaxivity and long intra-vascular half-life of ferumoxytol provide strong and stable enhancement of blood pool signal. However, ferumoxytol also has a stronger R2 relaxivity than conventional GBCA. To minimize the potential signal loss due to T2

relaxation, we used strong partial-echo readout (56%) to minimize TE (0.9ms in our protocol). In addition, to maximize the image contrast, which is determined by both T1 and T2 shortening effect, we carefully chose the contrast dose of 4mg/kg and flip angle of 25°, which provided satisfactory images for both CE-MRA and 4D MUSIC in our study. Further contrast dose and flip angle optimization may further improve the SNR of our acquisitions.

Although patients in our study were under anesthesia or sedation at time of imaging due to clinical need, the CS-PI 4D MUSIC can potentially be applied to patients during free-breathing using other forms of respiratory motion compensation strategies other than ventilator gating, such as diaphragmatic navigators or MR self-gating (61,62) techniques. Although the prospective under-sampling technique was evaluated in the context of evaluating cardiovascular anatomy, this technique may also be applicable to additional spatial/temporal resolution limited applications which may benefit from acquisition of multiple complete 3D volumes within an acceptable acquisition time.

Chapter 4 Motion Weighted Reconstruction

The parallel imaging and compressed sensing combined reconstruction introduced in Chapter 3 for 4D-MUSIC can improve the scan efficiency by a 50% reduction in acquisition time. In this chapter, we take another perspective to improve the scan efficiency by increase the temporal resolution of 4D-MUSIC within same acquisition time. This can potentially improve capacity of using 4D-MUSIC for better cardiac functional assessment.

4.1 Introduction

Cardiac MRI (CMR) is widely used for assessing cardiac structure and function over a spectrum of disorders, including pediatric congenital heart disease (CHD) (63–65). Conventionally, a stack of 2D CINE images is acquired in sequential breath-holds to generate parameters related to cardiac function, including left and right ventricular volumes, myocardial mass and ejection fraction. Although considered the clinical standard in adults, breath-held 2D CINE has limitations for pediatric CHD patients. First, slices are relatively thick (3-5 mm), while the requirement for high spatial resolution is demanding in small children due to the diminutive size of the heart. Additionally, repeated breath-holding and prolonged anesthesia are undesirable in many small children with CHD due to the risk of arterial desaturation.

The recently proposed 4D multi-phase steady-state imaging with contrast enhancement (MUSIC) technique (41) and its self-gated extension using rotating Cartesian k-space (ROCK-MUSIC) (66), have addressed several of the limitations that previously challenged cardiac imaging in pediatric CHD. By generating 4D images with isotropic high spatial resolution, without the requirement for breath-holding or slice positioning, MUSIC and

ROCK-MUSIC have opened up new vistas for speedy and definitive diagnosis, even in tiny patients with the most complex CHD anatomy (67).

When performed in combination with ferumoxytol, the signal from the blood pool on 4D MUSIC is bright and uniform, facilitating segmentation of dynamic ventricular volumes for functional analysis. However, current implementations of 4D MUSIC and ROCK-MUSIC generate about 9 cardiac phases, in 8 minutes and 5 minutes, respectively. Whereas this is sufficient for detailed cardiac and vascular anatomy, the temporal resolution for functional analysis is poor compared to 2D CINE, where 20-30 cardiac phases are routine. Therefore, improved temporal resolution is desirable for more detailed cardiac functional evaluation based on 4D MUSIC or ROCK-MUSIC.

The k-space sampling pattern in the ROCK-MUSIC technique allows for retrospective data binning into an arbitrary number of cardiac phases. Given the same amount of data, increasing the number of cardiac phases means fewer k-space samples for each cardiac phase. To address this issue, algorithms that exploit the temporal correlation of the dataset are usually used to reconstruct the highly under-sampled k-space (68–72). Motion regularized methods reconstruct images of all the motion states (i.e. cardiac phases) in a single optimization process and impose a regularization term on the sparsifying transformation along the motion direction (20,73–75). Although motion regularized methods could reconstruct highly under-sampled dynamic k-space data, the fact that all the images of different motion states are reconstructed in a joint optimization process significantly increases the computational burden and computer memory requirement (22,76).

Motion weighted image reconstruction is a recently proposed alternative approach to reconstructing highly-under sampled, motion corrupted k-space data. Instead of introducing additional regularization terms, the motion weighted methods add a weighting $w \in [0,1]$ to the data consistency term of the compressed sensing type reconstruction based on the degree of motion that occurred. Since the degree of motion corruption is described using the full range of $[0,1]$, this scheme is also called motion soft-gating. The concept was first introduced by Johnson et al. (77) where the weightings were based on the degree of off-resonance, and later applied in free-breathing coronary MR angiography (78), abdominal imaging (79), dynamic contrast enhanced MRI (80), and pulmonary MRI (76) to suppress respiratory motion. One advantage of motion weighted method is that the image reconstruction is independent for each motion state, which not only significantly reduces the computation scale of the problem, but also allows for parallelized implementation.

In this study, we use both a motion regularized method and a motion weighted method to improve the temporal resolution of previously acquired ROCK-MUSIC datasets. The high temporal resolution 4D images (18 cardiac phases) reconstructed by the aforementioned two methods were compared with low temporal resolution (9 cardiac phases) images reconstructed without these methods in terms of image quality and sharpness. Left ventricular (LV) function measurements based on the two sets of high temporal resolution 4D images were validated against the measurements based on 2D CINE.

4.2 Theory

4.2.1 Motion regularized reconstruction

Generally, the optimization problem to be solved in motion regularized reconstruction can be described as follows:

$$\hat{d} = argmin_d \sum_{i=1}^{N} ||D\mathcal{F}S_i d - m_i||_2^2 + \lambda_1||R_1 d||_1 + \lambda_2||R_2 d||_1 \quad (4\text{-}1)$$

where $\mathcal{F}$ is the Fourier transform; S_i are the sensitivity maps; D is the operator that selects the locations where data have been acquired; d is the multi-phase images to be reconstructed; m_i is the acquired under-sampled k-space data from each of the N receiver coil elements; R_1 and R_2 are spatial and temporal sparsifying transforms, respectively; and λ_1 and λ_2 are corresponding regularization parameters. One of the popular choices for temporal regularization R_2 in cardiac imaging is total variation (22,81), which assumes that cardiac motion (i.e. contraction and relaxation) is smooth and continuous across the cardiac cycle.

4.2.2 Motion Weighted Reconstruction

In motion weighted reconstruction, data in two temporally adjacent phases ($p-1$ and $p+1$) were included into the reconstruction of the target phase p. Data acquired in the target phase were assigned a weight of 1, and data acquired in adjacent phases were assigned a weight between 0 and 1, according to its temporal separation from the target phase within the cardiac cycle. For data acquired closer (in terms of temporal location) to the target phase, a larger weight is assigned (i.e. 0.9), while for data acquired further away, a smaller weight is assigned (i.e. 0.1). The optimization problem is thus modified as follows:

$$\widehat{d_p} = argmin_{d_p} \sum_{i=1}^{N} \left|\left|W(D\mathcal{F}S_i d_p - M_i)\right|\right|_2^2 + \lambda_1||R_1 d_p||_1 \quad (4\text{-}2)$$

where d_p is the image of target phase; M_i is the multi-coil k-space data of the target phase and two adjacent phases; and W is the diagonal matrix containing the weight for each data point. The solution of this motion weighted reconstruction converges toward the target phase p and the temporal blurring caused by incorporating data from the adjacent cardiac phases are inherently suppressed in the reconstruction process. This is in contrast to the conventional view-sharing reconstruction, where all incorporated data are treated equally and W in Equation 4-2 becomes an identity matrix.

4.3 Methods

4.3.1 Data Preparation

This study included 12 pediatric CHD patients who underwent Ferumoxytol-enhanced CMR exams on a 3.0T whole-body scanner (Magnetom TIM Trio, Siemens Healthcare solutions) during uninterrupted positive pressure ventilation. The study was approved by our institutional review board and written informed consent was obtained before each MRI scan. The CMR protocol included both ROCK-MUSIC (TE/TR = 1.2ms/2.9ms, matrix size: 480x280x140, 0.8-1mm^3 isotropic resolution, total acquisition time = 6min, FA=20^o) and multiple 2D CINE covering the left ventricle in cardiac short axis (TE/TR = 1.8/3.6ms, 12 second ventilator controlled breath-held, 1mm in-plane resolution, 5mm slice thickness, 25 cardiac phases, ECG gated).

4.3.2 Image Reconstruction

The ROCK-MUSIC data first underwent respiratory gating by discarding the data that were acquired outside the gating acceptance window, which was set to 40% of the

respiratory signal's dynamic range (41). Each dataset was then reconstructed using four different strategies.

Strategy 1: Data were binned into 9 cardiac phases and reconstructed phase-by-phase using standard parallel imaging and compressed sensing combined algorithm with spatial wavelets regularization only (8):

$$\hat{d} = \arg\min \sum_{i=1}^{N} ||D\mathcal{F}S_i d - m_i||_2^2 + \lambda_1 ||R_1 d||_1 \qquad (4\text{-}3)$$

Strategy 2: Data were binned into 18 cardiac phases and reconstructed using cardiac motion regularized reconstruction (Equation 4-1), with spatial wavelets regularization and temporal total variation regularization.

Strategy 3: Data were first separated into 18 bins as shown in Figure 4-1a. A flat-topped two-sided Gaussian kernel that slides through each bin was then generated and used to weigh each data point that resides under the kernel. Specifically, the flat-topped Gaussian kernel was scaled with the maximum set to 1 and centered at each bin, with the duration of the flat top equal to the duration of the target bin, and the duration of the ramps on each side equal to half of the duration of the adjacent bins. The parameters (mean and standard deviation) of the Gaussian ramps were designed such that it decays to half strength at 50% of its duration. A schematic plot of this Gaussian kernel is shown in Figure 4-1b. Finally, the acquired data and corresponding weights were grouped into individual cardiac phases (18 in total), as shown in Figure 4-1c, and reconstructed phase-by-phase using the motion weighted reconstruction (Equation 4-2), with spatial wavelets regularization.

Strategy 4: All non-zero values of the weighting matrix W used in Strategy 3 were replaced with 1, making Strategy 4 identical to a conventional sliding window reconstruction that

reconstructs 18 temporal frames based on the 4D datasets, where the temporal footprint of each temporal frame is twice as long as the temporal sampling period of the dynamic image.

All reconstructions were performed on a custom-build Linux PC (4 Core/4GHz, 64 GB Memory, Nvidia GTX 760) with parallelized CPU and GPU acceleration using C++ and the BART toolbox (51). Image reconstruction time for each strategy was recorded.

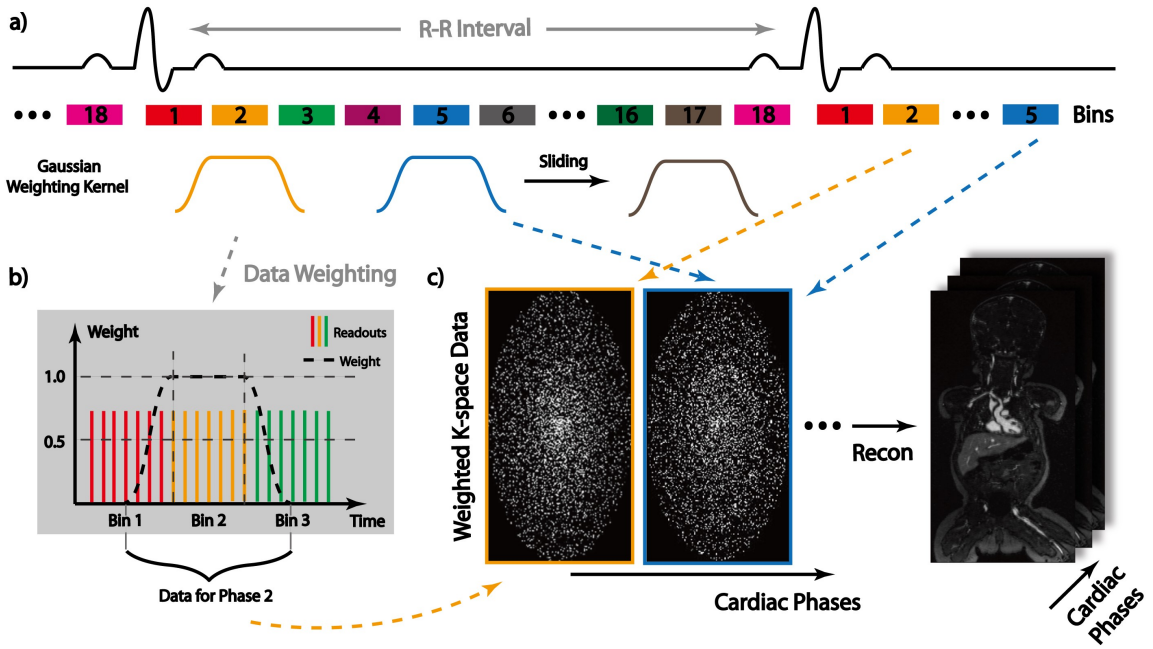

Figure 4-1 Illustration of motion weighted image reconstruction (Strategy 3). (a). Acquired data were first evenly separated into 18 bins. A Gaussian weighting kernel that slides through each bin was then used to weigh readouts that reside under the kernel. (b). Specifically, the weighting kernel has a flat top over the duration of the target bin, and the duration of the ramps on either side equals half of the duration for the adjacent bins. Weight equals to 1 was assigned to readouts under the flat top, while progressively decaying weights were assigned to readouts under the side ramps. (c). Finally, the acquired data and corresponding weights were grouped into 18 cardiac phases and input to a phase-by-phase parallel imaging and compressed sensing combined reconstruction algorithm

4.3.3 Image Analysis

Regional image sharpness measurements were calculated using inverse gradient entropy, a metric highly correlated with observed image sharpness (82). To evaluate the

effect of motion on image sharpness, inverse gradient entropy was computed for two regions of interest (ROIs): the common carotid artery (CCA, static tissue) and the entire heart (non-static tissue). For each region, inverse gradient entropy was computed separately for each cardiac phase, and averaged across all phases. The 3D rectangular ROIs were defined manually and the selected pixel data were processed using an in-house MATLAB program. Higher inverse gradient entropy indicates sharper image.

4.3.4 Statistical Analysis

Quantitative gradient entropy-based image sharpness was compared in two steps after satisfying normality assumption: First, a one-way ANOVA test was used to test the differences among all four reconstructions; Second, if significant difference was found among the techniques, a post-hoc Tukey's honest significant difference (HSD) test was performed for each of the four pairs of strategies. Both one-way ANOVA test and Tukey's HSD test were performed separately for the two ROIs (CCA and the heart) using a Bonferroni correction ($P<0.05/2=0.025$). The EDV, ESV and EF measurements from the four reconstruction strategies were compared with the measurements from CINE images using Lin's concordance correlation coefficient (57).

4.4 Results

All retrospective reconstructions were completed successfully. Reconstruction time was 0.73±0.15 min per phase for Strategy 1, 4.1±0.36 min on average per phase for Strategy 2, 0.72±0.18 min per phase for Strategy 3, and 0.72±0.09 min per phase for Strategy 4.

Figure 4-2 shows representative images of the four reconstruction strategies from a 6-year-old 6.2kg female patient. Fine intra-cardiac structures such as the papillary muscles and their connections (black and red arrow heads) were more clearly defined in Strategies 2 and 3 than with Strategies 1 and 4 due to the lower temporal resolution for 9 phase reconstruction and longer temporal footprint for view-sharing reconstruction, respectively. With lower effective under-sampling (more data are used for each phase) in Strategy 3, the reconstructed images had slightly lower background noise and sharper delineation of fine structures compared with Strategy 2.

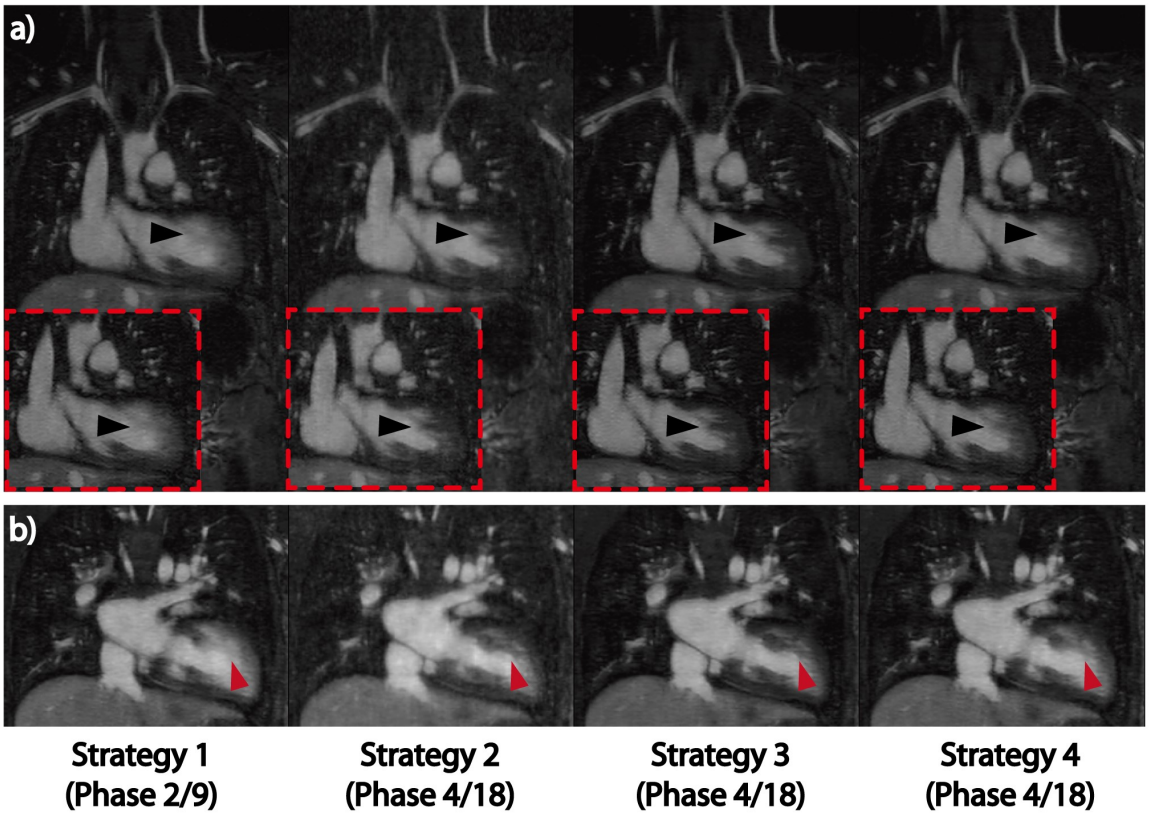

Figure 4-2 Reconstructed 4D images (selected slice and phase) using the four different strategies on the same dataset acquired on a 6-years-old female patient. Low temporal resolution reconstruction in Strategy 1 results in motion blurred intra-cardiac structures such as the papillary muscles and their connections (black and red arrow heads). Using view-sharing in Strategy 4 can improve the temporal resolution, which leads to slightly sharper delineation of these fine structures. However, the temporal footprint in Strategy 4

remained the same as Strategy 1. With a true higher temporal resolution and temporal footprint reconstruction in Strategy 2 and 3, cardiac motion is nicely resolved with well-defined intra-cardiac structures.

The high temporal resolution from reconstructions with Strategies 2 and 3 may be helpful for clearer visualization of major coronary arteries. Figure 4-3 shows the right coronary artery (RCA) and left anterior descending artery (LAD) in a 4-year-old 4.8kg male patient. Due to the long temporal footprint of view-sharing reconstruction in Strategy 4, both the RCA and LAD are blurred by the cardiac motion (red arrows). Conversely, the true short temporal footprint reconstructions from Strategies 2 and 3 enabled clear visualization of these coronary arteries.

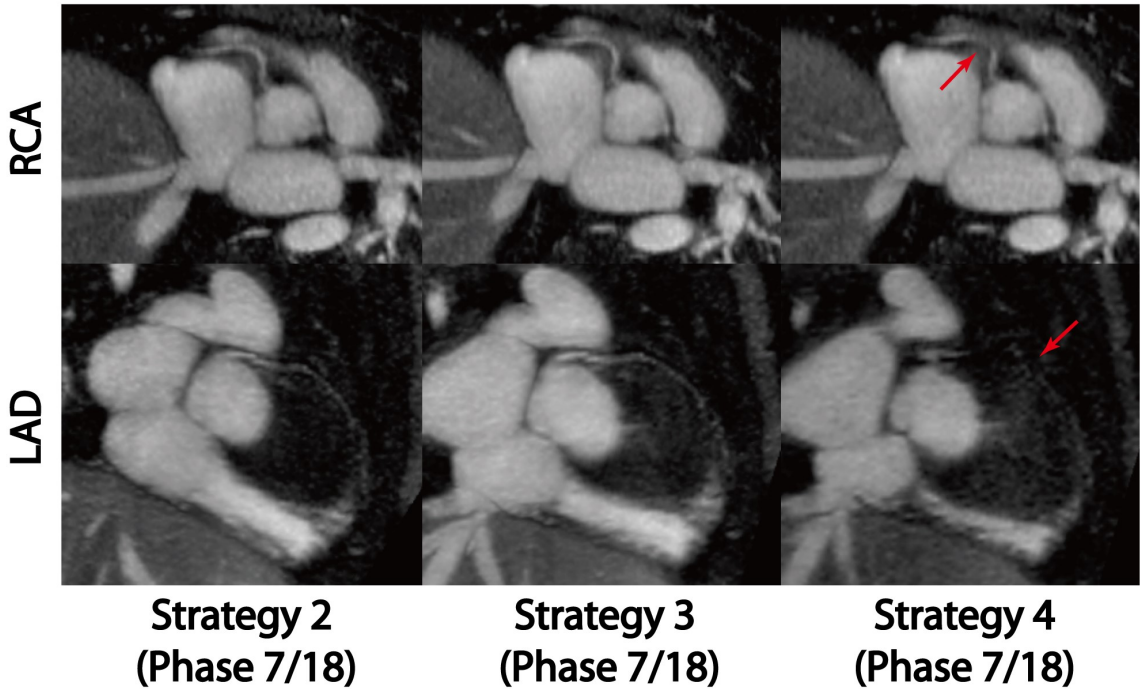

Figure 4-3 Multiplanar reformat images of the coronary arteries from a 4-year-old male patient using three reconstruction techniques with high temporal resolution. The long temporal footprint using view-sharing reconstruction (Strategy 4) precludes visualization of the full length and course of the RCA and LAD (red arrows). On the other hand, strategies with shorter temporal footprints (Strategies 2 and 3) allow sharper visualization and clearer course of these structures.

Figure 4-4a demonstrates the two ROIs that are used to determine image sharpness in an exemplary image. As shown in Figure 4-4b, mean sharpness scores (±standard deviations) of the four reconstruction strategies were 0.693±0.027, 0.538±0.013, 0.543±0.011, and 0.705±0.022 in the CCA, respectively. Image sharpness was significantly different among the four techniques (P= 0.008). Furthermore, Strategy 1 and 4 showed significantly improved image sharpness than the other two strategies for the CCA ($P \leqslant 0.018$ for all comparisons), but not a significant difference among themselves. This is because more data are included in the image reconstruction in Strategies 1 and 4, which translate to higher spatial resolution. However, in the heart region, Strategies 2 and 3 reconstruct significantly sharper images than Strategy 1 and 4 (0.309±0.011, 0.389±0.008, 0.392±0.006 and 0.323±0.012, respectively, P = 0.016 for global comparison, $P \leqslant 0.021$ for all paired comparisons between Strategies 2,3 and Strategies 1,4). This is because the spatial resolution advantage of Strategies 1 and 4 was compromised by the cardiac motion blurring resulting from their lower temporal resolution. Such compromise is more severe in the pediatric application where patients usually have high heart rate (>100bpm).

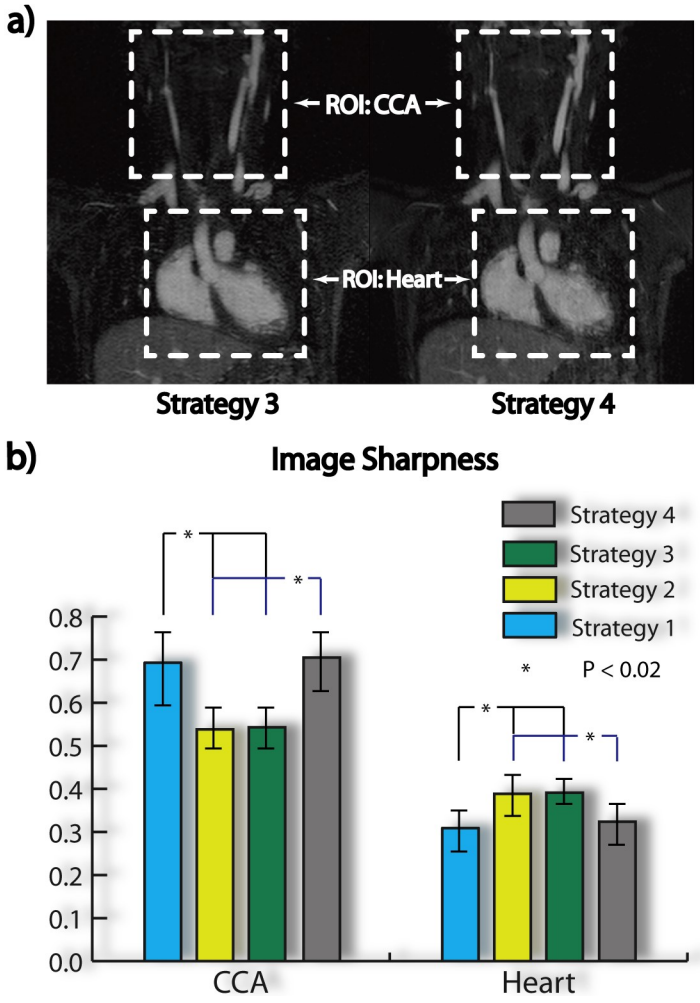

Figure 4-4 (a) Reconstructed images for Strategies 3 and 4 demonstrate the two regions-of-interest (ROIs) where image sharpness was measured using inverse gradient entropy. (b) Regional image sharpness of two ROIs (common carotid artery [CCA] and heart) using images reconstructed from four different strategies. Higher inverse gradient entropy indicates sharper image. In the static CCA, both Strategies 1 and 4 have significantly higher sharpness than Strategies 2 and 3, due to the lower under-sampling factor. However, in the heart, where intra-cardiac structures are dynamic, Strategies 2 and 3 have significantly higher sharpness than Strategies 1 and 4 because of the higher effective temporal resolution and temporal footprint in the setting of complex cardiac motion.

Because the reconstructed 4D images from MUSIC and ROCK-MUSIC can be reformatted into any user-specified slice orientation, the images were reformatted into ventricular short-axis views similar to those prescribed for 2D CINE. Figure 4-5 shows images in multiple selected cardiac phases. The M-Mode plot at the level of the blue dotted

line is shown at the right to enable visual comparison of the temporal resolution of the reconstruction strategies. The limited temporal resolution of Strategy 1 resulted in a coarse temporal profile, while the remaining three strategies provided smoother profiles over time, similar to 2D CINE. The blood-pool signal is much more uniform in all 4D MUSIC images than those of 2D CINE, which is a desirable feature for ventricular segmentation.

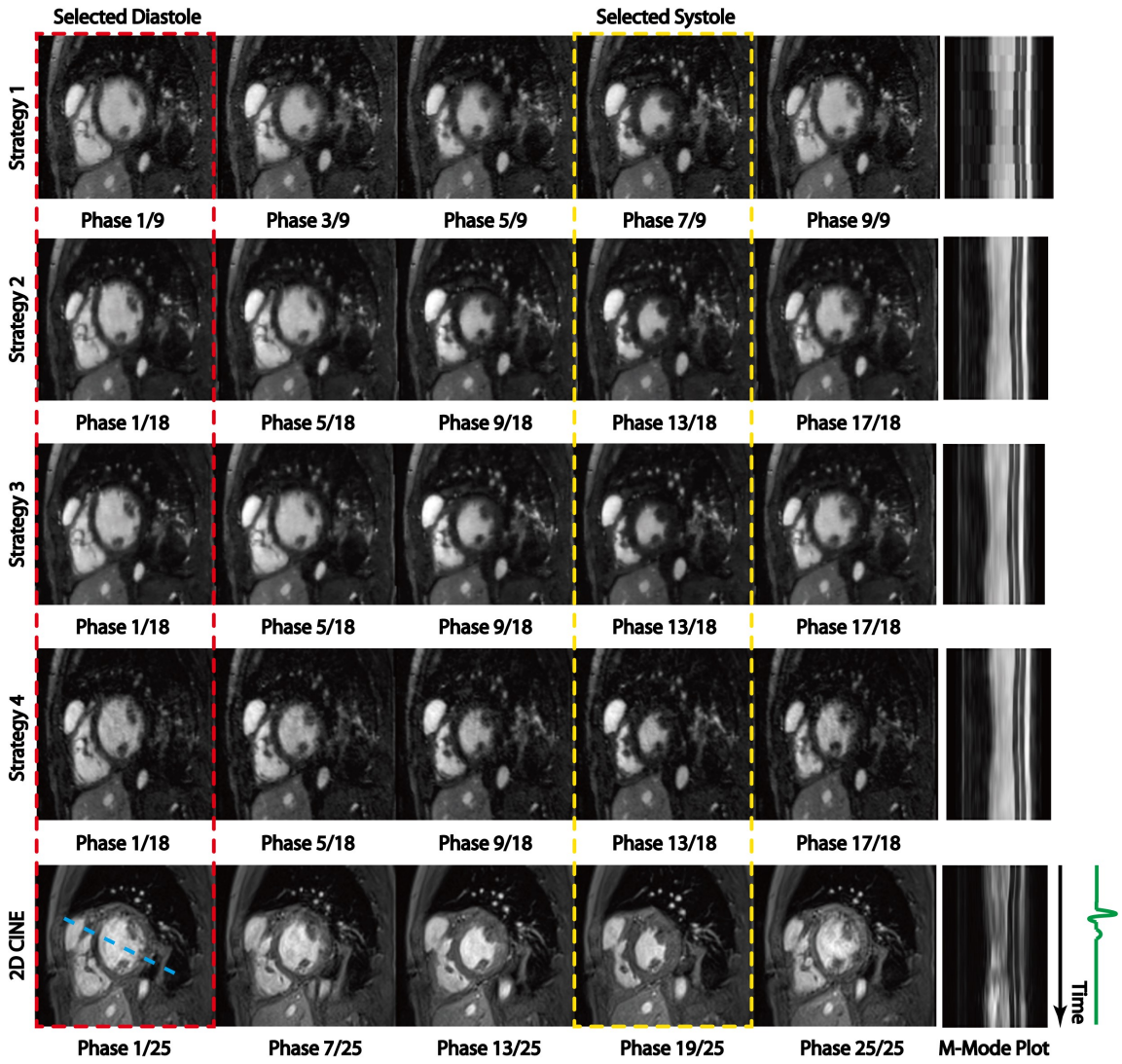

Figure 4-5 Reformatted ventricular short-axis views of the heart from four reconstruction strategies and 2D CINE. The M-mode plot to the right of the figure reflects the temporal resolution at the location of dashed blue line for each of the different strategies. The temporal profile of Strategy 1 is coarse because of limited temporal resolution whereas the temporal profiles of the other three strategies are smoother and similar to 2D CINE. The

selected end-diastole and end-systole phases for volumetric measurements are highlighted with red and yellow dashed boxes, respectively.

Table 4-1 summarizes the quantitative left ventricular functional measurements, including ESV, EDV and EF based on the four different reconstruction strategies with values from 2D CINE as the reference standard. The measurements based on images with low temporal resolution (9 phases, Strategy 1) have a systemic 8% overestimation of ESV and about 2% underestimation of EDV compared with measurements based on 2D CINE. These errors resulted in 7% underestimation of EF. Measurements based on images with high temporal resolution (18 phases, Strategies 2,3 and 4) had much smaller errors (<3.5%) based on 2D CINE values. There were minimal differences between Strategies 2,3 and 4 in terms of quantitative LV functional measurement. All these observations are also reflected in Lin's correlation coefficient shown in Table 4-1.

Table 4-1 Quantitative left ventricular functional measurements. Lin's correlation coefficients for measured volumes/ejection fraction between each strategy and the reference standard 2D CINE images are in parentheses.

	ESV(mL)	**EDV(mL)**	**EF(%)**
Strategy 1	14.81±5.04 (0.72)	34.33±13.16 (0.83)	56.93±8.18 (0.79)
Strategy 2	13.71±4.19 (0.91)	34.46±12.79 (0.96)	58.79±9.35 (0.93)
Strategy 3	13.88±5.31 (0.94)	34.83±13.17 (0.98)	58.96±9.01 (0.96)
Strategy 4	14.02±5.06 (0.86)	34.39±12.88 (0.92)	57.99±8.64 (0.9)
2D CINE	13.34±4.77	35.07±13.22	60.43±9.03
Error: Strategy 1 vs CINE	8.39±3.67%	-1.95±0.62%	-6.84±0.46%

Error: Strategy 2 vs CINE	3.25±2.06%	-0.95±0.33%	-2.56±0.64%
Error: Strategy 3 vs CINE	3.46±1.13%	-0.79±0.35%	-2.74±0.68%
Error: Strategy 4 vs CINE	4.06±1.92%	-1.23±0.48%	-3.51±0.52%

4.5 Discussion

In this study, we evaluated four different image reconstruction strategies, all aiming to improve the number of reconstructed cardiac phases of the 4D ROCK-MUSIC dataset for improved cardiac function assessment. In quantitative regional image sharpness, we found obvious improvements using the high temporal resolution reconstruction with Strategies 2 and 3 compared to the original reconstruction or the view-sharing reconstruction. However, there were no significant differences between Strategies 2 and 3 other than the reconstruction time and memory usage. The proposed Strategy 3 requires a shorter reconstruction time than Strategy 2. In our implementation, the 4D images with 18 cardiac phases can be reconstructed within 10 minutes and 23 GB memory using the motion weighted reconstruction method, while over 2 hours and 60 GB memory is required when using the motion regularized reconstruction method, with the same computer hardware. Based on these findings, the motion weighted reconstruction method represents a time- and computational-efficient solution for improving cardiac function assessment based on 4D ROCK-MUSIC. Our solution for image reconstruction based on motion weighing is practical and can be easily implemented in clinical practice.

The motion weighted image reconstruction is different from view-sharing. View-sharing directly includes k-space data from other motion states or temporal frames into the

image reconstruction. The increased temporal footprint of view-sharing will result in motion blurring in the reconstructed images. On the other hand, motion-weighted reconstruction offers an additional "relaxed" subsampling operation where the reconstruction will directly use the k-space data if the weights are closer to 1. The reconstruction will recover data that were not originally sampled or that have weights closer to 0 in the iterative reconstruction.

Since cardiac arrhythmia during image acquisition is not a common concern for pediatric CHD patients, the use of a symmetric flat top two-sided Gaussian kernel in the motion weighted reconstruction is a practical choice for providing high quality images to resolve cardiac motion, with much reduced computation requirements. In cases with irregular heartbeats, cardiac motion blurring may still occur for the motion weighted reconstruction when data under the symmetric Gaussian kernel has experienced a large motion range. This could be addressed by a carefully designed asymmetric kernel that minimizes the motion incorporated in each cardiac phase.

The remaining 2-3% error in LV functional measurement between high temporal resolution reconstructions and the 2D CINE reference standard may be due to the different number of cardiac phases (18 phases for 4D ROCK-MUSIC and 25 phases for 2D CINE) intrinsic for each technique. However, we have to also consider the fact that the 2D CINE is acquired during (ventilator controlled) breath-holding and 4D ROCK-MUSIC is acquired without breath-holding. It is possible that the remaining 2-3% error was due to the physiological effects of breath holding.

4.6 Conclusion

We have presented a practical approach to doubling temporal resolution in 4D cardiac functional assessment in children, based on a ROCK-MUSIC acquisition. Using motion weighted reconstruction, LV quantitative measurements are significantly improved compared to the original reconstruction. At the same time, reconstruction time and computation memory requirements are modest compared with motion regularized reconstructions.

Chapter 5 Accelerated ASL-based Intracranial MRA

In Chapter 3 and 4, we introduced two methods to improve the scan efficiency of an SNR-abundant application: Ferumoxytol-enhanced MRA. The use of conventional parallel imaging and compressed sensing combined reconstruction can effectively reduce the acquisition time by half or double the temporal resolution within same acquisition time. In this chapter, we turned to another application: ASL-based noncontrast-enhanced 4D intracranial MRA, where the SNR level of acquired signal is limited. We will investigate acquisition and reconstruction strategies for accelerated imaging in such a SNR-limited scenario, and examine its feasibility in clinical environment.

5.1 Introduction

The detailed characterization of dynamic flow patterns is important in the diagnosis of cerebrovascular diseases, such as arteriovenous malformation (AVM), arteriovenous fistula (AVF), and intracranial aneurysm (83). Non-contrast enhanced dynamic MR Angiography (NCE-dMRA) (84–88) has become a promising approach due to its completely non-invasive nature and lack of ionizing radiation, compared to digital subtraction angiography (DSA) and dynamic contrast-enhanced MRA (DCE-MRA) (89). The conventional intracranial NCE-dMRA technique combines arterial spin labeling (ASL) with multi-phase k-space segmented balanced steady-state free precession (bSSFP) sequence, and is able to provide dynamic information with high spatial (~1mm^3) and temporal (~100ms) resolution for the evaluation of cerebral malformations (87,90–92) and steno-occlusive diseases (93). However, the segmented cine acquisition usually requires a relatively long scan time to achieve sufficient spatiotemporal resolution and spatial

coverage (90,91), which potentially hampers the application of NCE-dMRA in clinical practice.

Golden angle radial acquisition (94) in conjunction with k-space weighted image contrast (KWIC) reconstruction (95,96) was proposed to accelerate the NCE-dMRA acquisition by up to threefold (97). KWIC is a projection view-sharing technique based on radial k-space sampling (95,96). KWIC applies a spatiotemporal filter by using progressively more radial projection views towards outer k-space so that the image series can be reconstructed at a relative high temporal resolution without introducing severe streaking artifacts. However, a potential drawback of view-sharing techniques such as KWIC is temporal smoothing of rapidly changing events in vessels and at vessel boundaries (98,99).

Recent developments in applying compressed sensing (CS) theory to MRI have revealed new ways of accelerating image acquisition (5). By exploiting the signal sparsity in a transformation domain, CS could reconstruct MRI images from randomly under-sampled k-space by optimizing a non-linear function. It has been successfully applied in cardiac cine imaging (100), phase-contrast flow imaging (101), and dynamic contrast-enhanced body imaging applications (102). However, to date, very few studies have attempted to apply CS in ASL based applications due to the inherently low SNR of ASL signal. Han et al. (103) utilized the complex image subtraction sparsity between control and label images to reconstruct under-sampled perfusion ASL data. Similarly, Zhao et al. (104) enforced sparsity of image under a perfusion model after the complex k-space subtraction of control and label acquisitions and applied it for cerebral ASL perfusion reconstruction. Although complex subtraction sparsity is theoretically sound, it is, in

practice, sensitive to phase errors caused by motion and other sources of off-resonance (105,106), especially in the case of bSSFP readout.

A novel CS algorithm has recently been developed, which takes advantage of the sparsity of the magnitude subtraction (MS) between the pre- and post-contrast images in thoracic DCE-MRA (45). Since the same subtraction sparsity may be applied to ASL-based MRA between the control and label images, we hypothesized that the magnitude-subtraction CS (MS-CS) method could be used to accelerate the acquisition of NCE-dMRA with high spatial and temporal resolutions. In this study, we focused on (1) investigation of the feasibility of using MS-CS to reconstruct highly under-sampled golden-angle stack-of-stars (SOS) NCE-dMRA data set; (2) comparison of the MS-CS method with the conventional independent CS (iCS) and complex-subtraction CS (CS-CS) methods (105,106) for image quality; and (3) comparison of MS-CS with KWIC in terms of temporal fidelity for depicting dynamic blood flow.

5.2 Methods

Similar to a previous work (45), the acquired NCE-dMRA data were reconstructed by optimizing Equation 5-1 for each temporal frame.

$$(m_1, m_2) = argmin \begin{pmatrix} \sum_{i=1}^{N} ||NUFFT(S_i m_1) - y_1^i)||^2 + \lambda||Wm_1||_1 + \mu||m_1| - |m_2||_1 \\ \sum_{i=1}^{N} ||NUFFT(S_i m_2) - y_2^i)||^2 + \lambda||Wm_2||_1 + \mu||m_1| - |m_2||_1 \end{pmatrix} \qquad (5\text{-}1)$$

where y_1^i and y_2^i are single coil (i^{th} coil) k-space data for control and label acquisitions in one frame; m_1 and m_2 are corresponding coil combined images to be recovered jointly, $NUFFT(\cdot)$ is the non-uniform fast Fourier transform (17) that transforms image to radial k-space data; S_i is the sensitivity map of the i^{th} coil; W is the randomized shifting

Daubechies spatial wavelets transform; $||m_1| - |m_2||_1$ is the L1 norm of the pixel-wise magnitude difference between the control and label images; and λ and μ are regularization parameters.

To demonstrate the effectiveness of magnitude subtraction regularization, the conventional iCS and CS-CS reconstructions were also performed using the following equations:

$$\text{iCS: } \begin{cases} m_1 = argmin \sum_{i=1}^{N} ||NUFFT(S_i m_1) - y_1^i)||^2 + \lambda ||Wm_1||_1 \\ m_2 = argmin \sum_{i=1}^{N} ||NUFFT(S_i m_2) - y_2^i)||^2 + \lambda ||Wm_2||_1 \end{cases} \quad (5\text{-}2)$$

$$\text{CS-CS: } I = argmin \sum_{i=1}^{N} ||NUFFT(S_i I) - (y_1^i - y_2^i)||^2 + \lambda ||I||_1 \quad (5\text{-}3)$$

where I is the final complex subtracted image and $||I||_1$ is the L1-norm in the image domain.

5.2.1 MRI Experiments

Six healthy volunteers (aged 28-32 years, 4 male) and one patient (23 y.o., male) with AVF were included in this study, after obtaining Institutional Review Board (IRB) approval and informed consent. All subjects were scanned on a 3T scanner (PRISMA, Siemens Healthcare, Erlangen, Germany) using a 20-channel head coil. NCE-dMRA data were collected using the previously proposed golden-angle SOS NCE-dMRA sequence (97) with the following parameters: spatial resolution=1x1x1.5 mm^3; FOV= 256x256x48 mm^3, TE/TR=2.43/4.86ms, FA=25°, BW=814Hz/pixel, 500 views per shot, one shot per slice, acquisition time: 3min. The sequence diagram for the 3D golden-angle SOS acquisition is illustrated in Figure 5-1. A 6-min 3D Cartesian NCE-dMRA scan without view-sharing (84) was performed as the gold standard for dynamic information. The spatial resolution and imaging coverage were identical to those of the 3D SOS scan. A total of 25 phases

with a temporal resolution of 100ms were collected in the Cartesian acquisition. The sequence diagrams for the 3D Cartesian acquisition is illustrated in Figure 5-2. In addition, time-of-flight (TOF) MRA images were acquired as a reference for the anatomical information.

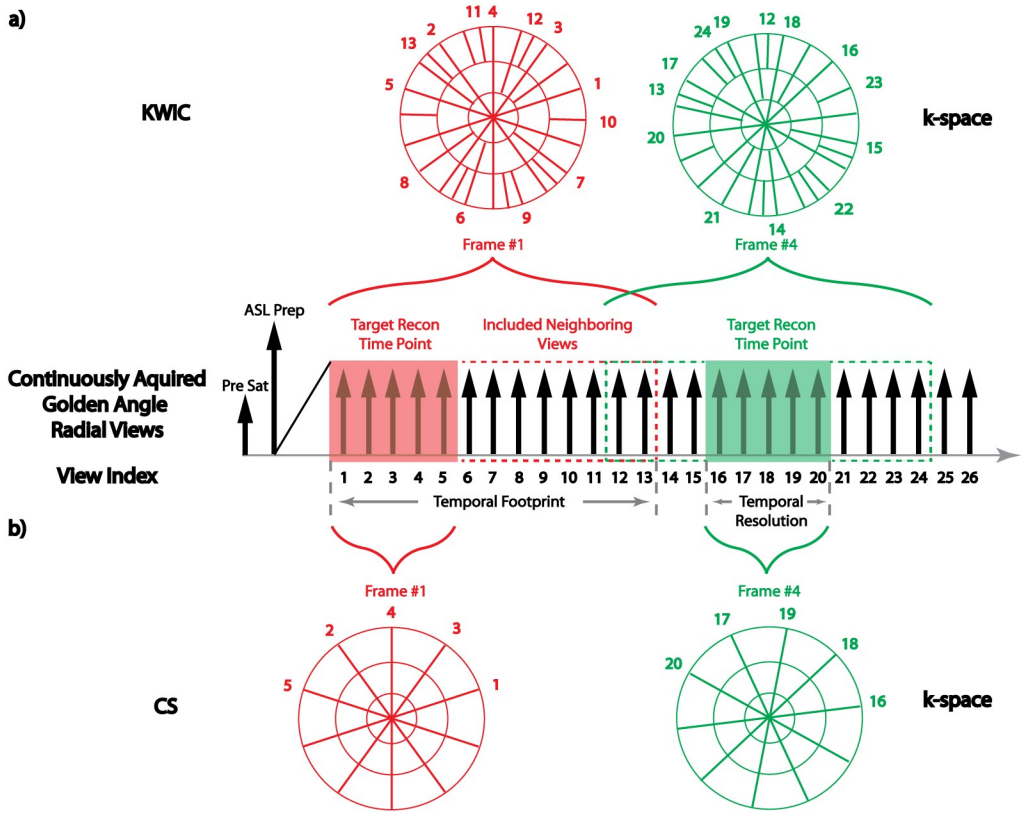

Figure 5-1 Sequence diagram of 3D SOS NCE-dMRA, which combines ASL with a continuous golden-angle bSSFP readout. An example of data binning with KWIC filtering and CS reconstruction is also shown in a) and b), respectively. In KWIC, K-space is divided into 3 regions, with 5 views (size of the target reconstruction time point) in the center region, 8 views in the middle region, and a total of 13 views in the outer region. For frame #1, included neighboring views (8 views) all reside on one side. For frame #4, included neighboring views symmetrically reside on both sides. In CS reconstructions, neighboring views are not included. Each frame only contains 5 views without overlapping with each other.

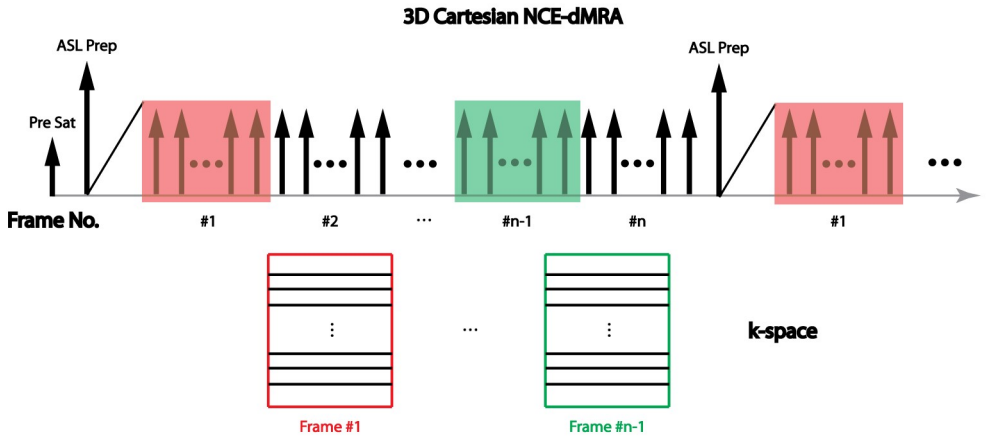

Figure 5-2 Sequence diagram of 3D Cartesian NCE-dMRA, which applies an ASL preparation pulse followed by a segmented multi-phase balanced steady-state free precession (bSSFP) readout. A pre-saturation pulse is applied before the ASL preparation pulse to saturate the background signal in the imaging slab. Segmented k-space is acquired in each repetition time, and the temporal resolution depends on the number of lines per segment.

5.2.2 Image Reconstruction

Each golden-angle SOS NCE-dMRA dataset was binned into 20 views per frame, i.e., a temporal resolution of 97ms, and reconstructed with the aforementioned three CS strategies respectively: MS-CS (Equation 5-1), iCS (Equation 5-2), and CS-CS (Equation 5-3). For demonstration purpose, one dataset was binned to 10, 20, and 30 views per frame separately and reconstructed with the MS-CS algorithm. The radials views in this demonstration reconstruction were aligned in such a way that the 10 views in the 10-view reconstruction corresponded to the middle 10 views of the 20-view reconstruction, and the 20 views in the 20-view reconstruction corresponded to the middle 20 views of the 30-view reconstruction. In addition, each dataset was binned using the KWIC method and reconstructed with the standard gridding reconstruction (107) with a k-space temporal filter described in (95), to reduce possible temporal blurring effect. The specific parameters of KWIC reconstruction were chosen based on the previous study (97): 20 views at the k-

space center, 40 more views were added in each outward adjacent annular ring region, with a total of 5 rings and 160 views per frame for the outer-most ring.

All CS image reconstruction algorithms were implemented based on the Berkeley Advanced Reconstruction Toolbox (51). The regularization parameters were determined based on a pilot study on two volunteers for parameter optimization. Specifically, we normalized the data sets prior to reconstruction and varied the regularization parameter(s) in each method from 0.05 to 1.0 in a step size of 0.05 to identify the optimal value(s) that would provide the best image quality by visual assessment among the reconstructed images for each method. Selected regularization parameter(s) for the three CS reconstructions were: $\lambda = 0.1$, $\mu = 0.4$ for MS-CS; $\lambda = 0.4$ for iCS; and $\lambda = 0.2$ for CS-CS. After the reconstruction of all image slices, label and control images were subtracted (except for CS-CS method in which the subtracted image is directly reconstructed) and maximum-intensity-projection (MIP) images along axial, coronal, and sagittal planes were generated.

5.2.3 Image Evaluation

The image quality of the three CS as well as the KWIC reconstructions were subjectively graded independently by two reviewers (both are MRI experts with over seven years of experience). Images were evaluated in terms of vessel delineation and artifacts/noise on a 4-point scale: 1. Poor delineation of all-sized arteries, with severe streaking artifact and noise leading to nondiagnostic images; 2. Confident delineation of large arteries (M1, P1/2), but with considerable artifacts and noise that compromise the evaluation of intermediate and small arteries (M2,3,4 and P3,4); 3. Confident delineation of large and intermediate arteries (M1,2, and P1,2), with little artifacts and low noise level that only impairs the definition of the fine structures of small vessels (M3,4 and P3,4); 4.

Confident delineation of all-size arteries (M1,2,3,4 and P1,2,3,4) with minimal artifacts and noise.

To evaluate the performance of the proposed MS-CS method on the temporal delineation of dynamic blood flow, we defined a weighted arrival time (wAT) as follows (108):

$$wAT = \frac{\sum_t I(t)*t}{\sum_t I(t)} \quad (5\text{-}4)$$

where $I(t)$ is the signal intensity at time t. Quantitative wAT maps were calculated from MS-CS and KWIC reconstructions as well as the reference Cartesian acquisition. Five regions of interest (ROIs) encompassing different vascular regions (M1, M2, M3/4, P1/2, P3) were manually drawn on the calculated wAT maps, from which average wAT values were measured using the following method: An intensity threshold was set for each region such that the intensity of the smallest visible vessels within the region were above the threshold. The threshold was then used as a mask to exclude pixels with signal intensity below the threshold. wAT values from the remaining pixels were then averaged and reported as the final wAT value for the region.

Signal-to-noise ratio (SNR) and contrast-to-noise ratio (CNR) were also calculated for MS-CS, KWIC and Cartesian reconstructed images, using the approach previously described (97). Specifically, a 16x16 square ROI was drawn on the M1 vessel and adjacent background from a MIP image that corresponds to the signal peak in each time series. All pixels were then averaged to determine the mean signal. Average noise level was calculated by taking the standard deviation of a background ROI placed far away from brain to avoid any motion or reconstruction related artifacts. SNR was then calculated as the ratio of the

mean signal to the standard deviation of background noise. As for CNR measurement, the M1 signal used in SNR measurement were subtracted by the brain tissue signal that measured from a ROI placed between the middle and posterior cerebral arteries where vessels were absent. The resulting signal difference was then divided by the standard deviation of background noise to calculate CNR.

5.2.4 Statistical Analysis

For subjective image quality scores, a Friedman test was performed among the four reconstructions to detect statistically significant differences. Post-hoc analyses with Wilcoxon signed-rank test were subsequently conducted to detect pairwise differences. For wAT, statistical significance for each ROI was determined between the three reconstructions using a repeated-measures analysis of variance (ANOVA) followed by a post-hoc paired t-test for the pairwise comparisons. In all the statistical pairwise comparisons, the null hypothesis was that there was no significant difference in image quality scores or wAT values between the two techniques. A two-tailed $P<0.05$ was considered statistically significant. The weighted kappa coefficient was used to evaluate the inter-observer agreement for the quality score. All statistical analyses were conducted using R software (version 3.3.1).

5.3 Results

All scans were successfully performed. The Cartesian dMRA images were directly reconstructed using the vendor-provided program. The MS-CS, iCS, CS-CS and KWIC reconstructions of the golden-angle SOS data took on average 4.7 minutes, 2 minutes, 1.3 minutes and 30s for the calculation of each temporal frame, respectively.

Figure 5-3 demonstrates the effects of different regularization terms on the proposed MS-CS method. The image reconstructed without any regularization (lower right), which is equivalent to the SENSE reconstruction, has the lowest SNR and inferior vessel delineation. Adding one regularization term was able to improve the image quality; however, the image with magnitude subtraction alone (lower left) had fewer streaking artifacts and lower noise level than the one with wavelets alone (upper right). Combing both regularization terms (upper left) further improved vessel delineation especially of fine structures.

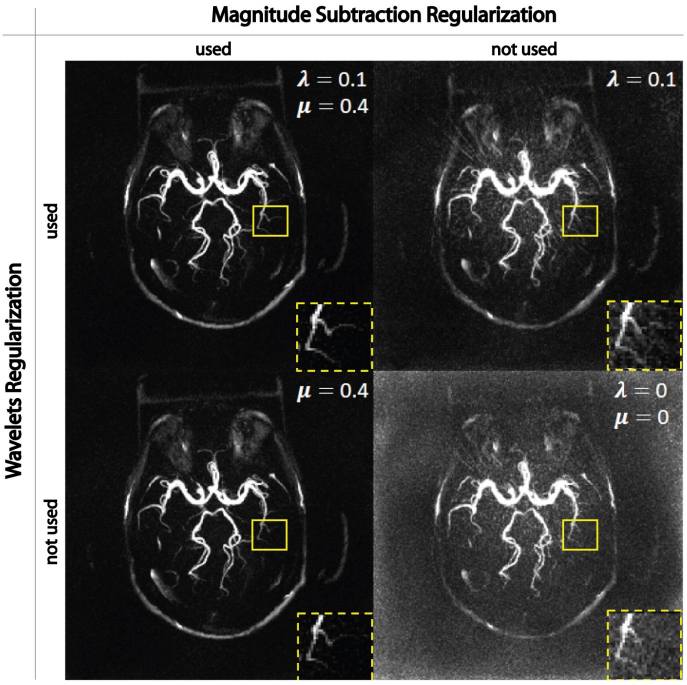

Figure 5-3 Demonstration of the contributions of magnitude subtraction regularization and wavelets regularization in the proposed MS-CS method. Without any regularization (lower right), reconstructed image has high noise level and suffers the loss of fine structures. By adding a single regularization term, image quality is significantly improved, although using magnitude subtraction (lower left) shows more improvement than wavelets (upper right). Combining the two regularizations provides the best image quality among all combinations. All images were normalized by its maximum intensity and displayed at the same window level.

Figure 5-4 illustrates four selected temporal frames of dMRA reconstructed with three different number of views per frame using the proposed MS-CS reconstruction. With 10 views per frame, the reconstructed images show residual streaking artifacts (red arrows) and increased background noise that precludes the visualization of small-sized vessels (yellow arrows). With 20 views per frame, the reconstructed images provide good image quality with sufficient SNR and adequate delineation of different vessels. With 30 views per frame, the reconstructed images demonstrate even better SNR that provides detailed delineation of all sizes of vessels. However, a wider reconstruction window would result in lower temporal resolution that may not capture sufficient temporal information. Based on visual inspection, the choice of 20 views per frame represents a good balance between image quality and temporal sampling rate.

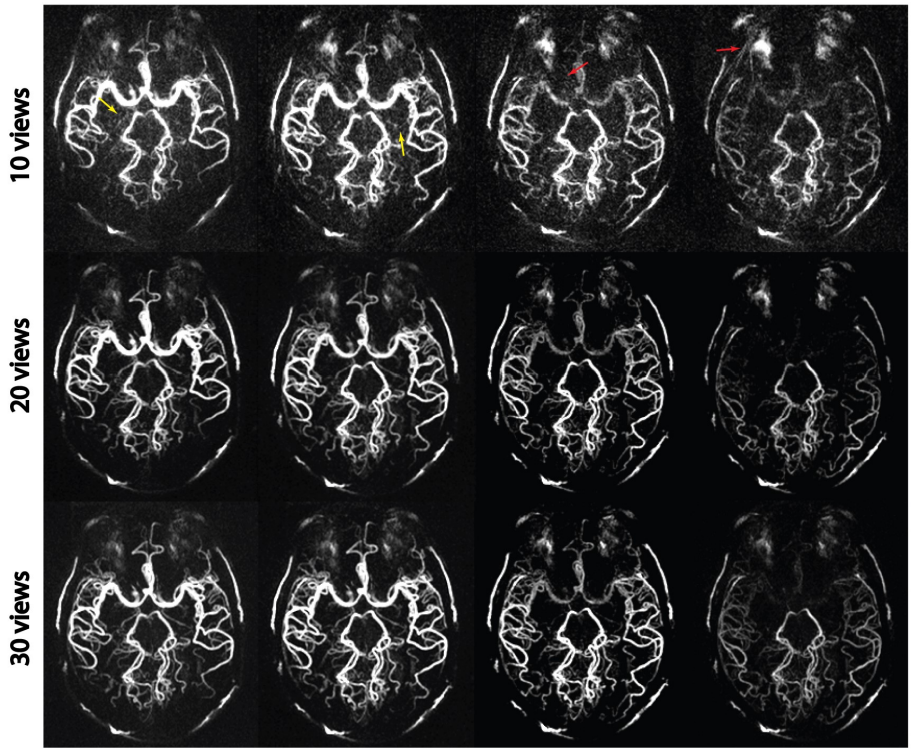

Figure 5-4 MIP images of a golden-angle SOS acquisition reconstructed with the MS-CS method using 10 views, 20 views and 30 views per frame. With 10 views per frame, increased noise (yellow

arrow) and residual streaking artifacts (red arrow) are noted in the images. With 20 views per frame, reconstructed images provide adequate delineation of different sizes of vessels. With 30 views per frame, the reconstructed images have even better SNR, but a wider reconstruction window potentially results in a reduced temporal resolution. The use of 20 views represents a good balance between image quality and temporal resolution.

Figure 5-5 compares the three CS reconstruction strategies on one volunteer at four temporal frames. The conventional iCS reconstruction (middle row) shows residual streaking artifacts (yellow arrow) and fails to recover fine structures (red arrows), as it does not benefit from the subtraction sparsity. This is also reflected in the subjective quality scores in Table 5-1, where iCS had the lowest score (2.75 ± 0.62) among all reconstruction strategies. The CS-CS reconstruction uses the additional information in complex subtraction regularization, and this indeed reduced the streaking artifact, with a slightly higher score (2.83 ± 0.57), although no statistical significance was reached ($P=0.38$). However, due to the increased sensitivity to phase errors in complex subtraction, the CS-CS reconstruction suffers from loss of SNR, resulting in slightly increased noise level that submerged fine anatomical details (green arrows). The proposed MS-CS reconstruction was able to reconstruct images with clean background, sharp contrast, and adequate details. This improvement was confirmed by a significant higher score (3.83 ± 0.38 vs. 2.75 ± 0.62 vs. 2.83 ± 0.57, $P<0.05$) when compared with both iCS and CS-CS. The MS-CS image quality scores were comparable to that of KWIC reconstruction (3.83 ± 0.38 vs. 3.78 ± 0.39, $p=0.21$). Scores from the two raters had moderate to excellent agreement, depending on the imaging and reconstruction techniques.

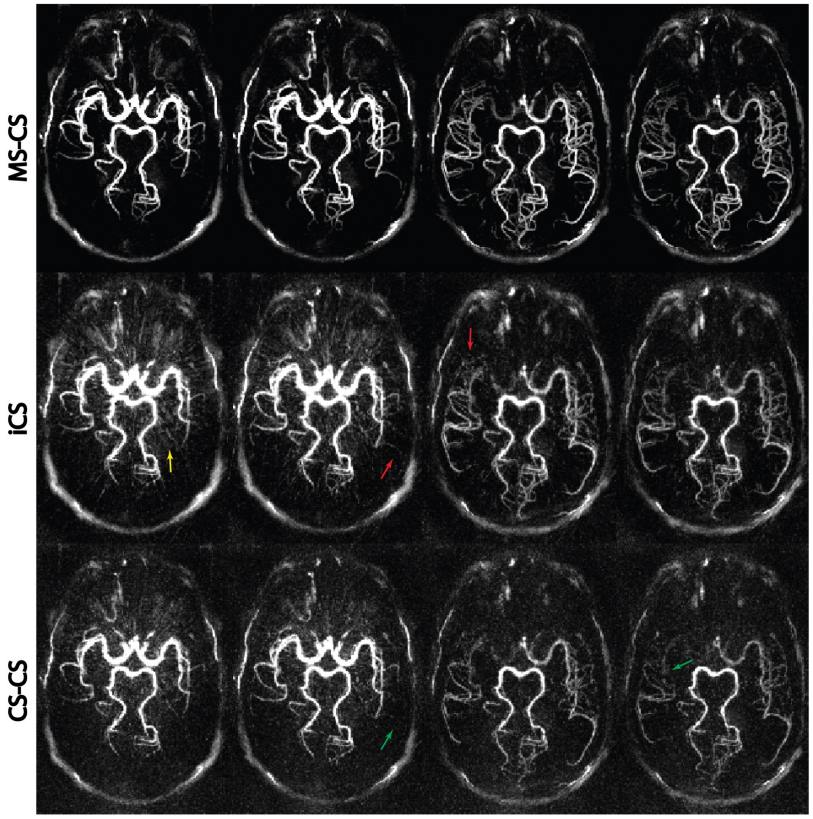

Figure 5-5 Comparison of the three CS reconstruction strategies. From top to bottom, each row represents axial MIP images at four time frames reconstructed with MS-CS, iCS, and CS-CS, respectively. Severe streaking artifacts and high noise level are clearly visible on the iCS and CS-CS reconstructions, while the proposed MS-CS reconstruction provides cleaner and sharper images. All images were normalized by its maximum intensity and displayed at the same window level.

Table 5-1 Subjective image quality scores and weighted kappa coefficients κ for different imaging techniques. a, $p<0.05$ (compared with iCS and CS-CS); b, $p<0.05$ (compared with iCS and CS-CS). No significance was detected between MS-CS and KWIC, and between iCS and CS-CS.

	MS-CS	**iCS**	**CS-CS**	**KWIC**
	1	2	3	4
Image Quality	3.83 ± 0.38^{a}	2.75 ± 0.62	2.83 ± 0.57	3.78 ± 0.39^{b}
κ	0.83	0.92	0.85	0.82

Figure 5-6 shows the comparison of KWIC and MS-CS reconstruction, as well as the reference Cartesian acquisition. Overall, good to excellent dMRA image quality was achieved with both KWIC and MS-CS reconstructions. However, differences were evident in the dynamics of blood flow in certain regions between the two reconstructions. KWIC reconstruction showed early filling of distal branches of middle cerebral artery (MCA) (M3,4) and posterior cerebral artery (PCA) (P3) (yellow arrows) at the first two frames. It also had a delayed drainage of middle branches of MCA (M2) and PCA (P1/2) (green arrows) at the last two frames. At the corresponding positions mentioned above (red and blue arrows), the presence of arteries in MS-CS reconstruction matched well with the reference Cartesian acquisition. The average SNR (±standard deviation) and CNR of the MS-CS reconstruction of all healthy volunteers were 61.5(±3.3) and 53.9(±4.5), respectively, 63.2(±5.2) and 56.4(±3.8) for KWIC reconstruction, and those of Cartesian were 89.6(±4.6) and 82.3(±5.7).

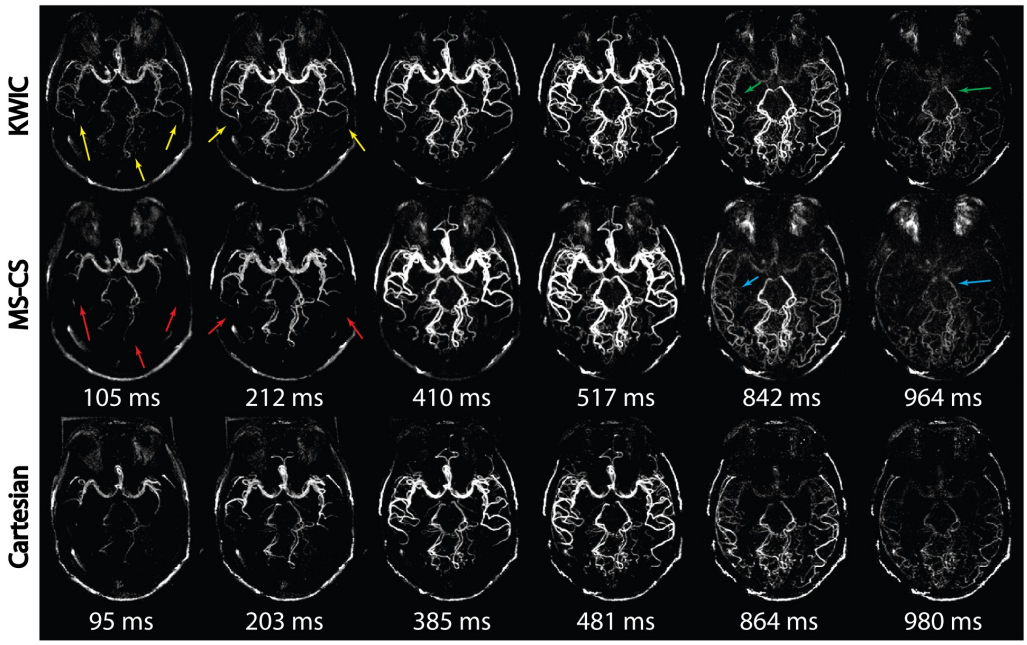

Figure 5-6 MIP images of KWIC reconstruction, MS-CS reconstruciton and Cartesian reference acquisition at six frames. Comparable image quality without visible streaking artifacts was obtained by KWIC and CS-CS reconstructions. However, the view-sharing in KWIC caused early filling (yellow arrows) and late drainge (green arrows) of small vessels at different regions, while the proposed method provided improved temporal delineation (red and blue arrows) comparable to Cartesian acquisition.

Figure 5-7 shows comparisons of temporal MIP (tMIP) as well as the wAT maps for KWIC and MS-CS reconstructions and Cartesian acquisition from one representative volunteer. The tMIP images showed similar spatial information of vascular structures across the three techniques. However, the wAT maps exhibited visible differences in intermediate to distal MCA (blue arrow) and the entire PCA (green arrow) regions. ANOVA tests confirmed this observation with $P<0.05$ in M2, M3/4, P1/2 and P3 regions, but $P=0.13$ in M1 region. The wAT values for different ROIs and reconstructions, as well as the P values for pairwise comparisons are listed in Table 5-2. This result suggests that view-sharing in KWIC affects medium- to small-sized vessels (M2, M3/4, P1/2 and P3) and large-sized vessels (M1) in different ways.

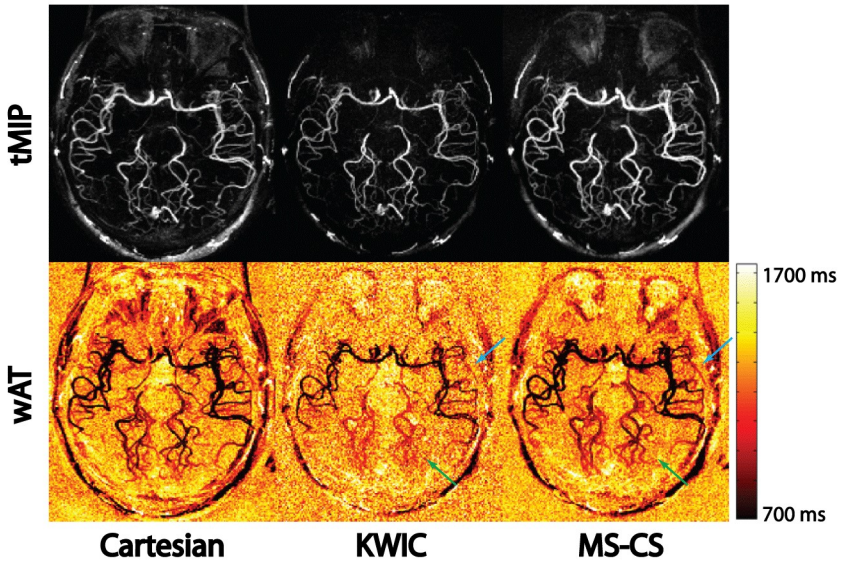

Figure 5-7 tMIP and wAT maps of Cartesian acquisition, KWIC reconstruction and MS-CS reconstruction from one volunteer. tMIP confirms minimal image quality difference between the three techniques. However, the wAT maps show significant differences in the MCA and PCA regions (blue and green arrows) between KWIC and the proposed method, while the proposed method generated comparable results with the reference Cartesian acquisition.

Table 5-2 wAT values for different vessel segments and imaging techniques. Unit of wAT is millisecond (ms). a, $p<0.05$ (compared with Cartesian and MS-CS). (MCA segments: M1, from the origin to bifurcation/trifurcation; M2, insular segment, from bi(tri)furcation to circular sulcus of insula; M3/4: opercular and cortical segment; M4: cortical segment. PCA segments: P1: from it origin at the termination of the basilar artery to posterior communicating artery (PCOM), P2: from the PCOM around the mid-brain; P3: quadrigeminal segment; P4: cortical segment.)

Segments	Cartesian	KWIC	MS-CS
	1	2	3
M1	1056.3	1048.2	1051.5
M2	977.7	1039.2[a]	978.2
M3/4	1095.6	1135.6[a]	1089.7
P1/2	1100.1	1180.2[a]	1097.5
P3	1138.3	1202.9[a]	1136.1

Figure 5-8 demonstrates NCE-dMRA acquired on an AVF patient with the proposed MS-CS and KWIC reconstructions, respectively. TOF and DSA images are also displayed as a reference. A left dural AVF was detected, where blood flows directly from the feeding artery (anterior branch of middle meningeal artery) into the transverse sinus bypassing the capillaries at a high flow velocity. MS-CS sequentially showed feeding artery (red arrow), fistula site (green arrow) and drainage into sinus (blue arrow), while such temporal information was lost in KWIC images and all the lesion components are displayed simultaneously. The signal intensity curves derived at three regions of interest (ROIs), shown in Figure 5-9 also support this observation: KWIC reconstruction generated wider curves at two ROIs with fast flow, while at the other ROI with relative slow flow, shape and peak position of the signal intensity curves from KWIC and MS-CS were similar.

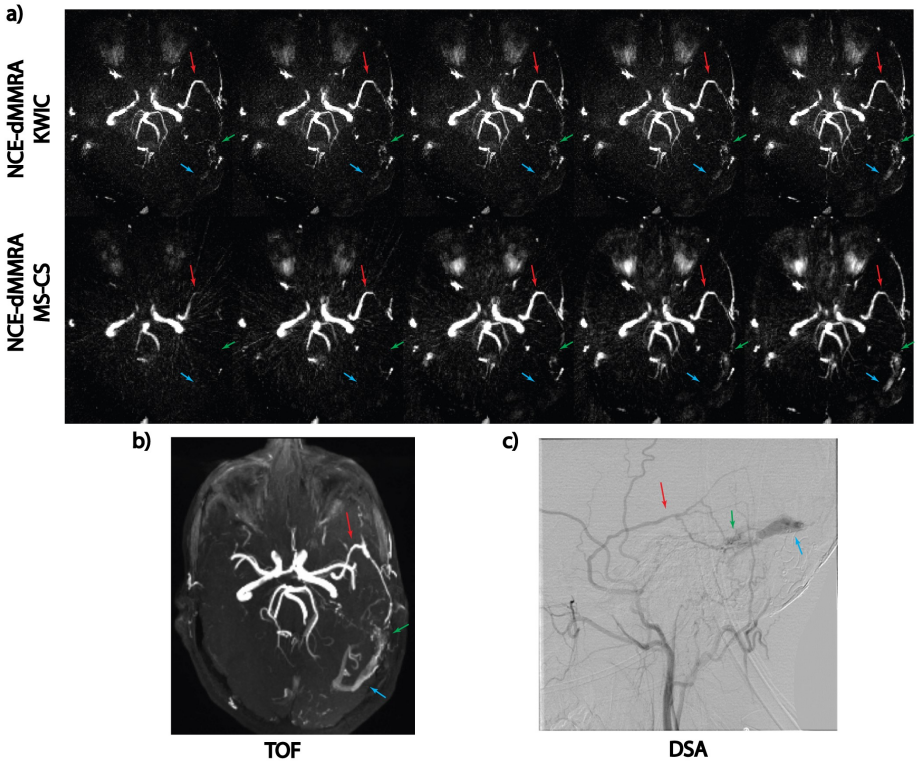

Figure 5-8 a). Example NCE-dMRA images of a AVF patient. From top to bottom, each row represents five frames of dynamic images reconstructed with KWIC and MS-CS, respectively.

Images from MS-CS reconstruction sequentially display feeding artery (red arrow), fistula site (green arrow) and drainage into sinus (blue arrow). Such dynamic information is not as obvious in the KWIC reconstruction. b,c). Reference TOF and DSA images.

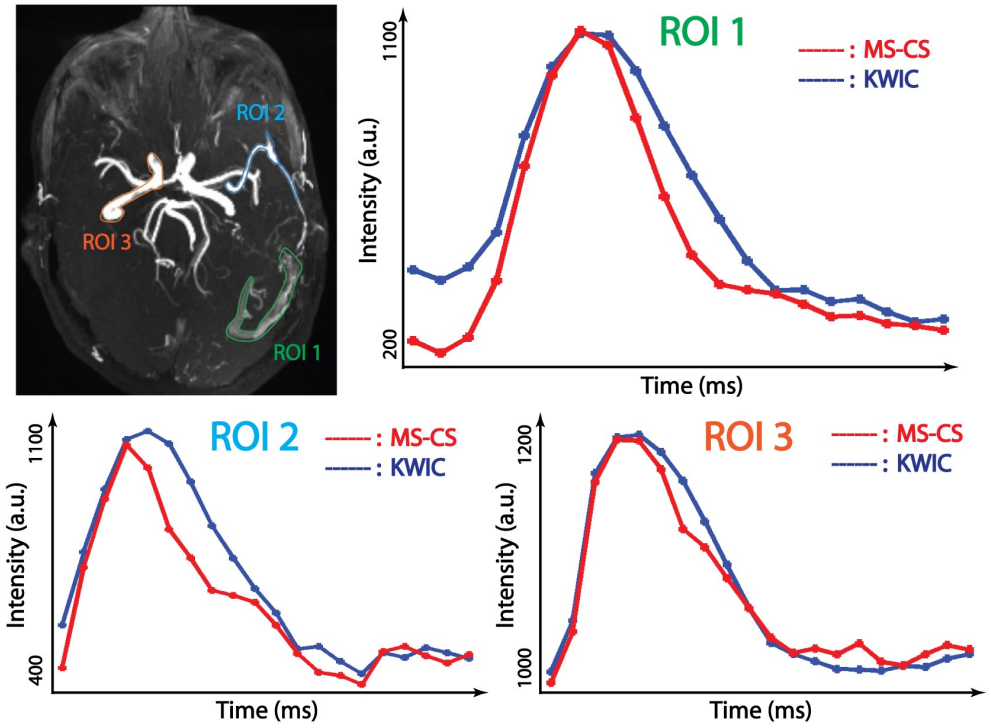

Figure 5-9 Intensities of signal at three ROIs, shown in the upper left sub-figure, are plotted against time for the KWIC and MS-CS reconstructions. For ROIs 1 and 2, which contain vessels with fast flow, view-sharing of KWIC reconstruction causes early filling and late drainage. For ROI 3 that contains the main branch with relative slow flow, both reconstructions have similar signal intensity curves.

Since our radial acquisition took only half of the scan time of Cartesian acquisition, it allowed doubling of the spatial coverage within the same scan time. Figure 5-10 displays five frames of a 64-slice 3D SOS acquisition with 1x1x1mm^3 isotropic resolution, which enabled high quality MIP images in sagittal, coronal, and axial views. The detailed vascular structure is also displayed as a reference by TOF. One can appreciate the cleaner dynamic information provided by the high-quality MS-CS reconstruction compared with KWIC reconstruction.

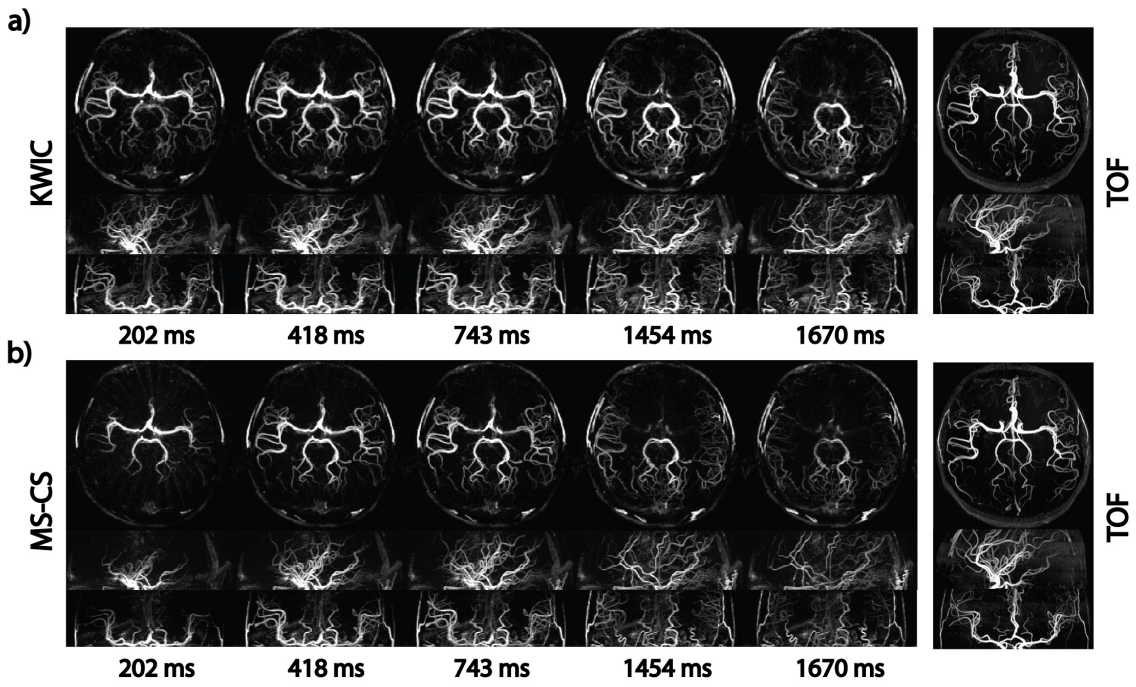

Figure 5-10 Example images of a 64 slices golden-angle SOS acquisition reconstructed with KWIC (a) and the proposed MS-CS method (b) in sagittal, coronal and axial views. Static TOF image is shown as an anatomical reference. The 1x1x1mm^3 isotropic resolution allows high quality MIP images in all three views to be reconstructed with KWIC and MS-CS methods. However, temporal smoothing of distal arteries can also be observed in all three planes in KWIC reconstruction, while the proposed method showed reduced temporal blurring and improved delineation of signal evolution in small arteries.

5.4 Discussion

Our work demonstrates the feasibility of applying MS-CS to accelerate NCE-dMRA with golden-angle stack-of-stars trajectory. Compared with the previous Cartesian acquisition, SOS NCE-dMRA was already shown to achieve a shorter scan time. By taking advantage of the magnitude subtraction sparsity of control and label images, the MS-CS method allows high spatial (~1mm^3) and temporal (~100ms) resolution NCE-dMRA within a short scan time (~3min). We further demonstrated the MS-CS reconstruction is superior to both iCS and CS-CS strategies in NCE-dMRA. Comparison with the previously proposed KWIC method was also performed. Our results suggest MS-CS is capable of

providing high temporal resolution images by reducing the number of radial spokes for each temporal frame without using view-sharing.

Compared to the conventional iCS reconstruction, where the control and label images are reconstructed independently before subtraction, the proposed method reconstructs both images in a joint optimization. Since the final dMRA image is generated by the subtraction between control and label acquisitions in ASL based MRA, the incorporation of magnitude subtraction in image reconstruction will highlight the labeled blood signal and effectively suppress the background signal including artifacts. On the other hand, from an algorithm perspective, the use of such an additional regularizer can further reduce the solution space and allow a higher likelihood to converge to an optimal solution (i.e. clean and sharp image). As another choice, complex subtraction in k-space between control and label acquisitions can be used to enhance the subtraction sparsity. However, we have shown in our work that this CS-CS method is inferior to the proposed MS-CS method for NCE-dMRA, due to the following two reasons: 1). Direct complex subtraction imposes signal to noise ratio (SNR) penalty and causes noise amplification; 2). MRA is based on the blood magnitude enhancement but complex subtraction partly depends on phase variation, and therefore, is sensitive to phase errors that come from system imperfection induced gradient delay, off-resonance effects raised from field inhomogeneity, as well as subtle motion between label and control acquisitions. Compared with the conventional Cartesian trajectory, the use of radial trajectory in our study also increases the sensitivity of data acquisition to these phase errors.

A previous study has successfully implemented KWIC reconstruction in NCE-dMRA with golden angle radial acquisition (97). With k-space view-sharing of adjacent temporal

frames, reconstructed image series have both high spatial and apparent temporal resolution. As demonstrated in this work, both proposed MS-CS method and KWIC showed good image quality without apparent streaking artifacts. However, view-sharing in KWIC can potentially lead to temporal smoothing of underlying flow dynamics at certain locations, such as vessels with fast flow. This would be a limiting factor in certain clinical applications. For instance, it will be difficult to capture the flow dynamics in feeding arteries with fast flow or distinguish between feeding arteries and cortical venous reflux needed for Borden classification (109) in arteriovenous fistula (AVF). As illustrated in the AVF case (Figure 5-8 and 5-9), in which abnormally fast flow appears in a small-size fistula site, KWIC failed to capture the full passage of blood flow from the feeding artery into the fistula and vein. This is due to the fact that small structures are mainly represented by high spatial frequencies in k-space, which are heavily shared between neighboring frames in KWIC reconstruction. On the contrary, the proposed MS-CS requires no view-sharing, and therefore preserves the temporal information.

In terms of SNR and CNR measurements, the proposed MS-CS approach has a similar performance compared with KWIC reconstruction. However, both radial-based reconstructions had significantly lower SNR and CNR compared with Cartesian acquisition. This matches our previous result (97). Aside from the reason mentioned in (97), which ascribed the difference to a k-space apodizing filter along the slice encoding direction for Cartesian online reconstruction, it is also well-known that radial acquisition has intrinsically low SNR efficiency compared with Cartesian acquisition (110). Considering that the acquisition time for the 3D SOS radial sequence is only half of that of the 3D Cartesian sequence, such difference is expected. Another thing to notice is that since

CS reconstruction is always an iterative nonlinear process, artificially high SNR and CNR can be created by manipulating regularization parameters. Therefore, care should be taken for the interpretation and evaluation of the SNR and CNR measured from MS-CS approach.

In the proposed reconstruction algorithm, the widely-used Wavelet regularization and application-tailored magnitude subtraction regularization are incorporated (45). We note that an inappropriate use of wavelets could lead to blurring of fine structures, due to the suppression of high frequency component in wavelets domain during the denoising (i.e. soft-thresholding) process. On the other hand, the magnitude subtraction regularization does not specifically penalize the high frequency component, since denoising is carried out in image domain and only signals with low amplitude are removed. To balance the two terms and prevent over-smoothing or insufficient artifact removal, we carefully tuned the associated regularization parameters. We found that both regularization terms contribute to final high quality images, although the majority of regularization comes from the proposed magnitude subtraction term whereas the wavelet term offered incremental improvement in image quality. We also note that our acquisition uses high under-sampling factor and has limited SNR. Under such circumstance, parallel imaging (PI) alone cannot guarantee to recover high quality image due to the ill-condition of the inverse problem in PI (3,4). Therefore, we included additional regularization terms in our optimization problem, although this came at a price of much longer reconstruction time and higher computation burden due to the iterative reconstruction.

Magnitude subtraction was originally introduced in the reconstruction of under-sampled CE-dMRA data sets (45). To apply it on SNR-limited ASL based NCE-dMRA, several optimizations were performed to compensate for the SNR difference. First, parallel

imaging was incorporated in the image reconstruction to utilize the dense coil arrays, e.g. 20 channels were used in this study. Second, a non-Cartesian radial trajectory was chosen to maximize the incoherence of artifacts when k-space is highly under-sampled. The intrinsic variable density sampling feature of radial-sampling also benefits the performance of CS algorithms. Third, the regularization parameters were carefully tuned using several NCE-dMRA data sets in a pilot optimization study. They are drastically different than the ones used in (45), reflecting the signal level difference between these two studies.

In order to further improve temporal resolution, aside from investigating various advanced reconstruction strategies that allows further reduction of the number of spokes used per phase, an alternative solution is to sample the 3D k-space more efficiently with the SOS acquisition. In the current implementation, the angle of radial spokes does not vary in the partition direction. Several previously proposed methods such as SOS-CAIPIRINHA (111) and rotated stack-of-stacks (9) vary the angles of the radial spokes in the partition direction and demonstrated improved result. By varying the angle distribution along the partition direction and combining the proposed MS-CS reconstruction, it is possible to further push temporal resolution without sacrificing spatial resolution.

Balanced SSFP (bSSFP) has been successfully used for 4D NCE-dMRA data acquisition by providing high SNR and imaging efficiency. However, it is intrinsically prone to off-resonance artifacts especially near sinuses. To minimize the off-resonance artifacts, a pre-saturation pulse was applied before the image acquisition to suppress the background tissue signal as well as the off-resonance induced artifacts. Furthermore, the ASL-based dMRA technique benefits from the subtraction between control and label images, which can effectively remove the off-resonance artifacts in subtracted dMRA

images. Meanwhile, a tilted axial acquisition slab was carefully placed to avoid covering most of the sinuses, which further reduced the off-resonance artifacts. Therefore, the off-resonance artifact was not an issue in the current study.

Our study has limitations. First, our main goal was to demonstrate the feasibility of applying CS on ASL and evaluate its effect on reducing view-sharing, we did not perform any SNR and CNR analysis and comparison. This is particularly important for calculating hemodynamic parameters such as cerebral blood flow (CBF), and cerebral blood volume (CBV). A systematic evaluation needs to be developed in the future. Second, the proposed method was only evaluated on limited number of patients. Future evaluation of the clinical utility of NCE-dMRA with MS-CS reconstruction in a large cohort of patients is warranted. In addition, developing an online reconstruction pipeline (8) assembled with faster imaging reconstruction is needed to facilitate its clinical utility.

5.5 Conclusion

In conclusion, by taking advantage of magnitude-subtraction sparsity of the ASL based MRA, a CS algorithm has been successfully implemented and evaluated in golden-angle stack-of-stars NCE-dMRA. Better image quality was achieved using the proposed MS-CS than the conventional iCS and CS-CS methods. Compared to the previous KWIC method, the proposed MS-CS strategy allows more accurate temporal depiction of cerebral flow patterns without view-sharing, which may become a useful approach in clinical applications.

Chapter 6 Improved Volumetric MRI using Radial Trajectory

In Chapter 5, we utilized the 3D stack-of-stars trajectory to improve the incoherence of artifacts when 3D k-space is heavily under-sampled. However, the capacity of generating incoherent sampling with conventional 3D stack-of-star trajectory is not fully exploited. In this chapter, we introduce a modified stack-of-star trajectory that provides reduced streaking artifacts and improved image quality for general 3D volumetric imaging. It is analyzed from theoretical point of view and demonstrated on three different applications to shows the efficacy.

6.1 Introduction

Radial sampling is a widely used k-space sampling trajectory for fast MRI. It offers several advantages compared with Cartesian k-space sampling, including improved robustness in the presence of motion (14) due to continuous update of the k-space center, and its suitability for high under-sampling factors due to its relatively benign under-sampling artifacts (112). The disadvantages of radial sampling include decreased SNR efficiency (110), increased sensitivity to system imperfection and trajectory errors (113–115), and more complex image reconstruction (116). Radial sampling has been used in many MRI applications, such as MR angiography (112,117), cardiac imaging (118), phase-contrast imaging (119) and abdominal imaging (120). To acquire 3D k-space data using radial sampling, two acquisition strategies are commonly available: 3D stack-of-stars (SOS) (112) and 3D radial (Koosh-Ball) (117,118).

In conventional 3D SOS acquisition strategies (102,112,121), the azimuthal angle of the radial spokes does not vary in the partition (i.e. 3D Cartesian phase encoding) direction such that if a radial spoke with angle θ is sampled in one partition, it is also sampled in all the other partitions. Recently, Chen L et al. (122) and Wech T et al. (123) proposed to rotate the radial spokes along the partition (slice) direction, but both did not provide sufficient implementation details on how the radial spokes were rotated. Other approaches such as SOS-CAIPIRINHA (111) and rotated stack-of-spirals (124) vary the angle of the radial spokes or spiral interleaves in a linear fashion in the partition direction; however, we show in this report that such a strategy is sub-optimal. We propose a rotated SOS (RSOS) sampling method in which radial spokes are rotated in a golden-ratio (94) fashion in the partition encoding direction, i.e. RSOS-GR. We show that our RSOS-GR strategy creates varying aliasing patterns along the partition direction, and such a varying aliasing pattern improves the condition of the inverse problem in a parallel imaging reconstruction and improves the incoherence of the sampling function in a compressed sensing reconstruction. We compare the conventional aligned SOS (ASOS), RSOS with a linear rotation in the partition direction (RSOS-Linear), and the proposed RSOS-GR using computer simulation, phantom and *in vivo* studies.

6.2 Methods

For the sake of simplicity and clarity, we only consider two common cases of in-plane view order in radial sampling: linear and golden angle (94), as our work mainly pertains to the angle variations in the partition direction. It is straightforward to generalize the proposed RSOS approach to more sophisticated in-plane radial sampling strategies such

as tiny golden angle radial sampling (125) and segmented golden angle radial sampling (126).

In this study, five different sampling strategies were studied: 1) conventional ASOS where all the partitions have the same radial spoke angles; 2) $RSOS_{(Lin)}$-Linear where the angle arrangement is linear both in-plane and across the partitions; 3) $RSOS_{(Lin)}$-GR, which is the proposed GR rotation in the partition direction applied to linear in-plane radial angles; 4) $RSOS_{(GR)}$-Linear, which includes GR in-plane radial spokes and linear rotation in the partition direction; 5) $RSOS_{(GR)}$-GR, which includes GR in-plane radial and the proposed GR rotation in the partition direction. An example of the radial spoke angle arrangement for all five strategies is shown in Figure 6-1. For in-plane linear view order, the angle θ_i of the i^{th} spoke out of total N_r spokes is calculated as: $\theta_i^L = \frac{\pi}{N_r} * (i-1), i = 1, 2, \dots, N_r$. For in-plane GR view order, the angle θ_i of the i^{th} spoke out of total N_r spokes is calculated as: $\theta_i^G = mod\left((i-1) * \pi * \frac{\sqrt{5}-1}{2}, \pi\right), i = 1, 2, \dots, N_r$. In the proposed GR rotation in the partition direction, non-zero azimuthal angle offsets that change across the partitions are introduced as follows:

$$\varphi_G(j) = mod\left((j-1) * \frac{\pi}{N_r} * \frac{\sqrt{5}-1}{2}, \frac{\pi}{N_r}\right), j = 1,2, \dots, N_{PE} \qquad (6\text{-}1)$$

where N_{PE} is the total number of partitions and j is the partition index. For the linear rotation in the partition direction, which is used in $RSOS_{(Lin)}$-Linear and $RSOS_{(GR)}$-Linear strategies, the azimuthal angle offsets are: $\varphi_L(j) = \frac{j-1}{N_{PE}} * \frac{\pi}{N_r}, j = 1,2, \dots, N_{PE}$. Based on the above definitions, the angle for the i^{th} radial spoke in the j^{th} partition will be θ_i^L for ASOS, $\theta_i^L + \varphi_L(j)$ for $RSOS_{(Lin)}$-Linear, $\theta_i^L + \varphi_{GR}(j)$ for $RSOS_{(Lin)}$-GR, $\theta_i^G + \varphi_L(j)$ for

RSOS$_{(GR)}$-Linear, and $\theta_i^G + \varphi_G(j)$ for RSOS$_{(GR)}$-GR. To reduce eddy currents and the resultant phase errors, spokes with the same in-plane index i (as defined above) in all partitions were acquired first before acquiring the next subset of spokes with index $i + 1$.

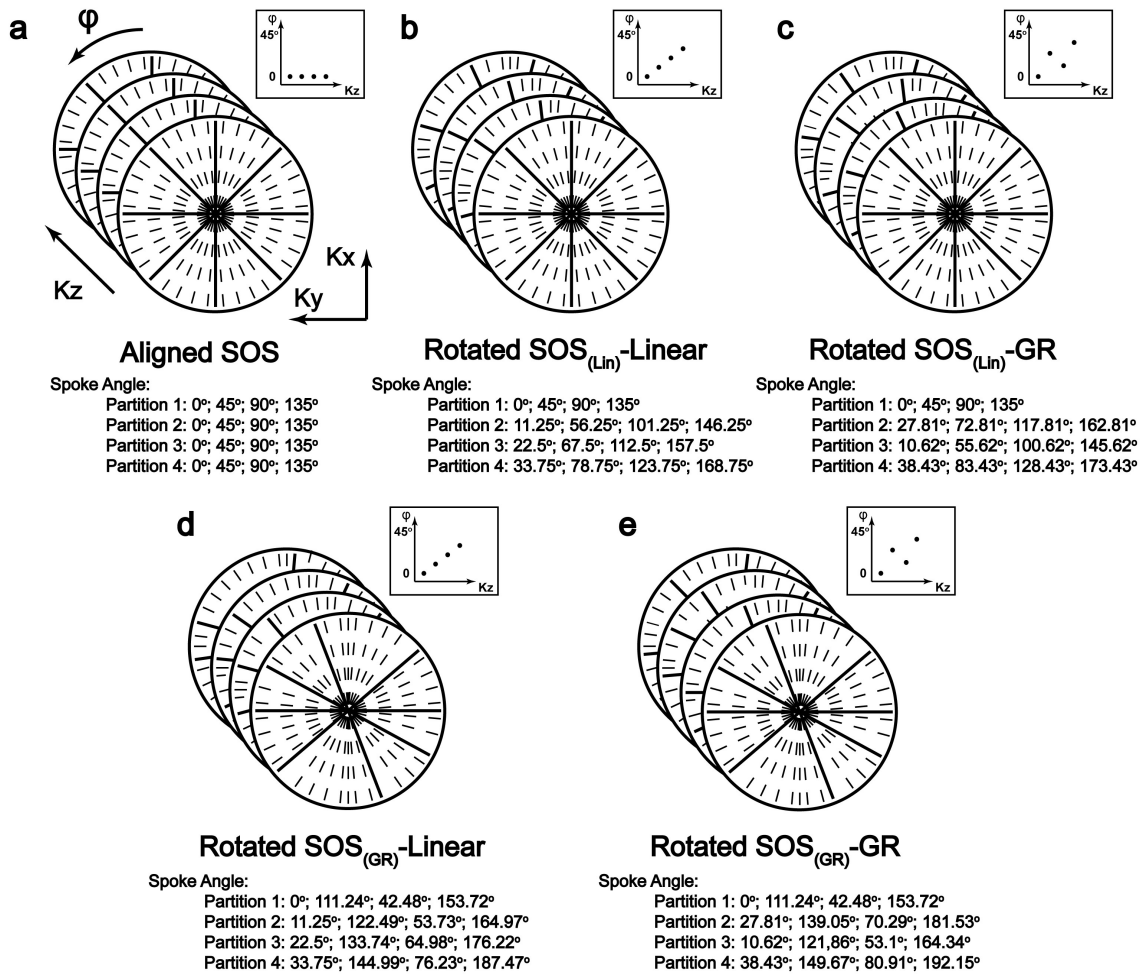

Figure 6-1 An example of the spoke angle arrangement using ASOS (a), RSOS$_{(Lin)}$-Linear (b), RSOS$_{(Lin)}$-GR (c), RSOS$_{(GR)}$-Linear (d), and RSOS$_{(GR)}$-GR (e). In this example, each partition has four spokes, and a total of four partitions. The calculated spoke angles are shown at the bottom of each sub-figure.

6.2.1 Computer Simulation

The point spread functions (PSF) of the conventional ASOS, RSOS$_{(Lin)}$-Linear, RSOS$_{(Lin)}$-GR, RSOS$_{(GR)}$-Linear and RSOS$_{(GR)}$-GR were first compared using simulations. The PSF for each of the five radial k-space trajectories was calculated following three steps:

1) Each sampled point was set to unit value; 2) The resultant k-space data were subsequently interpolated onto a Cartesian grid using a 3D Kaiser-Bessel kernel (107) in conjunction with appropriate density compensation derived from the Ram-Lak method; 3) The PSF was obtained as the Fourier transform of the gridded Cartesian k-space data. The k-space trajectory consisted of full spokes with base resolution of 256, partition number $N_{PE} = 36$ and was gridded onto a matrix size of 256x256x36. Spoke angles on each partition were calculated according to the aforementioned five strategies. The PSF calculation was performed for data sets with 20 to 100 radial spokes per partition in increments of 5 spokes to evaluate the effect of number of spokes on k-space sampling. The ratio of the main lobe magnitude of the PSF to the standard deviation of the PSF side-lobes magnitude (5) was calculated as a measure of the incoherence of the 3D PSF, which has been shown to affect the image reconstruction quality using compressed sensing algorithms (5,102). In cases where only gridding is used in the image reconstruction, the ratio of the main lobe energy to the sum of energy of side-lobes was calculated as an alternative incoherence measure of the PSF.

6.2.2 Phantom Experiment

To evaluate the performance of the proposed $RSOS_{(Lin/GR)}$-GR sampling strategy and compare it with ASOS and $RSOS_{(Lin/GR)}$-Linear, a 3D spoiled gradient recalled echo (GRE) sequence was modified to implement the five acquisition strategies. Phantom imaging and all in vivo studies in this work were performed on a 3.0T MRI scanner (Prisma, Siemens Medical Solutions, Erlangen, Germany). Relevant imaging parameters are listed in Table S1 in the online supporting materials. A fully-sampled reference data (400 spokes per partition, ASOS) and fifteen additional prospectively under-sampled data sets (20 spokes,

40 spokes, and 80 spokes per partition, using the aforementioned five strategies) were acquired. All acquired data were reconstructed with 3D gridding reconstruction as mentioned in the "Computer Simulation" section.

6.2.3 *In-vivo* Experiment

The five strategies were tested in three different applications: brain imaging, abdominal imaging, and dynamic MR angiography (dMRA) using arterial spin labeling (ASL) (97). The sequence used in brain imaging and abdominal imaging was identical to the one used in the phantom study, while the sequence used in dMRA-ASL imaging was modified based on a balanced steady-state free precession (bSSFP) sequence.

Brain imaging was performed on one healthy volunteer in axial orientation with a 20-channel head coil. Relevant imaging parameters are listed in Table 6-1. A fully sampled data and ten prospectively under-sampled data sets (40 spokes and 80 spokes per partition, using aforementioned the five strategies) were acquired. The five under-sampled data sets with higher under-sampling factor were acquired with 40 spokes instead of 20, due to the increased complexity of in-vivo structures compared with static phantom.

Abdominal imaging was performed on the same volunteer with a 12-channel body coil. Relevant imaging parameters are listed in Table 6-1. Five data sets with 40 spokes per partition using the aforementioned five strategies were acquired with a total scan time of 18s each during breath-holds.

DMRA-ASL imaging was performed on another healthy volunteer with a 20-channel head coil. Relevant imaging parameters are listed in Table 6-1. Due to the improved performance of $RSOS_{(Lin/GR)}$-GR over $RSOS_{(Lin/GR)}$-Linear and comparable performance between $RSOS_{(Lin)}$-GR and $RSOS_{(GR)}$-GR on previous experiments (shown in Result

section), only two data sets were acquired using ASOS and $RSOS_{(Lin)}$-GR with 20 spokes per partition per temporal phase, with a total of 10 phases.

Table 6-1 Imaging parameters in different applications. *: In radial sampling, the fully sampled Nyquist rate is: base resolution*pi/2. Acceleration factor here is therefore calculated as: acquired spoke number/radial Nyquist rate.

	Phantom Study	Brain Imaging	Abd. Imaging	ASL Imaging
Base Resolution	256	256	192	256
Partitions	64	32	56	32
Slice Thickness	1	1	2.5	1.5
FOV (mm^2)	250x250	250x250	300x300	256x256
TR/TE (ms)	3.41/1.82	3.41/1.82	3.52/1.51	4.7/2.35
FA (Degree)	12	12	12	25
Temporal Resolution	-	-	-	94

For the brain imaging and abdominal imaging experiments, acquired data sets were reconstructed with 3D gridding. To demonstrate the efficacy of RSOS in advanced image reconstruction methods, especially its advantage in SNR-limited application, acquired data sets in the dMRA-ASL imaging experiment were reconstructed with 3D gridding and a parallel imaging-compressed sensing (PI-CS) combined reconstruction method (8):

$$\hat{d} = \arg\min \sum_{i=1}^{N} ||\mathcal{F} S_i d - m_i||_2^2 + \lambda ||Rd||_1 \qquad (6\text{-}2)$$

where $\mathcal{F}$ is the non-uniform fast Fourier transform operator (NUFFT); S_i are the sensitivity maps estimated from the a fully-sampled pre-scan data using ESPIRiT method (50); d is the image to be reconstructed; m_i is the acquired under-sampled k-space data from each of the N receiver coil elements; R is spatial wavelets transform; and λ is the corresponding regularization parameter.

All reconstructions (gridding and PI-CS) were performed offline using a previously described tool (Berkeley Advanced Reconstruction Toolbox, BART) (51) on a Linux PC (4 Core/4GHz, 32 GB Memory, Nvidia GTX 760). For all the scans (phantom and in-vivo experiments), 40 initial calibration spokes along the x and y directions (0^o, 180^o, 90^o, 270^o, 10 spokes per angle) were additionally acquired and used in the image reconstruction to correct for system-dependent gradient-delay errors, as described in (115).

6.2.4 Data Analysis

For the phantom and brain imaging experiments, to compare different sampling strategies and different under-sampling situations quantitatively, both normalized root mean square errors (nRMSE) and structural similarity index (SSIM) were calculated between each slice of the reference images and images reconstructed from the under-sampled data acquired with the five strategies. The calculated nRMSE and SSIM were averaged across all slices. Whereas reduction in nRMSE indicates greater fidelity to the original image, perfect identicality is represented by a SSIM value of 1 and the SSIM value decreases as the images differ.

6.3 Results

6.3.1 Computer Simulation

Figure 6-2a shows the simulated PSFs in transversal (x-y plane) and coronal views (x-z plane) of fully-sampled and the under-sampled ASOS, $RSOS_{(Lin)}$-Linear, $RSOS_{(Lin)}$-GR, $RSOS_{(GR)}$-Linear and $RSOS_{(GR)}$-GR acquisitions with 20 and 80 spokes per partition. All PSFs were normalized to the peak of each individual PSF with peak amplitude set to 1. In the transversal view, there was significant PSF sidelobe energy for ASOS, but not for the

rest four strategies when 20 radial spokes are sampled. In the coronal view, there was significant energy in the PSF sidelobe for ASOS and RSOS$_{(Lin/GR)}$-Linear with 20 spokes, and these sidelobes were greatly reduced in the RSOS$_{(Lin/GR)}$-GR. In both transversal and coronal views, the PSFs corresponding to 80 radial spokes were similar among the five sampling methods and they were all similar to the full sampled PSF. Figure 6-2b and 6-2c shows the quantitative comparison of the five strategies in terms of incoherence measurement from PSF. The incoherence values (for both gridding and for compressed sensing reconstructions) for the RSOS$_{(Lin/GR)}$-GR strategies were superior (higher) to the ASOS and the RSOS$_{(Lin/GR)}$-Linear strategies regardless of the number of radial spokes per partition. This result confirms the superiority of the proposed GR rotation in the partition direction when compared to conventional aligned strategy or linear rotation, regardless of the in-plane radial angle arrangement.

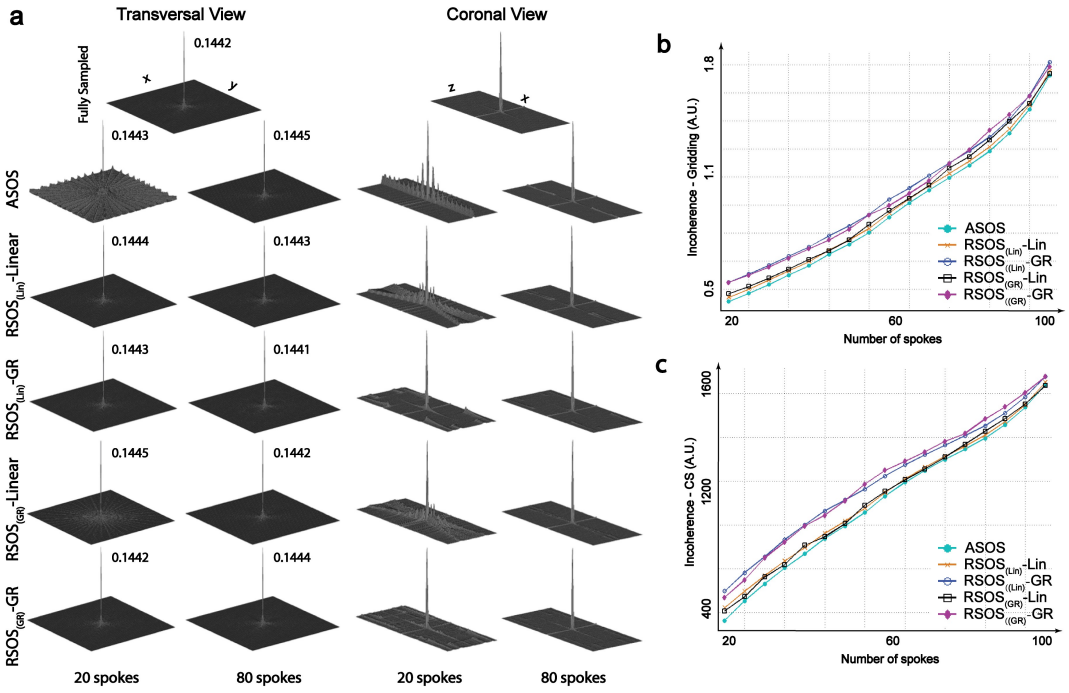

Figure 6-2 (a) The PSF of fully-sampled and ASOS, RSOS$_{(Lin)}$-Linear, RSOS$_{(Lin)}$-GR, RSOS$_{(GR)}$-Linear and RSOS$_{(GR)}$-GR k-space sampling with 20 spokes and 80 spokes per partition in

transversal and coronal views. All PSFs were normalized to the peak of each individual PSF such that all PSF peaks have unit amplitude. The individual normalization factors are noted at each peak in the transversal view. The PSFs are for the central slice of the volume in the respective view orientations. ASOS produces strong streaking artifact at when only 20 spokes are sampled per partition and there are essentially no significant difference between the five strategies when 80 spokes are sampled. For the 20 spokes per partition scenario, $RSOS_{(Lin/GR)}$-GR has reduce energy in the PSF sidelobes compared to ASOS and $RSOS_{(Lin/GR)}$-Linear in the coronal view. (b,c) The calculated incoherence indices for gridding reconstruction (b) and for CS-based reconstructions (c). $RSOS_{(Lin/GR)}$-GR has superior PSF incoherence compared with ASOS and $RSOS_{(Lin/GR)}$-Linear.

6.3.2 Phantom Experiment

Figure 6-3 shows two representative partitions of phantom images based on the five sampling strategies, as well as the fully sampled reference. With 20 spokes per partition, severe streaking artifacts (white arrows) and blurring of edge structures (blue arrows) were evident on the images acquired with ASOS and $RSOS_{(Lin/GR)}$-Linear; the image acquired with $RSOS_{(Lin/GR)}$-GR had much reduced artifacts and improved edge delineation. For 40 spokes per partition, streaking artifacts and blurring (yellow arrows) were reduced but were still significant in the ASOS and $RSOS_{(Lin/GR)}$-Linear images and the $RSOS_{(Lin/GR)}$-GR image were very similar to the fully sampled reference. With 80 views per partition, all five strategies provided high quality images. Table 6-2 in the online supporting materials shows the comparative results of the nRMSE and SSIM between the five sampling strategies and the three under-sampling factors. With 20 spokes per partition, the nRMSE and SSIM were 0.788/0.412 for ASOS, 0.702/0.501 for $RSOS_{(Lin)}$-Linear, 0.538/0.633 for $RSOS_{(Lin)}$-GR, 0.711/0.494 for $RSOS_{(GR)}$-Linear and 0.541/0.628 for $RSOS_{(GR)}$-GR. Overall, the nRMSE and SSIM for $RSOS_{(Lin/GR)}$-GR were both better than $RSOS_{(Lin/GR)}$-Linear or ASOS for all the under-sampling factors compared, while $RSOS_{(Lin)}$-GR and $RSOS_{(GR)}$-GR had similar performance (also true for $RSOS_{(Lin)}$-Linear and $RSOS_{(GR)}$-Linear).

Table 6-2 Qualitative comparisons of the five sampling strategies and the three under-sampling factors in the phantom imaging experiment. nRMSE: normalized root mean square error; SSIM: structural similarity index

	nRMSE	SSIM
ASOS: 20 spokes	0.788	0.412
$RSOS_{(Lin)}$-Linear:20 spokes	0.702	0.501
$RSOS_{(Lin)}$-GR: 20 spokes	0.538	0.633
$RSOS_{(GR)}$-Linear:20 spokes	0.711	0.494
$RSOS_{(GR)}$-GR: 20 spokes	0.541	0.628
ASOS: 40 spokes	0.391	0.728
$RSOS_{(Lin)}$-Linear:40 spokes	0.352	0.792
$RSOS_{(Lin)}$-GR: 40 spokes	0.298	0.835
$RSOS_{(GR)}$-Linear:40 spokes	0.346	0.781
$RSOS_{(GR)}$-GR: 40 spokes	0.291	0.833
ASOS: 80 spokes	0.181	0.938
$RSOS_{(Lin)}$-Linear:80 spokes	0.173	0.943
$RSOS_{(Lin)}$-GR: 80 spokes	0.162	0.951
$RSOS_{(GR)}$-Linear:80 spokes	0.169	0.948
$RSOS_{(GR)}$-GR: 80 spokes	0.161	0.957

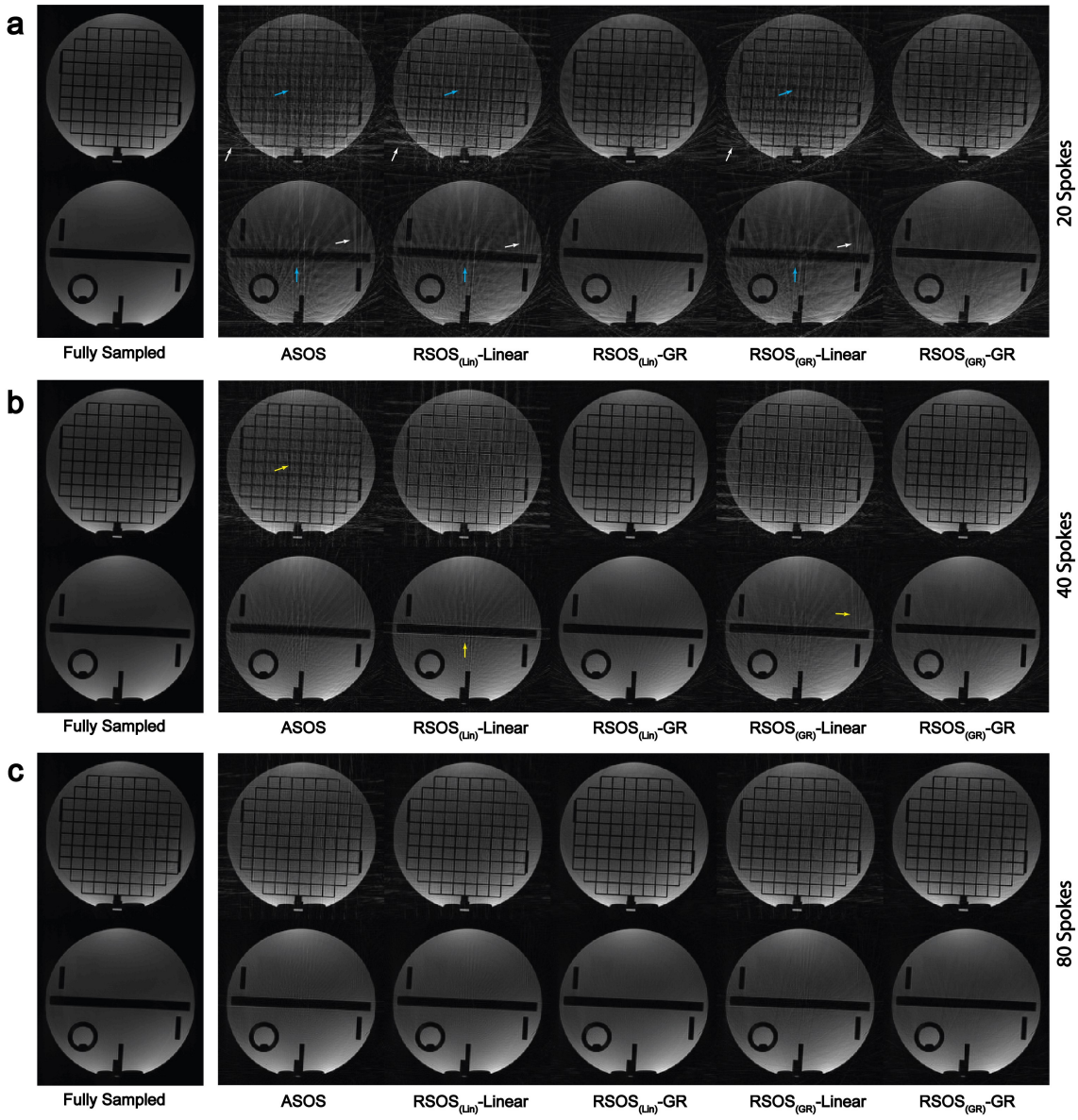

Figure 6-3 Phantom images acquired with different sampling strategies and with 20, 40 and 80 spokes per partition. From left to right, each column in (a), (b) and (c) shows two representative axial slices from the 3D images acquired with: fully-sampled, ASOS, $RSOS_{(Lin)}$-Linear, $RSOS_{(Lin)}$-GR, $RSOS_{(GR)}$-Linear, and $RSOS_{(GR)}$-GR, respectively. Three under-sampling scenarios are shown: 20 spokes (a), 40 spokes (b) and 80 spokes per partition (c). Streaking artifacts (white arrows) and blurring of edges (blue arrows) are clearly visible on ASOS and $RSOS_{(Lin/GR)}$-Linear acquisitions when 20 spokes/partition was used. By doubling the spoke number (e.g. 40 spokes), residual streaking and blurring (yellow arrows) still exist.

6.3.3 *In-vivo* Experiment

Figure 6-4 shows representative brain images acquired using the five sampling strategies. Similar to phantom experiment, the level of streaking artifacts (white arrows)

and blurring of fine structures (zoom-in boxes) were greater when using ASOS or $RSOS_{(Lin/GR)}$-Linear, especially at higher under-sampling factors (Figure 6-4a); in comparison, images acquired with $RSOS_{(Lin/GR)}$-GR had reduced artifacts and improved delineation of small features. Difference between the three strategies diminished as the number of spokes per partition increased from 40 to 80 (Figure 6-4b). As shown in Table 6-3 in the online support materials, the nRMSE and SSIM for $RSOS_{(Lin/GR)}$-GR of in vivo brain imaging data were better than $RSOS_{(Lin/GR)}$-Linear and ASOS, similar to our phantom results. With 40 spokes per partition, the nRMSE and SSIM were 0.521/0.632 for ASOS, 0.494/0.663 for $RSOS_{(Lin)}$-Linear , 0.352/0.704 for $RSOS_{(Lin)}$-GR, 0.502/0.655 for $RSOS_{(GR)}$-Linear and 0.361/0.695 for $RSOS_{(GR)}$-GR.

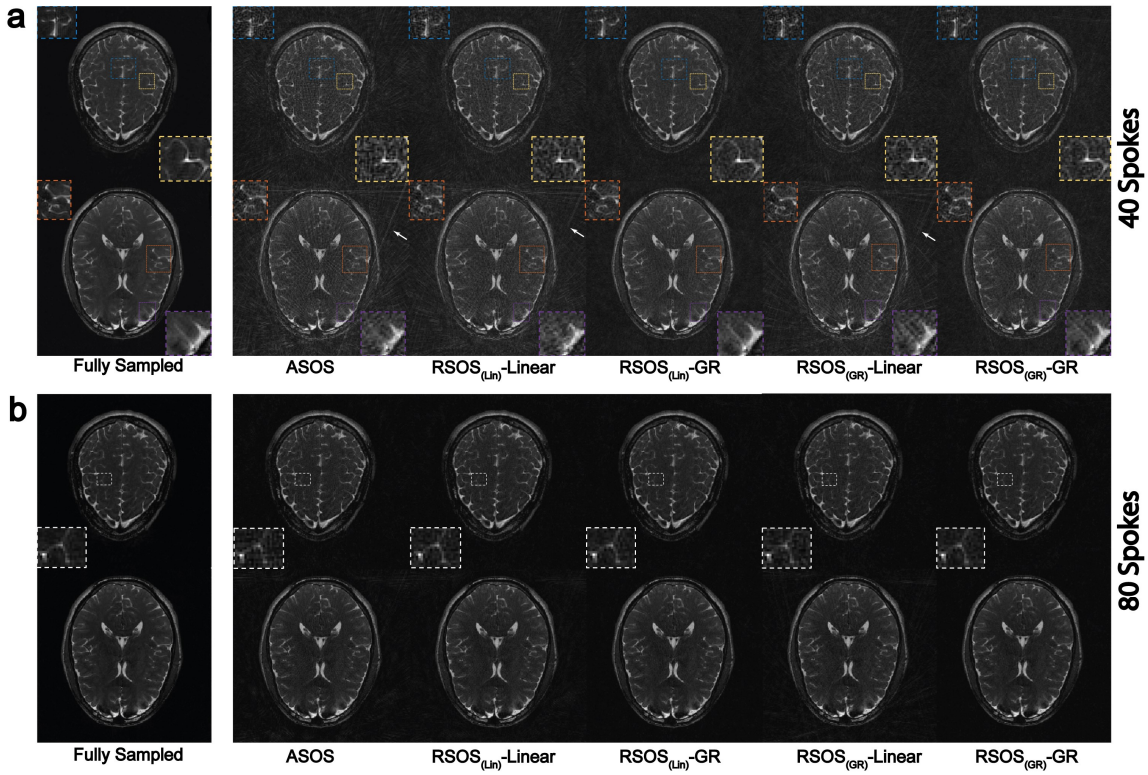

Figure 6-4 Selected brain images acquired with different sampling strategies and number of spokes per partition. Each column in (a) and (b) shows two representative axial slices from the 3D images acquired with: fully-sampled, ASOS, $RSOS_{(Lin)}$-Linear, $RSOS_{(Lin)}$-GR, $RSOS_{(GR)}$-Linear, and $RSOS_{(GR)}$-GR, respectively. Two under-sampling scenarios are shown: 40 spokes per partition (a) and 80 spokes per partition (b). Zoom-in boxes provide detailed comparisons of the five acquisition

strategies on fine structures. White arrows highlight the streaking artifact on ASOS and $RSOS_{(Lin/GR)}$-Linear acquisitions.

Table 6-3 Qualitative comparisons of the five sampling strategies and the two under-sampling factors in the brain imaging experiment. nRMSE: normalized root mean square error; SSIM: structural similarity index

	nRMSE	SSIM
ASOS: 40 spokes	0.521	0.632
$RSOS_{(Lin)}$-Linear:40 spokes	0.494	0.663
$RSOS_{(Lin)}$-GR: 40 spokes	0.352	0.704
$RSOS_{(GR)}$-Linear:40 spokes	0.502	0.655
$RSOS_{(GR)}$-GR: 40 spokes	0.361	0.695
ASOS: 80 spokes	0.223	0.796
$RSOS_{(Lin)}$-Linear:80 spokes	0.205	0.812
$RSOS_{(Lin)}$-GR: 80 spokes	0.191	0.837
$RSOS_{(GR)}$-Linear:80 spokes	0.197	0.821
$RSOS_{(GR)}$-GR: 80 spokes	0.188	0.842

Figure 6-5a shows two partitions of reconstructed abdominal images acquired with the five sampling strategies. On both partitions, streaking artifact in the body organs and outside of the body (yellow arrows) and blurring of edges (orange arrows) can be seen on the image with ASOS and $RSOS_{(Lin/GR)}$-Linear acquisitions. With $RSOS_{(Lin/GR)}$-GR, the streaking artifacts were greatly reduced and the edges appeared sharper. Figure 5b shows the dMRA-ASL maximum-intensity projection (MIP) images reconstructed with 3D gridding and PI-CS methods at two phases using ASOS and $RSOS_{(Lin)}$-GR. Distinct differences can be appreciated between the two acquisition strategies on gridding reconstruction, where strong streaking artifacts appear on the image with ASOS acquisition, but are mostly reduced in the $RSOS_{(Lin)}$-GR acquisition. With a PI-CS

reconstruction, residual streaking artifacts (blue arrows) can still be clearly seen. On the contrary, RSOS$_{(Lin)}$-GR with PI-CS provided much improved image quality. The example in Figure 6-5b shows the benefit of RSOS$_{(Lin)}$-GR in SNR-limited applications such as ASL.

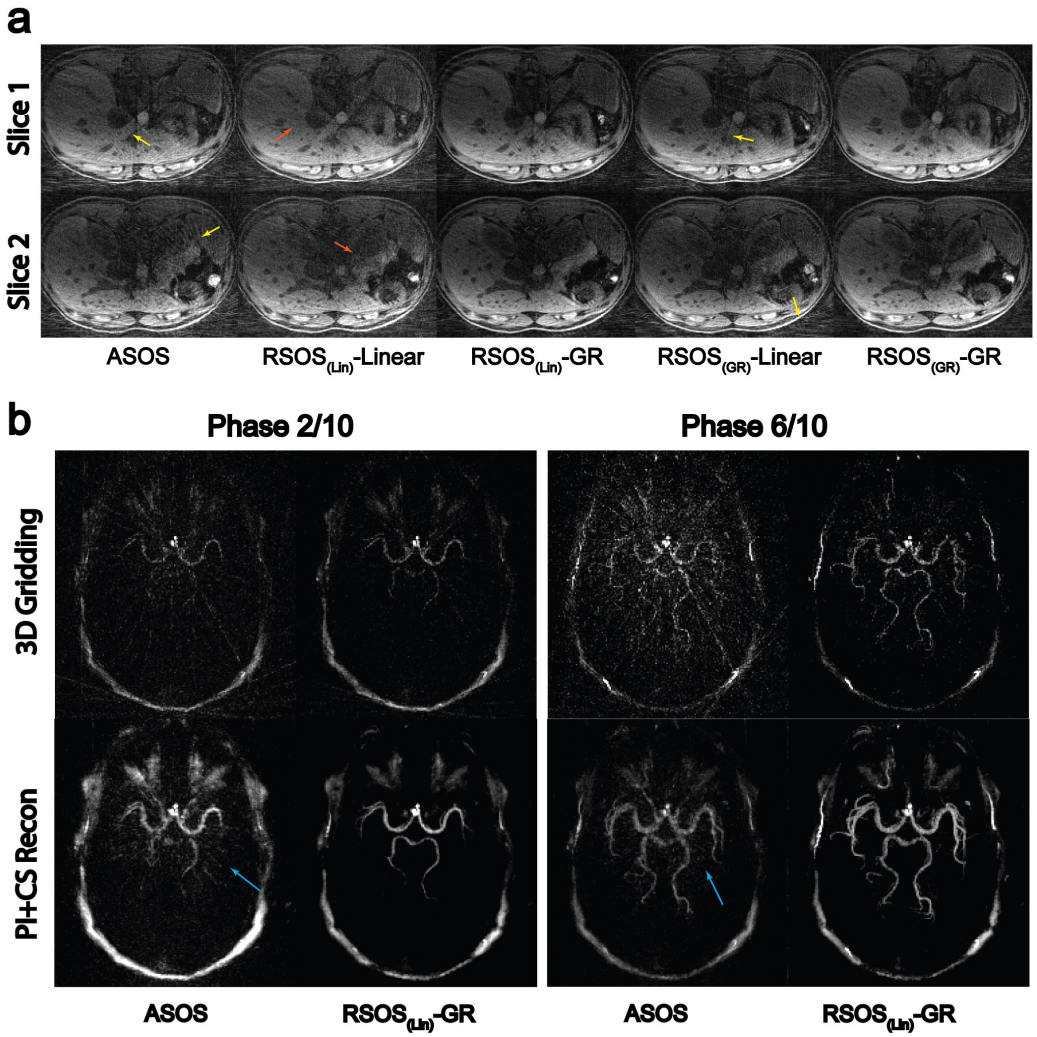

Figure 6-5 (a) Two representative slices of abdominal images acquired with ASOS, RSOS$_{(Lin)}$-Linear, RSOS$_{(Lin)}$-GR, RSOS$_{(GR)}$-Linear, and RSOS$_{(GR)}$-GR. RSOS$_{(Lin/GR)}$-GR provides images with less streaking artifacts and sharper structures. (b) MIP images at two phases of dMRA-ASL images acquired with ASOS and RSOS$_{(Lin)}$-GR. Even with only 20 spokes per partition per phase, RSOS$_{(Lin)}$-GR is still able to reduce majority of streaking artifacts compared with ASOS using 3D gridding reconstruction. With a PI-CS reconstruction, overall image quality was improved for both acquisitions. However, blurring of vessels and residual streaking artifacts can still be seen on

images with ASOS acquisition while $RSOS_{(Lin)}$-GR acquisition provides cleaner and sharper images.

6.4 Discussion

This work presented a golden ratio rotated stack-of-stars sampling strategy for improved 3D (or dynamic 3D) imaging. Our results show that, by rotating radial spokes along the through-plane direction in a golden-ratio manner, streaking artifacts arising from under-sampling are less structured and much reduced compared with the conventional aligned acquisition strategy or the rotated stack-of-stars with a linear angle rotation in the partition direction. Compared with the previously proposed linear rotation strategy (111,124), rotation in a golden-angle manner along the partition encoding direction provides more uniform local 3D k-space sampling. Since 3D gridding is a local operation that uses a support-limited kernel to interpolate the sampled data points onto a Cartesian grid, more locally uniform 3D k-space sampling leads to better gridding reconstruction results. Our results further show that our GR rotation approach provides improved image reconstruction regardless of the in-plane radial view order of either linear or golden angle. Another choice for radial sampling of the 3D k-space is 3D Koosh-Ball (117,118), which offers variable density sampling in 3D. However, for imaging applications that have non-isotropic FOV, such as abdominal and thoracic imaging, 3D Koosh-Ball is less commonly used since it typically requires similar FOV in all three orthogonal directions.

A drawback of the proposed method is its reconstruction speed and computation demand. Instead of performing highly parallelizable partition-by-partition 2D reconstructions after an initial Fourier transform along the partition encoding direction, a strategy widely used in ASOS acquisition to reduce computation demand and improve reconstruction speed, RSOS requires 3D volumetric reconstruction to better take advantage

of the incoherent 3D k-sampling provided by spoke rotation in the through-plane direction. Such a 3D whole-volume reconstruction is computationally more expensive since 3D interpolation (gridding) needs to be performed rather than 2D gridding, which reduces reconstruction speed. However, significant gains in reconstruction speed may be obtained by using dedicated reconstruction libraries (51,127,128) for CPU/GPU. For example, it only takes 15s to reconstruct a 256*20*64*32 (readout points*spoke number*partition number*coil number) RSOS dataset with 3D gridding (5s to reconstruct a same size ASOS dataset with partition-by-partition 2D gridding) using BART.

In most of our imaging experiments, we only performed 3D gridding reconstruction on the highly under-sampled data. One will notice that even for RSOS-GR, reconstructed images still suffer from some residual streaking artifacts and noise amplification. With a PI-CS reconstruction, image quality would be greatly improved. For the parallel imaging part, there are several ways to acquire sensitivity maps without acquiring fully-sampled data if SENSE-type reconstruction is desired. One solution is using pre-scan that acquires a few additional calibration lines (102) that can not only be used to estimate sensitivity maps but also to correct system-dependent gradient-delays errors. Another solution is to use optimization-based strategies (129) to recover center region of k-space if k-space is highly under-sampled. Recovered center region can then be used to estimate maps. If GRAPPA-type instead of SENSE-type reconstruction is desired, self-calibration strategies such as GROG (130), SPIRiT (131) can be used to directly fill out the missing k-space points. For the compressed sensing part, different types of regularizations (72,102) can be applied to further remove artifacts and recover details. Since radial sampling provide intrinsic variable density sampling and incoherent artifacts when under-sampled, the

incorporation of additional regularizations/sparsifying transforms can potentially benefit the image reconstruction.

6.5 Conclusion

We have presented a golden ratio rotated stack-of-stars sampling strategy to efficiently sample 3D k-space. Image quality is significantly improved in phantom and in-vivo experiments comparing with the conventional aligned sampling strategy or stack-of-stars with linear angle rotation. This strategy is useful for 3D stack-of-stars radial imaging for various clinical applications.

Chapter 7 Low-Latency Fast Real-Time Imaging

In the previous four chapters, we introduced different optimization based reconstruction techniques to enable accelerated acquisition for two applications. Although great efforts have been made to keep the reconstruction time within reasonable range that fits the clinical workflow for each particular application, their non-linear online-optimization feature prevents them to reach similar reconstruction speed as linear based reconstruction. This is particularly problematic for applications such as real-time imaging, which will greatly benefits the low-latency image feedback for online decision making. In this chapter, we introduced a learning based reconstruction strategy and demonstrated its performance in accelerated real-time imaging application.

7.1 Introduction

With tremendous advances in MRI hardware performance and fast imaging techniques in the past two decades, real time MRI has shown great potentials for a number of challenging applications, such as speech imaging (132), cardiac imaging (133), functional imaging (134), and interventional MRI (135). To achieve sufficient frame rate, real time MRI typically requires significant k-space under-sampling to accelerate the data acquisition; hence advanced image reconstruction algorithms such as parallel imaging and/or compressed sensing (CS) are necessary to recover the image from under-sampled k-space. These image reconstruction methods can be categorized as either online or off-line methods. For those real-time MRI applications that require user interaction or real time decision making based on image feedback, such as interventional MRI, the images need to be reconstructed online with minimal latency, which is the time interval between the end

of data acquisition and the completion of image reconstruction. For applications that require fast data acquisition but not online image reconstruction, slower off-line methods may be used. For example, Uecker et al. (136) demonstrated 1.5mm^2 and 20ms spatial/temporal resolution real-time MRI using radial FLASH sequence and non-linear inversion reconstruction. However, their off-line image reconstruction algorithm requires 2.5s to reconstruct a single image frame of size 128*128 with GPU acceleration. In another online real time MRI study by Lingala et al. (137), the authors used a through time spiral GRAPPA method (138) for real-time speech imaging with a reconstruction latency per frame of 114ms and a modest spatial resolution of 2.4mm^2. More recently, with the help of increasing power of CPU/GPU, several online reconstruction approaches (139–141) were able to perform high spatial and temporal resolution real-time imaging, using non-Cartesian trajectories and CS based iterative algorithms.

Despite the promise of non-Cartesian trajectories and CS based iterative approaches in real-time imaging, these methods are limited in certain aspects: 1). Non-Cartesian trajectories are sensitive to different kinds of system imperfections and usually require extra pre/post-processing time for reconstruction (116); 2). Human designed fixed sparsifying transforms used in most CS based algorithms may be too simple to capture the underlying complex image features (31); 3). Solvers for iterative algorithm need to be specially designed or modified so that low-latency online reconstruction is feasible (141). Recent developments in deep learning-based MRI image reconstruction may provide solutions to these issues. Taking the experiences from early success in image classification (27) and recent improvement in image restoration (142) and super-resolution (143), several neural network architectures have been proposed (33,34,36,144) to learn the (non-linear)

mapping from artifact-contaminated images due to k-space under-sampling to the fully-sampled reference images. This could greatly relax the need for using non-Cartesian k-space trajectories to achieve incoherent sampling, and alleviate the need for optimizing the sparsifying transform. More importantly, the burden of learning such a mapping (characterized by network parameters) is offloaded to the off-line training process. Once the mapping is learned, applying the trained network to newly acquired under-sampled data can typically be completed with minimal latency (within tens to hundreds of milliseconds).

In this work, we sought to develop a Parallel Imaging and Convolutional Neural Network (PI-CNN) combined reconstruction framework and apply it to 2D real-time imaging for low-latency online reconstruction. Compared with most existing neural network-based methods (33,35,144) that only learn the mapping from single-coil data, our framework integrated multi-coil k-space data and utilize them through parallel imaging. We demonstrate the capability of our framework on two different applications: real-time cardiac imaging at 1.5T and real-time abdominal imaging at 0.35T. Retrospective studies were performed to compare the proposed method against an existing single-coil based neural network reconstruction (144) and a PI-CS method (50). Prospective examples were also shown to demonstrate the improved temporal resolution from the accelerated acquisition and our image PI-CNN reconstruction algorithm.

7.2 Methods

7.2.1 Problem Formulation

To reconstruct under-sampled data in an accelerated MR acquisition, an ill-posed linear inverse problem can be formulated as follows:

$$A_u x = y \tag{7-1}$$

where x is the target image to be reconstructed; y is the acquired multi-coil under-sampled k-space data padded with zeros at un-sampled k-space locations; and A_u is a chain of linear operators including point-wise multiplication of sensitivity maps, forward Fourier transform, and point-wise multiplication of under-sampling mask. Since the system of Equation 7-1 is ill-posed, as well as the fact that measured data y are noisy in practical scenarios, minimizing the least square error of Equation 7-1 with additional regularization term $R(x)$ is usually used to prevent over-fitting to noisy image, given by the following optimization problem:

$$min_x \, ||A_u x - y||_2^2 + \lambda R(x) \tag{7-2}$$

where λ is the regularization parameter that trades-off the data fidelity term and regularization term.

Common choices of $R(x)$ are l_1 norm of wavelets and total variation, aiming at exploiting the sparsity of the underlying image in the transform domain. However, pre-determined sparsifying transforms only preserve certain features of the image and lack the generality of representing complex natural features. For example, total variation reflects sparsity at edges of the image and therefore favors piece-wise constant structures. An inappropriate use of total variation can cause over-smoothing and blocky artifacts on the reconstructed image. Inspired by early work of using sparse dictionary learning based regularization (31) for MR reconstruction, and more recent work of using convolutional neural networks (CNN) for natural image reconstruction (145), we propose to use a general CNN-based regularization in this work. Specifically, assume $M_{CNN}: x_{artifact} \rightarrow x_{clean}$

maps an artifact-contaminated image to an artifact-free image. It can be represented by multiple layers of convolutional kernels parameterized by θ (145,146). Hence, a compact representation of this mapping is:

$$M_{CNN}(x_{artifact}|\theta) = x_{clean} \quad (7\text{-}3)$$

Incorporating Equation 7-3 as a regularization term into Equation 7-2 gives us the following reconstruction problem:

$$min_x \, ||A_u x - y||_2^2 + \lambda||x - M_{CNN}(x_{zf}|\theta)||_2^2 \quad (7\text{-}4)$$

where x_{zf} is the image derived from under-sampled zero-filled k-space data. In case the mapping $M_{CNN}(x_{zf}|\theta)$ is already learned with known parameters θ^*, Equation 7-4 can be solved using the gradient descent algorithm with some initial image x^0:

$$x^{t+1} = x^t - 2\alpha^t[\lambda(x^t - M_{CNN}(x_{zf}|\theta^*)) + A_u^*(A_u x^t - y)] \quad (7\text{-}5)$$

where x^t is reconstructed image at iteration t, α^t is the step size at iteration t, and A_u^* is the adjoint chain of linear operators. For previously mentioned natural image reconstruction task (145,146), learning parameters θ for M_{CNN} is usually performed in image domain only. However, by incorporating the k-space data in training, which is a representation of the image in the spatial-frequency domain, we hypothesize that we will be able to improve image reconstructions compared to traditional image based training. In several previously proposed CNN-based MR reconstruction methods (144,147) that utilized k-space data for reconstruction, the investigators either utilized the k-space data after the network training is completed (147) or only considered single-coil data (144). On the contrary, the proposed approach alternatively learns parameters θ through CNN and

solves the parallel imaging problem in Equation 7-5, using a cascaded network architecture (144) as shown in Figure 1. Our approach not only generalizes the common regularization terms used in CS methods, but also allow the CNN to better use the acquired multi-coil k-space data by incorporating parallel imaging.

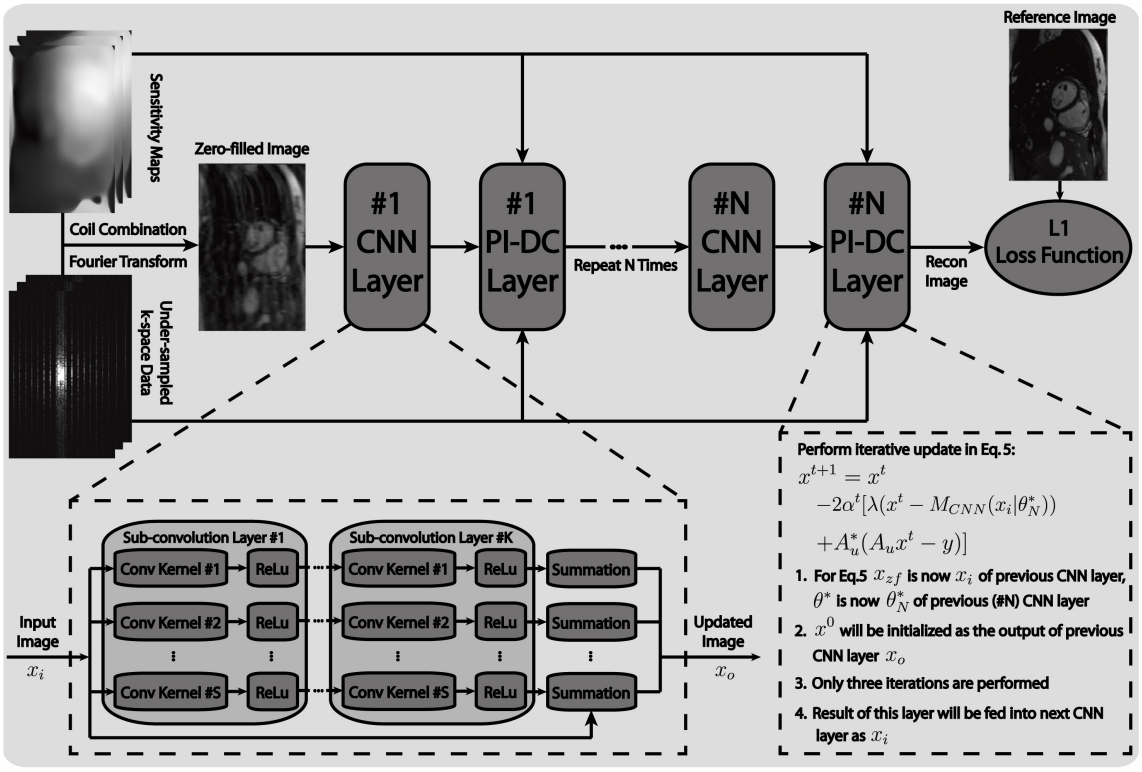

Figure 7-1 Structure of the proposed parallel imaging and convolutional neural network (PI-CNN) combined reconstruction network. The PI-CNN network consists of *N* composite CNN layers and PI-DC layers cascaded in series. Each composite CNN layer contains *K* sub-convolution layers. To obtain a reconstruction, we provide the sensitivity maps, under-sampled k-space data, and initial zero-filled image to the network, and let them pass through the network layers. During the off-line training process, the reconstructed image is compared with an artifact-free reference image using the L1 similarity measure, and resulting reconstruction error is propagated backward to derive the updated set of parameters for the network layers.

7.2.2 Network Design

As illustrated in Figure 7-1, our network consists of *N* composite CNN layers and *N* Parallel Imaging data consistency (PI-DC) layers cascaded in series. Each composite CNN layer contains an input layer, *K* sub-convolution layers associated with rectifier linear units

(ReLu) as activation function, a summation layer that sums the output of sub-convolution layers with input layer, and an output layer. Each sub-convolution layer has $S = 48$ filters with size 3*3. Input layers of the composite CNN layers have two channels, one for the real part and one for the imaginary part of complex image. In the output layer, the two-channeled image is combined together as a single-channeled complex image, which subsequently serves as input to the following PI-DC layer. In the PI-DC layer, the output of the preceding composite CNN layer is iteratively updated according to Equation 7-5. Due to the concern of computation time, three iterations are performed in the PI-DC layer, and the result is the input to the subsequent composite CNN layer. λ was set to 0.4 empirically in Equation 7-5.

During the offline network training process, the goal is to find an optimal parameter set θ for the convolution filters. Since there is no updatable parameter in the PI-DC layer, a total of $N * K * 3 * 3 * 48 * 2$ parameters need to be trained. To set up this procedure, we minimize a loss function over a set of paired reconstructed image and reference image with respect to θ. Based on previous literature (148), we choose L1 norm instead of conventional L2 norm as our main loss function, which is defined as follows:

$$L(\theta) = min_{\theta} \sum_{i=1}^{P} ||Mag(x_{recon}^{i}(\theta)) - Mag(x_{ref}^{i})||_1 + \gamma||\theta||_2 \qquad (7\text{-}6)$$

where x_{recon}^{i} and x_{ref}^{i} is the i^{th} pair of images in the set of size P, and $Mag(\cdot)$ is the operation that takes the magnitude of the complex image. To prevent model over-fitting, we further added an L2 regularization on the network parameters. Due to the fact that $Mag(\cdot) = \sqrt{real(\cdot)^2 + imag(\cdot)^2}$ is not differentiable at the origin point, we relaxed it with $Mag_{\epsilon}(\cdot) = \sqrt{real(\cdot)^2 + imag(\cdot)^2 + \epsilon}$ in our practical implementation. The above

optimization problem is solved by the well-known back-propagation algorithm (149), i.e. applying the chain rule for parameters θ_m of the m^{th} layer:

$$\frac{\partial L(\theta)}{\partial \theta_m} = \frac{\partial x_{recon}^{[m+1]}}{\partial \theta_m} \cdot \frac{\partial x_{recon}^{[m+2]}}{\partial x_{recon}^{[m+1]}} \cdots \frac{\partial x_{recon}^{[N \cdot K+N]}}{\partial x_{recon}^{[N \cdot K+N-1]}} \cdot \frac{\partial L(\theta)}{\partial x_{recon}^{[N \cdot K+N]}}$$

where $x_{recon}^{[m+1]}$ is the output of $(m+1)^{th}$ layer from a total of $N \cdot K + N$ layers including the sub-convolution layers and PI-DC layers. Note that we are performing an end-to-end training, and therefore, the back-propagation starts from the last cascaded layer. Although no parameter is updated in the PI-DC layer, the derivation of its output with respect to its input still needs to be calculated, so that the gradient can flow backward.

For comparison purposes, the single-coil based network described in Ref. (144) was also implemented in this work. In this network, the k-space data y in Equation 7-4 is replaced with a synthesized single-coil k-space data, which is generated by inverse Fourier transform of fully-sampled multi-coil k-space data to image domain, coil-combination in image domain using SENSE (3), another Fourier transform, and retrospective k-space under-sampling. The chain operator A only involves performing Fourier transform and applying the under-sampling mask. Moreover, Equation 7-5 is replaced with a single-step k-space data substitution operation. Equation (6) in Ref. (144) describes this operation in more details.

7.2.3 Data Acquisition

To evaluate the performance of the proposed PI-CNN method and demonstrate its utility, we tested our strategy for real time cardiac and abdominal imaging applications. The study was approved by our institutional review board, and each subject provided written informed consent. For cardiac imaging, 20 healthy volunteers were scanned on a

1.5T MRI scanner (Avanto Fit, Siemens Medical Solutions, Erlangen, Germany) using a standard bSSFP sequence with a 32-channel body coil array (TE/TR = 1.5/3ms, flip angle = 60^{o}, bandwidth = 814Hz/pixel, field of view = 260-350*160-220mm^2, matrix size = 192*122, slice thickness = $6mm^2$). In each volunteer, 250 short-axis view fully sampled images (temporal resolution = 3 frames per second) at various slice locations across the heart were acquired during free-breathing without ECG gating. Prospectively 4X under-sampled data using a one-dimensional variable density Poisson-disc pattern (5) were acquired in two additional volunteers in the short-axis view. As a comparison, a separate cardiac cine MRI using conventional 3X GRAPPA acceleration with 20 reference lines and partial Fourier 5/8, corresponding to a 4X net acceleration, was acquired at the same slice locations as our Poisson-disc under-sampled data.

For abdominal imaging, a total of 7 healthy volunteers and 7 liver cancer patients were scanned on a 0.35T MRI-guided radiotherapy (MRgRT) system (MRIdian, ViewRay, Cleveland, OH) using a standard bSSFP sequence with a 12-channle body coil array (TE/TR = 1.7/3.4ms, flip angle = 110^{o}, bandwidth = 548Hz/pixel, field of view = 300-420*180-250mm^2, matrix size = 192*114, slice thickness = $8mm^2$). The MRgRT system is capable of simultaneous MRI and radiotherapy, but was only used as an MRI scanner in the study. In each volunteer and patient, 250 sagittal fully sampled images (temporal resolution = 3 fps) at various locations of the liver region (covering the tumor for patients) were acquired during free-breathing.

7.2.4 Network Training

Both the proposed network and the single-coil based network described in Ref. (144) were trained using retrospectively under-sampled data paired with their corresponding

fully-sampled reference data. As mentioned above, SENSE reconstruction (3) was used to generate single-coil images from multi-coil images in the single-coil based network (144). In the proposed network, SENSE type reconstruction was used in the PI-DC layer to enforce data consistency under the parallel imaging framework. For cardiac imaging, 3000 short-axis image pairs from the first 12 volunteers were used for training. For abdominal imaging, 2500 sagittal image pairs from 5 volunteers and 5 patients were used. For a given under-sampling factor (3X-5X), the Poisson-disc under-sampling masks were varied for the training data sets so that the network learns various aliasing patterns. The coil sensitivity maps used in the proposed method were calibrated from the 24*24 central k-space region using ESPIRiT (50).

Both networks were implemented in Python using Theano and Lasagne libraries. Parameters of the networks were initialized with He initialization (150), trained with Adam optimizer (151) using following parameters: $\alpha = 1e^{-4}$, $\beta_1 = 0.9$, and $\beta_2 = 0.999$. 1000 epochs with minibatch size of 16 was used. All training and experiments were performed on a Linux PC (8 Core/4GHz, 64 GB, Nvidia GTX 760). It took approximately 1 day to train each network.

7.2.5 Evaluation

The proposed PI-CNN network was tested on data from the remaining 8 volunteers in cardiac imaging, and the remaining 2 volunteers and 2 patients in abdominal imaging. All test data were not included in the training process.

In the first step, we evaluated the effect of different N and K in the proposed PI-CNN network. Two experiments were performed: 1). We fixed $K = 4$ for each composite CNN layer but varied $N = 1\sim6$. This experiment would show the value of increasing cascade

iteration. 2). We compared two architectures, both with 25 total number of layers : $N = 5, K = 4$ and $N = 1, K = 24$. The first architecture benefits from the repeated enforcement of data consistency while the second one can extract very deep features. This experiment allowed us to evaluate the benefit of using k-space data within a network. For each network trained in the two experiments, acceleration factor was set to 4-fold.

Next, we evaluated the performance of the proposed network against single-coil based network (144) and L1-ESPIRiT (50), a state-of-the-art PI-CS reconstruction method, through a retrospective study on the cardiac imaging. Based on experiments in the first step, we set $N = 5, K = 4$ for both the proposed network and the single-coil based network. Acceleration factors from 3-fold to 5-fold were evaluated with the 1D variable density Poisson-disc under-sampling pattern. L1-ESPIRiT was performed using a previously described tool (Berkeley Advanced Reconstruction Toolbox, BART) (51), with the same sensitivity maps used for network reconstruction. All hyper-parameters for L1-ESPIRiT such as the number of iterations and regularization parameters were tuned empirically to provide best image quality based on visual assessment.

Since our network learns to de-alias under-sampled artifact-contaminated images in general, it is possible that the network trained at one acceleration factor may be used to reconstruct images acquired with a different acceleration factor. To explore this, we used the network trained with the intermediate 4-fold acceleration factor in the previous experiment to reconstruct images retrospectively under-sampled with 3-fold to 5-fold. As a comparison, these images were also reconstructed using the networks trained with the corresponding acceleration factors. L1-ESPIRiT, as a representative of non-training-based methods, was also performed.

As a next step, we further evaluated the performance of the proposed PI-CNN network on the prospectively under-sampled data. However, it is not possible to reconstruct them with the single-coil based network (144). This is because it only works with the synthesized single-coil data (i.e., it is trained on the synthesized coil-combined image and coil-combined retrospectively under-sampled k-space data), while the acquired prospective under-sampled k-space data has multiple channels and there is no easy way to derive coil-combined under-sampled k-space data from that. Therefore, we only compare it with the L1-ESPIRiT reconstruction based on the same data, as well as the additionally acquired GRAPPA accelerated data.

Finally, to evaluate the proposed network in a different body site, a different SNR scenario, and to demonstrate its potential in clinical utility in patients, we performed a study for abdominal imaging acquired at 0.35T. The patients in this evaluation were liver cancer patients who underwent MR-guided radiation therapy using our MRgRT system. The abdominal images were acquired immediately after the patient finished a treatment session. The k-space data from one volunteer and two patients were retrospectively under-sampled by 3-fold, and reconstructed with the proposed network and L1-ESPIRiT. Because of the improved performance of proposed network over single-coil based network based on cardiac imaging (shown in the "Results" section), here we used the clinically available linear PI reconstruction GRAPPA as the alternative comparison, based on the same data that were retrospectively under-sampled with a regular pattern and net acceleration factor of 3-fold.

7.2.6 Data Analysis

To compare the different reconstruction strategies quantitatively in the second and last retrospective evaluations above, both normalized root mean square errors (nRMSE) and structural similarity index (SSIM) (56) were calculated between each frame of the reference images and images reconstructed with the different strategies (proposed network, single-coil based network, L1-ESPIRiT, and GRAPPA). The calculated nRMSE and SSIM were averaged across all frames and all volunteers/patients. Whereas reduction in nRMSE indicates greater fidelity to the original image, an SSIM value of 1 indicates perfectly identical pair and the SSIM value decreases as the images differ.

7.3 Results

Figure 7-2 shows example images reconstructed from the six networks that have different cascading depths ($N = 1{\sim}6$). As N increased, the reconstructed images had less aliasing artifacts (red arrows), sharper tissue boundary (yellow arrows) and better delineated myocardium (green arrows). The rate of improvement and artifact reduction slowed down as N increased. There was obvious difference between the $(N = 1, K = 4)$ image and the $(N = 2, K = 4)$ image. The difference between the $(N = 5, K = 4)$ image and the $(N = 6, K = 4)$ image was more subtle, although the the $(N = 6, K = 4)$ image required increased reconstruction time (46ms for $N = 5$ and 90ms for $N = 6$ to reconstruct a 12-channel data) and potentially increased sensitivity to over-fitting. Therefore, we used the $N = 5, K = 4$ network for the remaining study of this work.

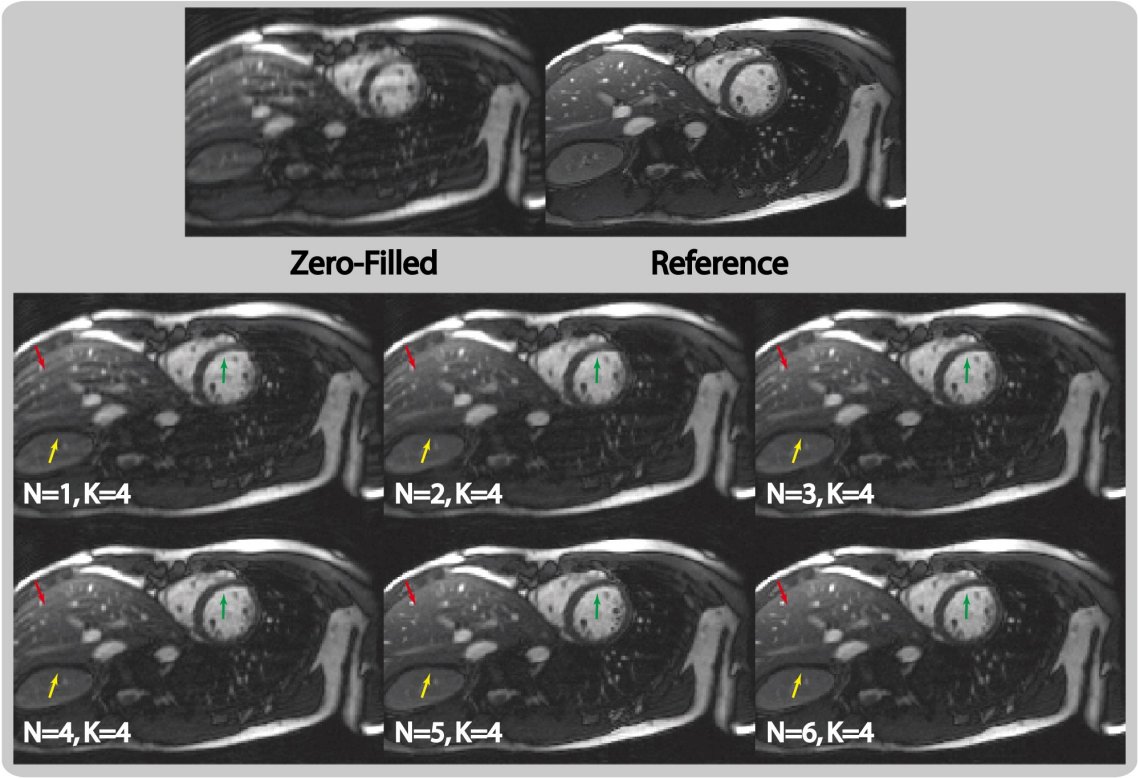

Figure 7-2 Example images reconstructed with the proposed PI-CNN network using different network depths (i.e. number of composite CNN and PI-DC layers) at 4-fold acceleration factor. With increased depth (N from 1 to 6), the reconstructed image has less aliasing artifact (red arrows) and sharper edges (yellow and green arrows), although this comes with longer reconstruction time. The network with $N = 5, K = 4$ represents a good balance between image quality and required reconstruction time.

Figure 7-3 shows the comparison of the two network architectures that have the same total number of 25 layers on selected reconstructed frames. As illustrated, the architecture that employs very deep convolution layers ($N = 1, K = 24$) for feature extraction was not able to remove residual aliasing artifacts (blue arrows) and failed to recover sharp myocardium boundaries (red arrows). This is probably due to the training over-fitting since the size of training data is relatively small compared with the number of parameters within the directly connected network. On the contrary, using the same size of training data, the interleaved architecture ($N = 5, K = 4$) reconstructed much cleaner and sharper images, benefitting from the fact that it consistently provides updated improved image from a PI

reconstruction for each composite CNN layer. This consequently allows the network to converge faster and generalize better for new unseen images.

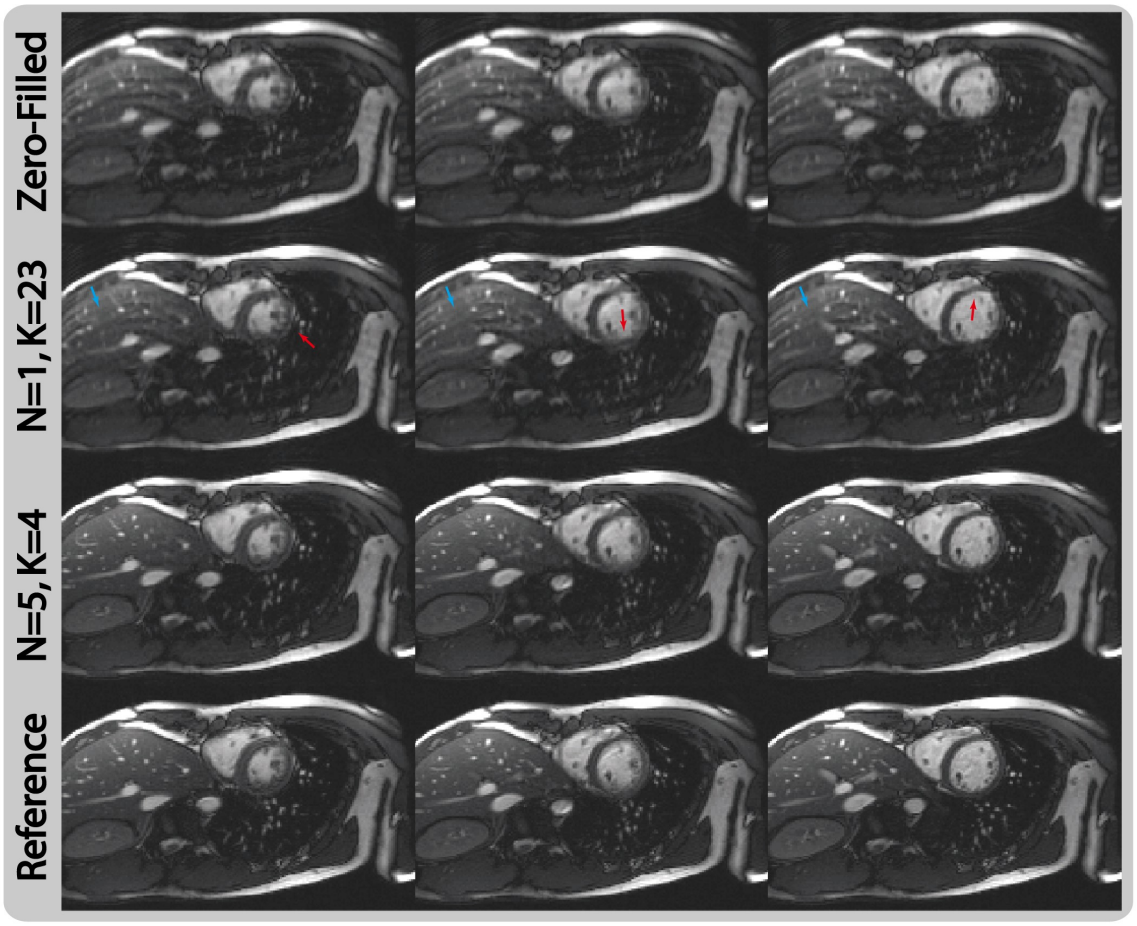

Figure 7-3 Selected reconstructed images of retrospective 4-fold acceleration at three cardiac phases from two networks that have the same number of total layers but different architectures. For the network that has very deep convolution layers ($N = 1, K = 24$), it fails to remove residual aliasing artifacts and sharpen the edges. On the other hand, the proposed cascaded architecture ($N = 5, K = 4$) allows good utilization of the feature extraction from CNN layers and data consistency enforcement from PI-DC layers, and produces cleaner and sharper reconstructions.

To better understand how the proposed network utilizes the interleaving CNN and PI-DC structure, Figure 7-4 shows the intermediate images from each of the composite CNN layers (top row) and PI-DC layers (bottom row) within the proposed network. In general, the cascaded structure gradually removes the aliasing artifacts and sharpens the images. Since end-to-end training was used, the intermediate layers can internally learn to correct

for the errors caused by the previous layers, and thus make the reconstructed image from the last layer optimally similar to the reference image in terms of the error metric chosen. At the same time, by inserting a PI-DC layer between composite CNN layers, image quality can be improved due to the incorporated multi-coil information. This can be clearly visualized at each PI-DC layer in the bottom row.

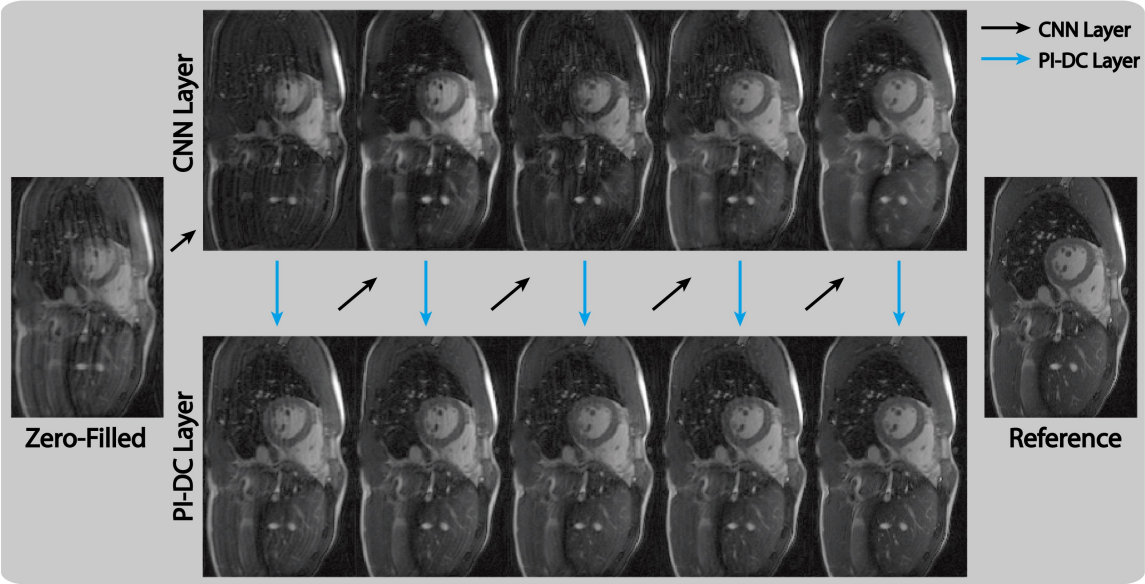

Figure 7-4 Intermediate network layer outputs of the PI-CNN network for a retrospectively 4-fold under-sampled data. We observe overall continuously suppression of aliasing artifacts and sharpening of fine structures as the data pass through each cascaded layer. Due to the end-to-end training, our proposed PI-CNN network can internally correct for these deviations and produce an artifact-free image after the final layer.

Figure 7-5 shows representative images reconstructed from zero-filling, single-coil based network, proposed network, L1-ESPIRiT, and fully-sampled reference data. With 3-fold under-sampling, all three strategies (single-coil based network, the PI-CNN network, and L1-ESPIRiT) were able to reconstruct images with acceptable quality, although reconstruction from single-coil based network had mild blurring on fine structures. With 4-fold under-sampling, single-coil based network reconstructed an image with apparent residual aliasing artifact (white arrow) and over-smoothed blocky artifacts (yellow arrow).

L1-ESPIRiT similarly had blurred myocardium (red arrow) and small blood vessel (blue arrow). The proposed network, however, could reconstruct similar image compared with the reference. At 5-fold acceleration, the proposed PI-CNN method started to show over-smoothed images (green arrows). The other two methods had similar reconstruction errors with 4-fold under-sampling. These observations correlate well with the numerical analysis shown in Table 7-1.

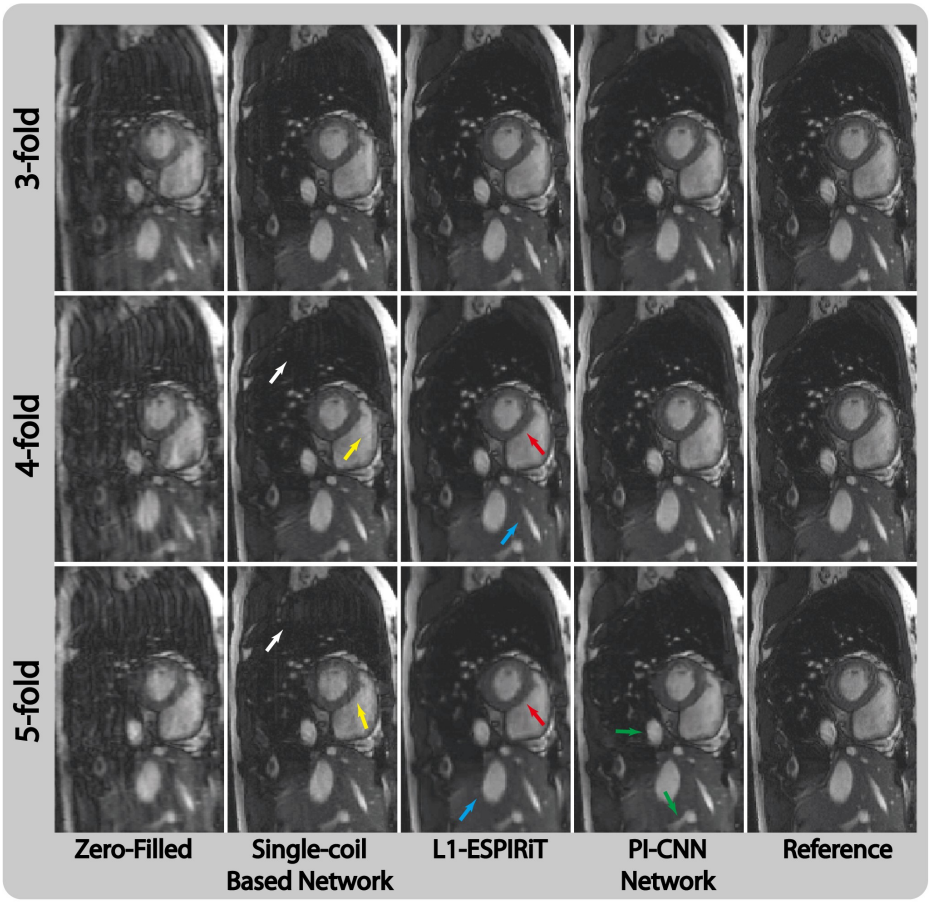

Figure 7-5 Comparison of different reconstruction strategies at three acceleration factors for short-axis cardiac acquisition. From left to right, each column represents selected cardiac frame reconstructed with zero-filling, single-coil based network, L1-ESPIRiT, proposed PI-CNN network and reference, respectively. At 3-fold acceleration, the three reconstructions can all recover decent quality images. At 4-fold acceleration, residual aliasing artifact (white arrow) and over-smoothed blocky artifacts (yellow arrow) appear on single-coil based network reconstruction, while L1-ESPIRiT reconstruction has blurred myocardium (red arrow) and small blood vessel (blue arrow). The proposed PI-CNN method performs well at 4 fold acceleration. At 5-fold acceleration, the proposed PI-CNN network starts to show blurriness at edges (green arrows), whereas image quality based on the other two methods continues to deteriorate.

Table 7-1 Qualitative comparisons of the different reconstruction strategies and the different under-sampling factors in the cardiac and abdominal imaging experiments. A total of 2000 images from the 8 testing subjects (healthy volunteers) in the cardiac imaging and a total of 1000 images from the 4 testing subjects (2 healthy volunteers and 2 patients) in the abdominal image were evaluated for the qualitative comparisons. nRMSE: normalized root mean square error; SSIM: structural similarity index.

		nRMSE	SSIM
Cardiac (3-fold)	**Zero-Filling**	0.284	0.528
	Single-coil Based Network	0.125	0.861
	L1-ESPIRiT	0.082	0.905
	PI-CNN Network	0.081	0.911
Cardiac (4-fold)	**Zero-Filling**	0.425	0.456
	Single-coil Based Network	0.213	0.727
	L1-ESPIRiT	0.134	0.819
	PI-CNN Network	0.103	0.875
Cardiac (5-fold)	**Zero-Filling**	0.586	0.379
	Single-coil Based Network	0.324	0.613
	L1-ESPIRiT	0.202	0.736
	PI-CNN Network	0.158	0.803
Abdominal	**Zero-Filling**	0.302	0.506
	GRAPPA	0.163	0.803
	L1-ESPIRiT	0.116	0.846
	PI-CNN Network	0.094	0.889

Figure 7-6 shows the results of applying the proposed network trained with one acceleration factor to reconstruct images under-sampled with other acceleration factors.

Applying the network trained on 4-fold under-sampled data to 3-fold under-sampled data produces images with the similar quality compared with the image reconstructed directly with a network trained on 3-fold under-sampled data. However, if such network is applied to 5-fold under-sampled data, additional artifact (yellow arrow) and overall increased blurriness can be seen in the reconstructed image. This indicates that for different under-sampling scenarios, in contrast to non-training-based methods like L1-ESPIRiT, which only needs to adapt the regularization parameter value, the proposed network requires adaptive training process to achieve the best performance.

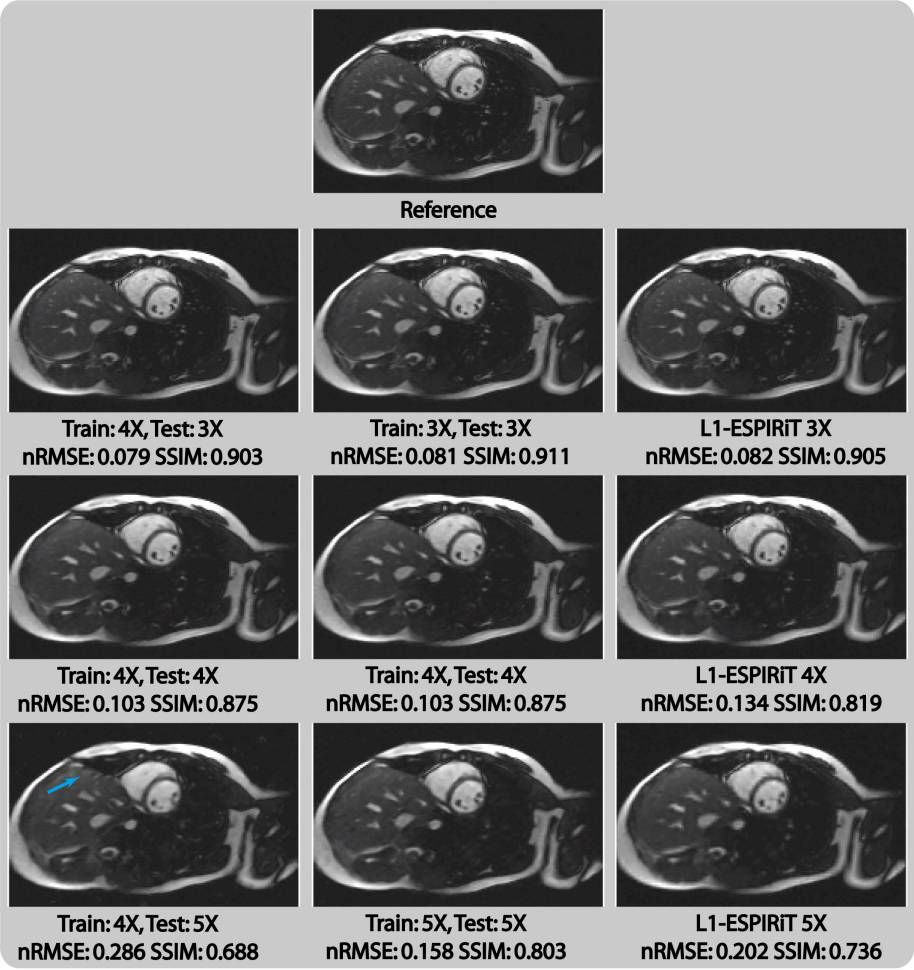

Figure 7-6 Selected cardiac images reconstructed with different testing/training acceleration factor settings in the proposed PI-CNN network. Applying the network trained with 4-fold acceleration factor to data under-sampled with 3-fold can produce images with similar quality compared with

those reconstructed from a matched testing/training acceleration factor setting (both 3-fold). However, using such network to reconstruct data under-sampled with 5-fold demonstrates additional artifact (blue arrow) when compared with those from the matched testing/training acceleration factor setting (both 5-fold). The non-training-based L1-ESPIRiT reconstructions are also shown for comparison. nRMSE and SSIM evaluations for each scenario on the 8 volunteers (2000 images) were also reported in the figure.

Figure 7-7 depicts the reconstruction results of prospectively under-sampled data from GRAPPA, L1-ESPIRiT and the proposed PI-CNN network. We observe the similar performance of the three reconstructions as for the retrospectively study. GRAPPA reconstruction suffers from a high noise level, and L1-ESPIRiT results in residual aliasing artifacts for certain case (blue arrows). On the other hand, the PI-CNN network can produce much cleaner reconstruction and is less prone to remaining artifacts.

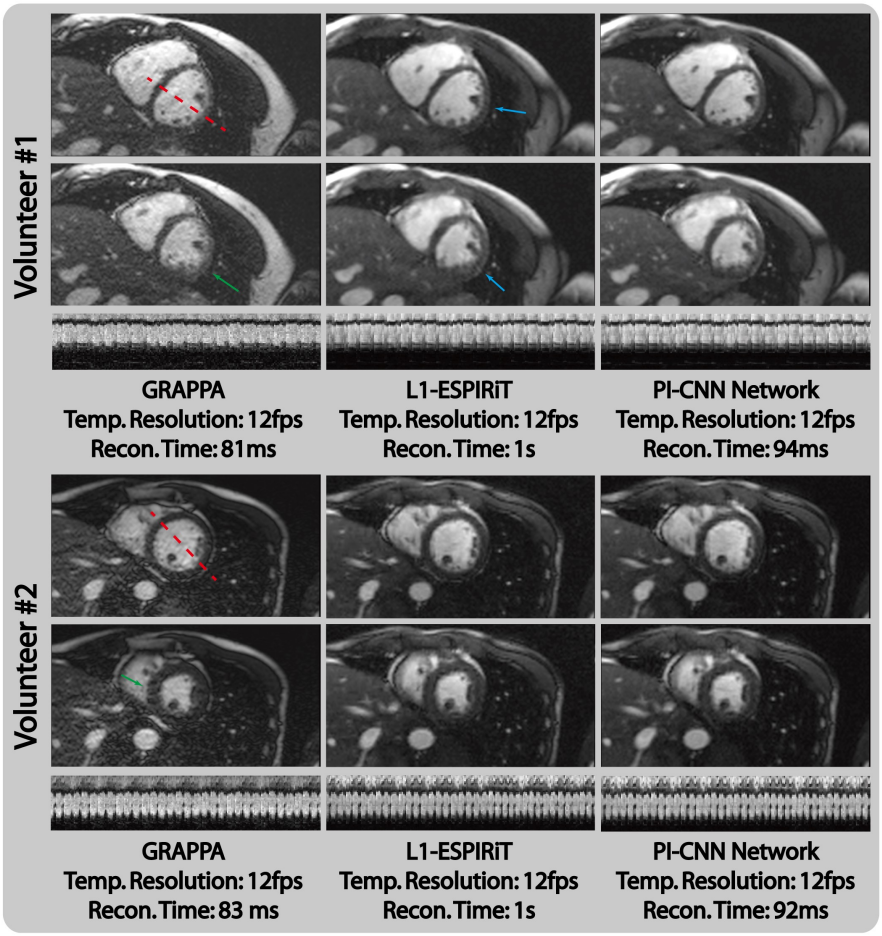

Figure 7-7 Reconstruction results of prospectively 4-fold under-sampled data from GRAPPA, L1-ESPIRiT and the proposed PI-CNN network. Similar behavior is observed as for the retrospective

under-sampled data. GRAPPA reconstruction has high noise level that results in poor visualization of the myocardium (green arrows). L1-ESPIRiT reconstruction has small residual aliasing artifact (blue arrows) in certain case. Reconstructions from the proposed PI-CNN network have less under-sampling artifacts and an improved SNR. As for the reconstruction time, linear GRAPPA reconstruction is the fastest among all three techniques (~82ms/slice), and the proposed PI-CNN network method is slightly slower (~93ms/slice). However, the L1-ESPIRiT took 1s to reconstruct one slice.

Figure 7-8 demonstrates the advantage of the proposed method in single to noise ratio (SNR) limited scenario and its generalization capacity in patient cases. For both healthy volunteers and tumor patients, the linear reconstruction GRAPPA suffers from high noise level due to the poor conditioning of the system matrix in low SNR situation. L1-ESPIRiT was able to reconstruct cleaner images but still has visible noise compared with the reference image. The proposed method, however, was able to reconstruct high quality images with well-delineated tumor regions (blue, yellow and red arrows). Reconstructed images also have a much lower noise floor that makes them comparable to the fully sampled reference. Quantitative measurements shown in Table 7-1 also confirm these observations.

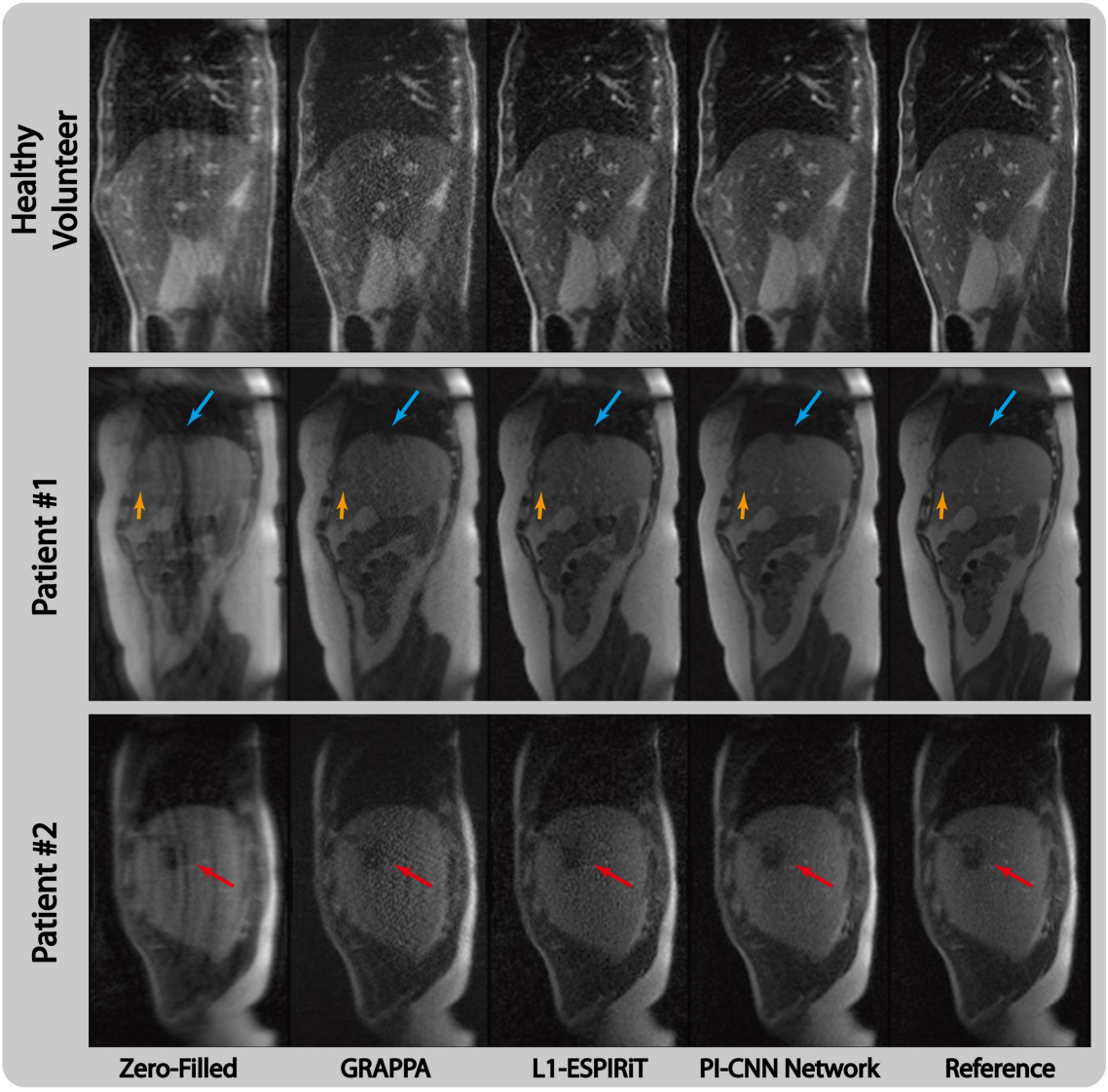

Figure 7-8 Comparison of different reconstruction strategies at 3-fold acceleration factor for sagittal view abdominal acquisitions at 0.35T low-field environment. From left to right, each column represents selected frame reconstructed with zero-filling, GRAPPA, L1-ESPIRiT, proposed PI-CNN network and reference, respectively. Both GRAPPA and L1-ESPIRiT reconstructions suffer from limited SNR that produce noisy images and fail to delineate tumor regions (yellow, blue and red arrows). On the contrary, the proposed PI-CNN network is able to recover much cleaner images that show the tumor region well enough.

The single-coil based network, proposed network, as well as the GRAPPA method, are all compatible with on-the-fly reconstruction. Reconstruction time on eight cores and single GPU was 28ms/frame for the single-coil based network, 46-108ms/frame for proposed method depends on coil number, and 76-95ms/frame for GRAPPA including

calibration weight calculation. L1-ESPIRiT with spatial wavelet constraint, on the other hand, took 1.2-1.4s to reconstruct each frame.

7.4 Discussion

This work demonstrates the feasibility of using a PI and CNN combined network to perform low-latency reconstruction on accelerated real-time acquisitions. By taking advantage of an interleaved PI and CNN reconstruction, the network, once trained, is capable of reconstructing 2D images within tens of milliseconds and will likely enable on-the-fly reconstruction for high spatial and high temporal resolution real-time MRI. In particular, we demonstrated that the PI-CNN network is superior to both previously proposed single-coil based network (144) and L1-ESPIRiT (50) at 4-fold acceleration in 1.5T for real-time cardiac imaging. Comparison with L1-ESPIRiT and clinical available GRAPPA reconstructions at SNR-limited 0.35T environment for real-time abdominal imaging also shows the improved performance of proposed PI-CNN network with 3-fold acceleration.

In recent years, while deep learning has resulted in clear breakthroughs in computer vision related tasks, the application of deep learning to MR reconstruction is just beginning. Previous literature (33,34,144,147) only shows the feasibility of reconstruction with single-coil data and lacks a clear demonstration of how the clinical multiple-coil data are handled. Compared to the selected single-coil based network used in this work, the proposed PI-CNN network includes multi-coil information to allow the network to better de-alias the artifact-contaminated zero-filled input image. Given the same amount of training data and number of epochs, we believed the improved results of the proposed method come from a faster convergence and a smaller gap between the training-testing errors (i.e., less over-

fitting), all resulting from the fact that more (multi-coil) information is included in the PI-CNN network. With a limited number of data available, which is a generally common scenario for deep learning applications in medical imaging, our PI-CNN network can effectively learn the general relationship between the aliasing-contaminated zero-filled image and the clean reference image, and generalize it well to the unseen new inputs. One may argue that more training samples may be easily obtained through image based data augmentation (152), including rigid and regional elastic deformation. However, since multi-coil k-space data is required for the interleaved data consistency layer, it is unclear how to link the deformed image with the k-space data.

The over-fitting issue has always been a concern for learning-based methods, especially with a training dataset of a relatively small size. To alleviate this, the proposed PI-CNN network utilized a cascaded structure that interleaves the CNN layer and PI-DC layer to constrain the size of the receptive field for each layer. The benefit of such strategy can be clearly seen from Figure 7-3. We also carefully choose the parameters related to the network design (K, N, S) that satisfies our application needs, which is essentially a trade-off between model complexity and training efficiency. With increased model complexity (larger K, N, S), the network may be capable of delineating finer structures and removes stronger aliasing artifacts, but requires more training data and longer computation time. With increased training efficiency (smaller K, N, S), the network converges much quicker and need less training data, but it will perform poorly when the under-sampling factor increases. With the current setup ($K = 4$, $N = 5$, $S = 48$), our experiments show the proposed network can recover high quality images with less than 100ms from moderate under-sampled images.

Compared with the conventional CS approaches, the proposed learning-based PI-CNN network offers two distinct advantages for image reconstruction. First, CS methods usually require the selection of specific sparsifying transform(s) as regularization term(s) to constrain the solution space for the under-determined problem, which is not a trivial task. Using the learning-based approach allows the network to adapt its kernels to the underlying features of the image and artifacts automatically and requires minimal human interaction. Based on criteria given by the loss function, the training process optimally adjusts the convolutional kernels such that the output matches well with the reference. However, such data-driven-based adaption from the training process can also limit the way that a learned network is used for reconstruction. As shown in Figure 6, if the severity of aliasing artifacts is drastically different between the training and application stages, learning-based PI-CNN network performs inferior to the CS approach. Fortunately, recent research results have highlighted the potential of transfer learning (35) to handle this training-application mismatch. Its applicability to our proposed PI-CNN network warrants future study. Second, CS reconstruction usually requires long reconstruction time since every reconstruction is treated as an individual optimization problem. On the contrary, the learning-based PI-CNN network offloads the computational expensive optimization process offline and pre-calculates the network parameters. Once the parameters are determined, the application to new data is extremely fast since no optimization is needed.

Our study shows that the proposed network can learn the general and global mapping from under-sampled aliased image to reference image, using different sampling patterns with fixed under-sampling factor during the training. This suggests that a fixed aliasing pattern or strong incoherence is not required, although more incoherent aliasing from

trajectories such as radial sampling might be helpful at higher under-sampling factor. To further improve the network, one may pre-train the network with various under-sampling masks, and fine tune it with a fixed pattern that will be finally used in the prospective study. Furthermore, jointly training the under-sampling mask and aliased image for reconstruction may provide further improvement.

In the proposed PI-CNN network, we utilized the multi-coil information through an interleaved PI-DC layer, which is essentially solving a parallel image problem with pre-calculated sensitivity maps. Alternatively, the multi-coil data can be input into the network directly, and let the network itself to learn the implicit relationship between coils. This could be better than the proposed approach which uses the coil sensitivity explicitly, but will greatly increase the network size and requires more processing such as data shuffling to prevent the network from learning a fixed coil arrangement.

In the low-field abdominal imaging experiment, we incorporated patient cases to demonstrate the generalization capability of the proposed network. We ascribe the high quality reconstruction on patient data partly to the fact that we incorporate k-space data into the network and enforce the consistency repeatedly. This allows the network to capture the unseen features, including the pathology related features, during the application stage. However, since there is no clear idea what exactly the convolutional kernels represent in a learned network, the capacity of the proposed network to handle more complicated pathology cases remains undefined and warrants further investigation.

7.5 Conclusion

In conclusion, by taking advantage of multi-coil information and convolutional neural network, a PI-CNN reconstruction network has been successfully implemented and

evaluated in both cardiac and abdominal real-time imaging on retrospective and prospective data. Better image quality was achieved using the proposed PI-CNN network than a single-coil based reconstruction network, L1-ESPIRiT and GRAPPA on moderate 3X-4X acceleration. In terms of reconstruction speed, the proposed method can achieve less than 100ms reconstruction for clinical multi-coil data, which implies its potential of real-time reconstruction for real-time imaging applications.

Chapter 8 Summary and Future Work

This dissertation presented several application-tailored accelerated MR imaging methods. More specifically, two methods to improve the scan efficiency were discussed for Ferumoxytol-enhanced 4D multi-phase cardiovascular MR in Chapter 3 and 4; one method to reduce temporal blurring was exploited for ASL-based noncontrast-enhanced 4D intracranial MR angiography in Chapter 5 and stands upon this, a general strategy to improve 3D volumetric imaging using radial trajectory was analyzed in Chapter 6; finally one method to enable low-latency on-the-fly reconstruction was demonstrated for real-time imaging in Chapter 7. The proposed methods were all designed with application specificity and clinically utility in mind, and they can be applied to many other applications that have similar SNR level, clinical requirement etc. By exploiting the potential of these particular applications, the idea was not to only improve the performance of current applications, but to build ideology for solving other limitations that may occur in future applications.

In this chapter, the technical developments mentioned in this dissertation are first summarized. Potential directions for future works are then described at the end of this chapter.

8.1 Summary of technical development

8.1.1 4D MUSIC with Reduced Acquisition Time

By taking advantage of the high SNR results from Ferumoxytol contrast enhancement in 4D MUSIC, acquisition time was reduced using k-space under-sampling with a carefully designed center-out elliptical variable density Poisson-disc pattern. A simple yet effective compressed sensing and parallel imaging reconstruction was employed to reconstruct

under-sampled data to maintain the image quality. In addition, an inline image reconstruction pipeline was also developed and fully integrated with the existing clinical workflow that provides a powerful platform to translate the advanced image reconstruction algorithms into daily clinical practice without interrupting normal clinical workflow.

8.1.2 4D MUSIC with Improved Temporal Resolution

4D MUSIC in its current format provides exquisite delineation of anatomical structures but fails short of allowing comprehensive cardiac functional assessment due to the limited temporal resolution. A motion weighted reconstruction approach is utilized to reconstruct the same 4D MUSIC dataset but binned into more cardiac phases for improved temporal resolution. By incorporating k-space data acquired in adjacent cardiac phases, and assignment corresponding 0 to 1 weights in the data fidelity, effective under-sampling factor can be reduced while cardiac motion is suppressed through the iterative reconstruction process. As result, spatial resolution is preserved without motion corruption and temporal resolution is doubled.

8.1.3 Magnitude Subtraction for Accelerated ASL-based MR Angiography

Considering the inherently low SNR level of ASL signal, straightforward employment of conventional simple compressed sensing and parallel imaging reconstruction as in 4D MUSIC application usually results in blurry and artifact contaminated reconstruction. A magnitude subtraction regularization term that exploits the unique image generation process of MR angiography with ASL-based acquisition is incorporated in the reconstruction process. This in combination with the radial stack-of-stars trajectory permits a higher level of sparsity and finer constraint on the solution space in the optimization reconstruction, which translates to sharper images.

8.1.4 Rotated Stack-of-Stars Trajectory

Conventional stack-of-stars trajectory, for example the one used in ASL-based MRA application, acquires the same spoke angles for all partitions. In k-space under-sampling scenario, this only generates incoherent artifacts within each partition but not across partitions. By simply rotating the angle arrangement in a golden-angle manner along the partition direction (regardless of the angle arrangement within each partition), streaking artifacts can be greatly reduced due to a more efficient 3D k-space sampling and more spread-out incoherent artifacts. This in turn allows improved image quality for general 3D volumetric imaging.

8.1.5 Low-Latency Accelerated Real-Time Imaging

Despite the great success and wide adoption of optimization-based reconstruction methods, which are used for the previous two applications, its reconstruction speed is sometimes insufficient for application such as real-time imaging, which benefits from on-the-fly image feedback. By resolving the conventional parallel imaging reconstruction as gradient descent steps and interleaving with convolutional layers in a general convolutional neural network, a learning based reconstruction framework is proposed to offload the computation burden as an offline training process. Once parameters for the network are learned, it can be applied to reconstruct un-seen under-sampled data within hundreds of milliseconds.

8.2 Future outlook

8.2.1 Dual Motion-Weighted 4D MUSIC

For the motion weighted reconstruction introduced in chapter 4, acquired k-space data were first rejected or accepted through a binary thresholding mask along the respiratory dimension to perform respiratory gating. However, the similar motion weighting idea used along cardiac dimension in motion weighted reconstruction can be directly applied in the respiratory dimension. This can incorporate more k-space into image reconstruction, which allows for an SNR boost in the final reconstruction.

A schematic plot of respiratory and cardiac dual motion weighted reconstruction is shown in Figure 8-1. Each readout was first weighted according to the respiratory distance of its corresponding position to the reference position (end-expiration) using a Gaussian kernel that centered at reference position (respiratory motion weighting). The kernel parameter was chosen such that only 25% of data's weight is larger than 0.8. Respiratory weighted data was further weighted according to their cardiac position using a flat-topped Gaussian kernel that slides through each cardiac phase (cardiac motion weighting). Resulting dual motion-weighted (or soft-gating as contrast binary hard-gating) data was feed into the same phase-by-phase reconstruction using Equation 4-2.

Figure 8-2 shows an example for an 18-phases reconstruction using the dual motion-weighted strategy and motion regularized strategy (Strategy 2 in chapter 4) on a 2-day-old male patient with heart rate of 135bpm. As shown, both reconstructions are able to suppress respiratory motion with sharp diaphragm boundary and resolve cardiac motion with clear visualization of mitral valve. However, reconstruction time of the dual motion-weighted reconstruction is only 1/9 of that of motion regularized reconstruction.

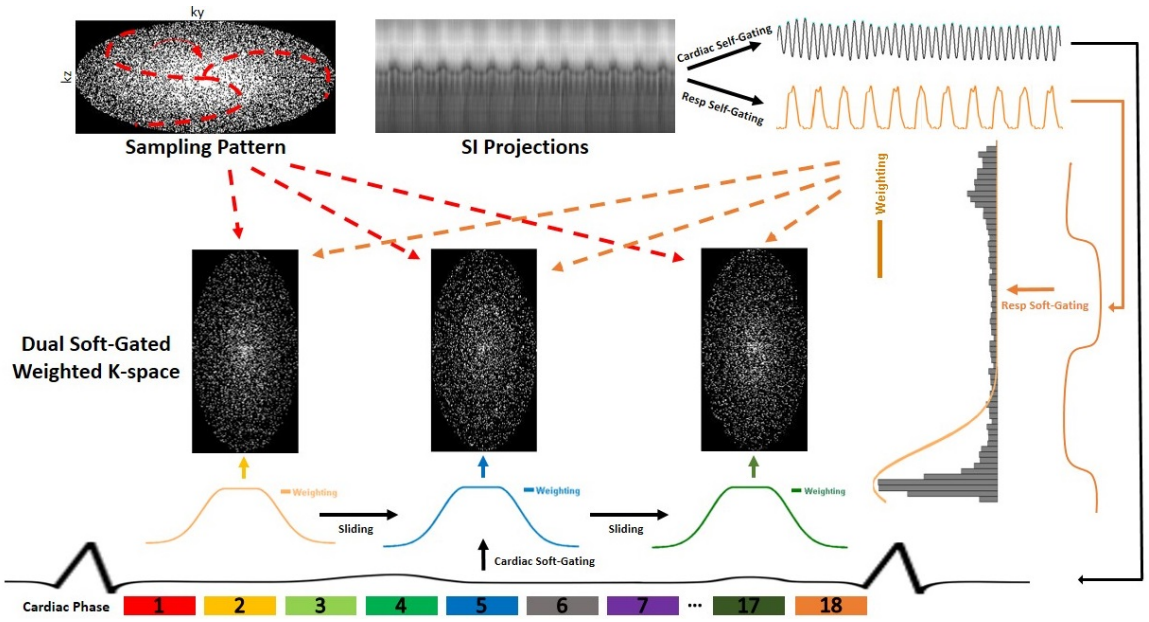

Figure 8-1 Schematics of proposed workflow. K-space is acquired with golden-angle rotated spiral-like arms on Cartesian grid. Frequently sampled SI projections provide accurate estimation of physiological motions, based on which soft-gating (SG) weights are generated using Gaussian kernels. Combining these weights, acquired k-space are retrospectively binned into 18 cardiac phases.

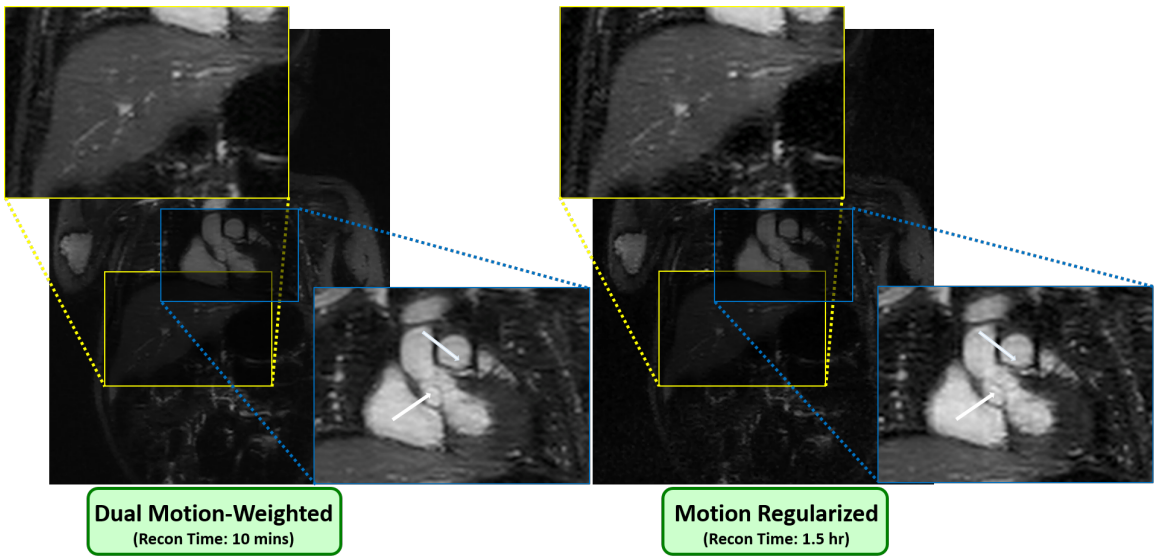

Figure 8-2 Example reconstruction images from respiratory and cardiac dual motion-weighted strategy, and conventional motion regularized strategy.

8.2.2 Rotated Stack-of-Stars at Low-Field Environment

The rotated stack-of-star radial trajectory developed in chapter 6 is an efficient 3D k-space sampling strategy. Its advantage over conventional aligned stack-of-stars trajectory not only lies in the regime of heavy k-space under-sampling, as shown in detail in chapter 6, but also lies in the SNR-limited scenario, which is partially demonstrated in chapter 6 using the ASL application. Such advantage in SNR-limited scenario can be further investigated in the low-filed environment, where SNR is proportional to the field strength.

We have ported the rotated stack-of-stars sequence to a 0.35T low-filed MR scanner, which is essentially a sub-portion of a MRI-guided radiotherapy system (ViewRay, Cleveland, OH). Daily basis treatment planning and radiation delivery were performed on this system, with conventional 3D Cartesian bSSFP sequence being used as the baseline anatomical reference volumetric imaging. The rotated radial stack-of-stars sequence allows free-breathing acquisition and is insensitive to bulk body motion when compared to the conventional Cartesian acquisition. In combination with compressed sensing reconstruction algorithm, it can be a useful tool for MR-based treatment planning, especially for patients who cannot hold their breath or remain still. Figure 8-3 shows an example of patient with intrahepatic bile duct carcinoma, with images acquired during free-breathing using the rotated radial stack-of-stars sequence and conventional Cartesian sequence. As clearly visualized, the patient failed to hold his breath during the standard Cartesian acquisition, resulting in strong motion artifacts (yellow arrow). The proposed sequence was able to reduce such motion artifacts and reveal clear boundary of the tumor region (blue arrow).

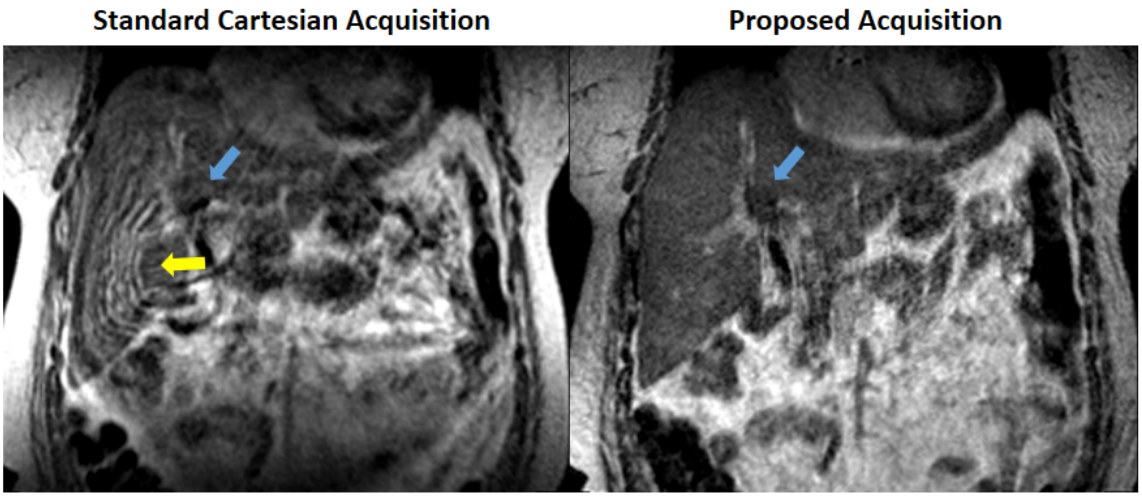

Figure 8-3 Example of rotated radial stack-of-stars sequence on the ViewRay system. It has better motion robustness when compared with standard Cartesian sequence.

REFERENCE

1. Sodickson DK, Manning WJ. Simultaneous acquisition of spatial harmonics (SMASH): fast imaging with radiofrequency coil arrays. Magn. Reson. Med. 1997;38:591–603.

2. Griswold MA, Jakob PM, Nittka M, Goldfarb JW, Haase A. Partially Parallel Imaging with Localized Sensitivities (PILS). Magn. Reson. Med. 2000;44:602–609. doi: 10.1002/1522-2594(200010)44:4<602::AID-MRM14>3.0.CO;2-5.

3. Pruessmann KP, Weiger M, Scheidegger MB, Boesiger P. SENSE: sensitivity encoding for fast MRI. Magn. Reson. Med. 1999;42:952–62.

4. Griswold MA, Jakob PM, Heidemann RM, Nittka M, Jellus V, Wang J, Kiefer B, Haase A. Generalized autocalibrating partially parallel acquisitions (GRAPPA). Magn. Reson. Med. 2002;47:1202–10.

5. Lustig M, Donoho D, Pauly JM. Sparse MRI: The application of compressed sensing for rapid MR imaging. Magn. Reson. Med. 2007;58:1182–95.

6. Lustig M, Donoho DL, Santos JM, Pauly JM. Compressed Sensing MRI. IEEE Signal Process. Mag. 2008;25:72–82.

7. Zhou Z, Han F, Rapacchi S, Nguyen K-L, Brunengraber DZ, Kim G-HJ, Finn JP, Hu P. Accelerated ferumoxytol-enhanced 4D multiphase, steady-state imaging with contrast enhancement (MUSIC) cardiovascular MRI: validation in pediatric congenital heart disease. NMR Biomed. 2016. doi: 10.1002/nbm.3663.

8. Zhou Z, Han F, Yu S, Yu D, Rapacchi S, Song HK, Wang DJJ, Hu P, Yan L. Accelerated noncontrast-enhanced 4-dimensional intracranial MR angiography using golden-angle stack-of-stars trajectory and compressed sensing with magnitude subtraction. Magn. Reson. Med. 2018;79:867–878. doi: 10.1002/mrm.26747.

9. Zhou Z, Han F, Yan L, Wang DJJ, Hu P. Golden-ratio rotated stack-of-stars acquisition for improved volumetric MRI. Magn. Reson. Med. 2017;78:2290–2298. doi: 10.1002/mrm.26625.

10. Liang Z-P, Lauterbur PC. Principles of magnetic resonance imaging: a signal processing perspective. IEEE Press 2000:416. doi: 10.1109/MEMB.2000.870245.

11. Bernstein MA, King KF, Zhou XJ. Handbook of MRI Pulse Sequences. 2004. doi: 10.1016/B978-0-12-092861-3.X5000-6.

12. Jung Y, Jashnani Y, Kijowski R, Block WF. Consistent non-cartesian off-axis MRI quality: calibrating and removing multiple sources of demodulation phase errors. Magn. Reson. Med. 2007;57:206–12.

13. Brodsky EK, Samsonov AA, Block WF. Characterizing and correcting gradient errors in non-cartesian imaging: Are gradient errors linear time-invariant (LTI)? Magn. Reson. Med. 2009;62:1466–76.

14. Glover GH, Pauly JM. Projection Reconstruction Techniques for Reduction of Motion Effects in MRI. Magn. Reson. Med. 1992;28:275–289. doi: 10.1002/mrm.1910280209.

15. Scheffler K, Hennig J. Reduced circular field-of-view imaging. Magn. Reson. Med. 1998;40:474–480. doi: 10.1002/mrm.1910400319.

16. Pipe JG. Motion correction with PROPELLER MRI: application to head motion and free-breathing cardiac imaging. Magn. Reson. Med. 1999;42:963–9.

17. Fessler JA. On NUFFT-based gridding for non-Cartesian MRI. J. Magn. Reson. 2007;188:191–195. doi: 10.1016/j.jmr.2007.06.012.

18. Fessler JA, Sutton BP. Nonuniform fast Fourier transforms using min-max interpolation. IEEE Trans. Signal Process. 2003;51:560–574. doi: 10.1109/TSP.2002.807005.

19. Asif MS, Hamilton L, Brummer M, Romberg J. Motion-adaptive spatio-temporal regularization for accelerated dynamic MRI. Magn. Reson. Med. 2013;70:800–12.

20. Adluru G, Awate SP, Tasdizen T, Whitaker RT, Dibella EVR. Temporally constrained reconstruction of dynamic cardiac perfusion MRI. Magn. Reson. Med. 2007;57:1027–36.

21. Tsao J, Kozerke S. MRI temporal acceleration techniques. J. Magn. Reson. Imaging 2012;36:543–60.

22. Feng L, Axel L, Chandarana H, Block KT, Sodickson DK, Otazo R. XD-GRASP: Golden-angle radial MRI with reconstruction of extra motion-state dimensions using compressed sensing. Magn. Reson. Med. 2015;0:n/a-n/a.

23. Feng L, Coopo S, Piccini D, Lim RP, Stuber M, Sodickson DK OR. Five-Dimensional Cardiac and Respiratory Motion-Resolved Whole-Heart MRI. In: proceedings of the 23rd ISMRM annaual meeting2. Toronto, Canada; 2015.

24. Rudin LI, Osher S, Fatemi E. Nonlinear total variation noise removal algorithm. Phys. D Nonlinear Phenom. [Internet] 1992;60:259–268. doi: 10.1016/0167-2789(92)90242-F.

25. Lecun Y, Bengio Y, Hinton G. Deep learning. Nature 2015;521:436–444. doi: 10.1038/nature14539.

26. Goodfellow, Ian, Bengio, Yoshua, Courville A. Deep Learning. MIT Press [Internet] 2016.

27. Krizhevsky A, Sutskever I, Geoffrey E. H. ImageNet Classification with Deep Convolutional Neural Networks. Adv. Neural Inf. Process. Syst. 25 [Internet] 2012:1–9. doi: 10.1109/5.726791.

28. Chen Y, Yu W, Pock T. On learning optimized reaction diffusion processes for effective image restoration. In: Proceedings of the IEEE Computer Society Conference on Computer Vision and Pattern Recognition. Vol. 07–12–June. ; 2015. pp. 5261–5269. doi: 10.1109/CVPR.2015.7299163.

29. Golkov V, Dosovitskiy A, Sperl JI, Menzel MI, Czisch M, Sämann P, Brox T, Cremers D. q-Space Deep Learning: Twelve-Fold Shorter and Model-Free Diffusion MRI Scans. IEEE Trans. Med. Imaging 2016;35:1344–1351. doi: 10.1109/TMI.2016.2551324.

30. Kleesiek J, Urban G, Hubert A, Schwarz D, Maier-Hein K, Bendszus M, Biller A. Deep MRI brain extraction: A 3D convolutional neural network for skull stripping. Neuroimage 2016;129:460–469. doi: 10.1016/j.neuroimage.2016.01.024.

31. Ravishankar S, Bresler Y. MR image reconstruction from highly undersampled k-space data by dictionary learning. IEEE Trans. Med. Imaging 2011;30:1028–1041. doi: 10.1109/TMI.2010.2090538.

32. Caballero J, Price AN, Rueckert D, Hajnal J V. Dictionary learning and time sparsity for dynamic MR data reconstruction. IEEE Trans. Med. Imaging 2014;33:979–994. doi: 10.1109/TMI.2014.2301271.

33. Wang S, Su Z, Ying L, Peng X, Zhu S, Liang F, Feng D, Liang D. Accelerating magnetic resonance imaging via deep learning. In: 2016 IEEE 13th International Symposium on Biomedical Imaging (ISBI). ; 2016. pp. 514–517. doi: 10.1109/ISBI.2016.7493320.

34. Yang Y, Sun J, Li H, Xu Z. Deep ADMM-Net for Compressive Sensing MRI. NIPS - Adv. Neural Inf. Process. Syst. 2017:10–18.

35. Han Y, Yoo J, Kim HH, Shin HJ, Sung K, Ye JC. Deep learning with domain adaptation for accelerated projection-reconstruction MR. Magn. Reson. Med. 2018. doi: 10.1002/mrm.27106.

36. Hammernik K, Klatzer T, Kobler E, Recht MP, Sodickson DK, Pock T, Knoll F. Learning a Variational Network for Reconstruction of Accelerated MRI Data. 2017;3071:3055–3071. doi: 10.1002/mrm.26977.

37. Zhu B, Liu JZ, Rosen BR, Rosen MS. Image reconstruction by domain transform manifold learning. Nat. Publ. Gr. [Internet] 2017;555:487–492. doi: 10.1017/CCOL052182303X.002.

38. Prince MR, Yucel EK, Kaufman JA, Harrison DC, Geller SC. Dynamic gadolinium- enhanced three- dimensional abdominal MR arteriography. J. Magn. Reson. Imaging 1993;3:877–881. doi: 10.1002/jmri.1880030614.

39. Saleh RS, Patel S, Lee MH, Boechat MI, Ratib O, Saraiva CR, Finn JP. Contrast-enhanced MR angiography of the chest and abdomen with use of controlled apnea in children. Radiology 2007;243:837–46.

40. Prince MR, Narasimham DL, Stanley JC, Chenevert TL, Williams DM, Marx M V, Cho KJ. Breath-hold gadolinium-enhanced MR angiography of the abdominal aorta and its major branches. Radiology [Internet] 1995;197:785–792. doi: 10.1148/radiology.197.3.7480757.

41. Han F, Rapacchi S, Khan S, Ayad I, Salusky I, Gabriel S, Plotnik A, Finn JP, Hu P. Four-dimensional, multiphase, steady-state imaging with contrast enhancement (MUSIC) in the heart: A feasibility study in children. Magn. Reson. Med. 2015;74:1042–1049.

42. Li W, Tutton S, Vu AT, Pierchala L, Li BSY, Lewis JM, Prasad P V, Edelman RR. First-pass contrast-enhanced magnetic resonance angiography in humans using ferumoxytol, a novel ultrasmall superparamagnetic iron oxide (USPIO)-based blood pool agent. J. Magn. Reson. Imaging 2005;21:46–52.

43. Donoho DL. Compressed sensing. IEEE Trans. Inf. Theory 2006;52:1289–1306. doi: Doi 10.1109/Tit.2006.871582.

44. Gamper U, Boesiger P, Kozerke S. Compressed sensing in dynamic MRI. Magn. Reson. Med. 2008;59:365–373. doi: 10.1002/mrm.21477.

45. Rapacchi S, Han F, Natsuaki Y, Kroeker R, Plotnik A, Lehrman E, Sayre J, Laub G, Finn JP, Hu P. High spatial and temporal resolution dynamic contrast-enhanced magnetic resonance angiography using compressed sensing with magnitude image subtraction. Magn. Reson. Med. 2014;71:1771–83.

46. Murphy M, Alley M, Demmel J, Keutzer K, Vasanawala S, Lustig M. Fast l_1 -SPIRiT compressed sensing parallel imaging MRI: scalable parallel implementation and clinically feasible runtime. IEEE Trans. Med. Imaging 2012;31:1250–62. doi: 10.1109/TMI.2012.2188039.

47. Wu XL, Gai J, Lam F, Fu M, Haldar JP, Zhuo Y, Liang ZP, Hwu WM, Sutton BP. Impatient MRI: Illinois Massively Parallel Acceleration Toolkit for image reconstruction with enhanced throughput in MRI. In: Proceedings - International Symposium on Biomedical Imaging. ; 2011. pp. 69–72. doi: 10.1109/ISBI.2011.5872356.

48. Cook RL. Stochastic sampling in computer graphics. ACM Trans. Graph. [Internet] 1986;5:51–72. doi: 10.1145/7529.8927.

49. Wilman AH, Riederer SJ. Performance of an elliptical centric view order for signal enhancement and motion artifact suppression in breath-hold three-dimensional gradient echo imaging. Magn. Reson. Med. 1997;38:793–802. doi: 10.1002/mrm.1910380516.

50. Uecker M, Lai P, Murphy MJ, Virtue P, Elad M, Pauly JM, Vasanawala SS, Lustig M. ESPIRiT-an eigenvalue approach to autocalibrating parallel MRI: Where SENSE meets GRAPPA. Magn. Reson. Med. 2013;1001:990–1001.

51. Tamir JI, Ong F, Cheng JY, Uecker M, Lustig M. Generalized Magnetic Resonance Image Reconstruction using The Berkeley Advanced Reconstruction Toolbox. Proc. ISMRM 2016 Data Sampl. Image Reconstr. Work. [Internet] 2016;2486:9660006. doi: 10.5281/zenodo.31907.

52. Dagum L, Menon R. OpenMP: an industry standard API for shared-memory programming. IEEE Comput. Sci. Eng. [Internet] 1998;5:46–55. doi: 10.1109/99.660313.

53. Prince MR, Zhang HL, Chabra SG, Jacobs P, Wang Y. A pilot investigation of new superparamagnetic iron oxide (ferumoxytol) as a contrast agent for cardiovascular MRI. J. Xray. Sci. Technol. 2003;11:231–40.

54. Sigovan M, Gasper W, Alley H, Owens C, Saloner D. USPIO-enhanced MR angiography of arteriovenous fistulas in patients with renal failure. Radiology 2012;265(2):584–90.

55. Bashir MR, Mody R, Neville A, Javan R, Seaman D, Kim CY, Gupta RT, Jaffe T a. Retrospective assessment of the utility of an iron-based agent for contrast-enhanced magnetic resonance venography in patients with endstage renal diseases. J. Magn. Reson. Imaging 2014;40:113–8.

56. Wang Z, Bovik AC, Sheikh HR, Simoncelli EP. Image quality assessment: From error visibility to structural similarity. IEEE Trans. Image Process. 2004;13:600–612. doi: 10.1109/TIP.2003.819861.

57. Lin LI-K. A Concordance Correlation Coefficient to Evaluate Reproducibility. Biometrics [Internet] 1989;45:255. doi: 10.2307/2532051.

58. Stalder AF, Schmidt M, Quick HH, Schlamann M, Maderwald S, Schmitt P, Wang Q, Nadar MS, Zenge MO. Highly undersampled contrast-enhanced MRA with iterative reconstruction: Integration in a clinical setting. Magn. Reson. Med. 2015;74:1652–1660. doi: 10.1002/mrm.25565.

59. Carr JC, Simonetti O, Bundy J, Li D, Pereles S, Finn JP. Cine MR angiography of the heart with segmented true fast imaging with steady-state precession. Radiology [Internet] 2001;219:828–34. doi: 10.1148/radiology.219.3.r01jn44828.

60. Jung BA, Hennig J, Scheffler K. Single-breathhold 3D-trueFISP cine cardiac imaging. Magn. Reson. Med. 2002;48:921–925. doi: 10.1002/mrm.10280.

61. Larson AC, White RD, Laub G, McVeigh ER, Li D, Simonetti OP. Self-gated cardiac cine MRI. Magn. Reson. Med. 2004;51:93–102.

62. Hu P, Hong S, Moghari MH, Goddu B, Goepfert L, Kissinger K V, Hauser TH, Manning WJ, Nezafat R. Motion correction using coil arrays (MOCCA) for free-breathing cardiac cine MRI. Magn. Reson. Med. 2011;66:467–75.

63. Ntsinjana HN, Hughes ML, Taylor AM. The Role of Cardiovascular Magnetic Resonance in Pediatric Congenital Heart Disease. J. Cardiovasc. Magn. Reson. 2011;13:51.

64. Bailliard F, Hughes ML, Taylor AM. Introduction to cardiac imaging in infants and children: Techniques, potential, and role in the imaging work-up of various cardiac malformations and other pediatric heart conditions. Eur. J. Radiol. 2008;68:191–198. doi: 10.1016/j.ejrad.2008.05.016.

65. Fratz S, Chung T, Greil GF, Samyn MM, Taylor AM, Valsangiacomo Buechel ER, Yoo S-J, Powell AJ. Guidelines and protocols for cardiovascular magnetic resonance in children and adults with congenital heart disease: SCMR expert consensus group on congenital heart disease. J. Cardiovasc. Magn. Reson. [Internet] 2013;15:51. doi: 10.1186/1532-429X-15-51.

66. Han F, Zhou Z, Han E, Gao Y, Nguyen KL, Finn JP, Hu P. Self-gated 4D multiphase, steady-state imaging with contrast enhancement (MUSIC) using rotating cartesian K-space (ROCK): Validation in children with congenital heart disease. Magn. Reson. Med. 2017;78:472–483. doi: 10.1002/mrm.26376.

67. Nguyen KL, Han F, Zhou Z, Brunengraber DZ, Ayad I, Levi DS, Satou GM, Reemtsen BL, Hu P, Finn JP. 4D MUSIC CMR: value-based imaging of neonates and infants with congenital heart disease. J. Cardiovasc. Magn. Reson. 2017;19. doi: 10.1186/s12968-017-0352-8.

68. Tsao J, Boesiger P, Pruessmann KP. k-t BLAST and k-t SENSE: Dynamic MRI With High Frame Rate Exploiting Spatiotemporal Correlations. Magn. Reson. Med. 2003;50:1031–1042. doi: 10.1002/mrm.10611.

69. Jung H, Sung K, Nayak KS, Kim EY, Ye JC. K-t FOCUSS: A general compressed sensing framework for high resolution dynamic MRI. Magn. Reson. Med. 2009;61:103–116. doi: 10.1002/mrm.21757.

70. Lustig M, Santos JM, Donoho D, Pauly JM. k-t SPARSE: high frame rate dynamic MRI exploiting spatio-temporal sparsity. Proc. ISMRM, Seattle 2006;50:2420.

71. Lingala SG, Hu Y, Dibella E, Jacob M. Accelerated dynamic MRI exploiting sparsity and low-rank structure: K-t SLR. IEEE Trans. Med. Imaging 2011;30:1042–1054. doi: 10.1109/TMI.2010.2100850.

72. Otazo R, Candès E, Sodickson DK. Low-rank plus sparse matrix decomposition for accelerated dynamic MRI with separation of background and dynamic components. Magn. Reson. Med. 2015;73:1125–1136. doi: 10.1002/mrm.25240.

73. Feng L, Srichai MB, Lim RP, Harrison A, King W, Adluru G, Dibella EVR, Sodickson DK, Otazo R, Kim D. Highly accelerated real-time cardiac cine MRI using k-t SPARSE-SENSE. Magn. Reson. Med. 2013;70:64–74. doi: 10.1002/mrm.24440.

74. Kozerke S, Tsao J, Razavi R, Boesiger P. Accelerating cardiac cine 3D imaging using k-t BLAST. Magn. Reson. Med. 2004;52:19–26. doi: 10.1002/mrm.20145.

75. Usman M, Atkinson D, Odille F, Kolbitsch C, Vaillant G, Schaeffter T, Batchelor PG, Prieto C. Motion corrected compressed sensing for free-breathing dynamic cardiac MRI. Magn. Reson. Med. 2013;70:504–516. doi: 10.1002/mrm.24463.

76. Jiang W, Ong F, Johnson KM, Nagle SK, Hope TA, Lustig M, Larson PEZ. Motion robust high resolution 3D free-breathing pulmonary MRI using dynamic 3D image self-navigator. Magn. Reson. Med. [Internet] 2017. doi: 10.1002/mrm.26958.

77. Johnson KM, Block WF, Reeder SB, Samsonov A. Improved least squares MR image reconstruction using estimates of k-space data consistency. Magn. Reson. Med. 2012;67:1600–8.

78. Forman C, Piccini D, Grimm R, Hutter J, Hornegger J, Zenge MO. Reduction of respiratory motion artifacts for free-breathing whole-heart coronary MRA by weighted iterative reconstruction. Magn. Reson. Med. 2015;73:1885–1895.

79. Cheng JY, Zhang T, Ruangwattanapaisarn N, Alley MT, Uecker M, Pauly JM, Lustig M, Vasanawala SS. Free-breathing pediatric MRI with nonrigid motion correction and acceleration. J. Magn. Reson. Imaging 2015;42:407–420.

80. Feng L, Huang C, Shanbhogue K, Sodickson DK, Chandarana H, Otazo R. RACER-GRASP: Respiratory-weighted, aortic contrast enhancement-guided and coil-unstreaking golden-angle radial sparse MRI. Magn. Reson. Med. 2017. doi: 10.1002/mrm.27002.

81. Cheng JY, Hanneman K, Zhang T, Alley MT, Lai P, Tamir JI, Uecker M, Pauly JM, Lustig M, Vasanawala SS. Comprehensive motion-compensated highly accelerated 4D flow MRI with ferumoxytol enhancement for pediatric congenital heart disease. J. Magn. Reson. Imaging 2016;43(6):1355–68.

82. McGee KP, Manduca A, Felmlee JP, Riederer SJ, Ehman RL. Image metric-based correction (Autocorrection) of motion effects: Analysis of image metrics. J. Magn. Reson. Imaging 2000;11:174–181. doi: 10.1002/(SICI)1522-2586(200002)11:2<174::AID-JMRI15>3.0.CO;2-3.

83. Willinsky RA, Taylor SM, terBrugge K, Farb RI, Tomlinson G, Montanera W. Neurologic Complications of Cerebral Angiography: Prospective Analysis of 2,899

Procedures and Review of the Literature. Radiology [Internet] 2003;227:522–528. doi: 10.1148/radiol.2272012071.

84. Yan L, Wang S, Zhuo Y, Wolf RL, Stiefel MF, An J, Ye Y, Zhang Q, Melhem ER, Wang DJJ. Unenhanced dynamic MR angiography: high spatial and temporal resolution by using true FISP-based spin tagging with alternating radiofrequency. Radiology [Internet] 2010;256:270–279. doi: 10.1148/radiol.10091543.

85. Bi X, Weale P, Schmitt P, Zuehlsdorff S, Jerecic R. Non-contrast-enhanced four-dimensional (4D) intracranial MR angiography: A feasibility study. Magn. Reson. Med. 2010;63:835–841. doi: 10.1002/mrm.22220.

86. Lanzman RS, Kröpil P, Schmitt P, et al. Nonenhanced ECG-gated time-resolved 4D steady-state free precession (SSFP) MR angiography (MRA) for assessment of cerebral collateral flow: Comparison with digital subtraction angiography (DSA). Eur. Radiol. 2011;21:1329–1338. doi: 10.1007/s00330-010-2051-9.

87. Raoult H, Bannier E, Robert B, Barillot C, Schmitt P, Gauvrit J-Y. Time-resolved spin-labeled MR angiography for the depiction of cerebral arteriovenous malformations: a comparison of techniques. Radiology [Internet] 2014;271:524–33. doi: 10.1148/radiol.13131252.

88. Wu H, Block WF, Turski PA, Mistretta CA, Johnson KM. Noncontrast-enhanced three-dimensional (3D) intracranial MR angiography using pseudocontinuous arterial spin labeling and accelerated 3D radial acquisition. Magn. Reson. Med. 2013;69:708–715. doi: 10.1002/mrm.24298.

89. Taschner CA, Gieseke J, Le Thuc V, Rachdi H, Reyns N, Gauvrit J-Y, Leclerc X. Intracranial Arteriovenous Malformation: Time-resolved Contrast-enhanced MR Angiography with Combination of Parallel Imaging, Keyhole Acquisition, and k-Space Sampling Techniques at 1.5 T. Radiology [Internet] 2008;246:871–879. doi: 10.1148/radiol.2463070293.

90. Xu J, Shi D, Chen C, Li Y, Wang M, Han X, Jin L, Bi X. Noncontrast-enhanced four-dimensional MR angiography for the evaluation of cerebral arteriovenous malformation: A preliminary trial. J. Magn. Reson. Imaging 2011;34:1199–1205. doi: 10.1002/jmri.22699.

91. Yu S, Yan L, Yao Y, et al. Noncontrast dynamic MRA in intracranial arteriovenous malformation (AVM): Comparison with time of flight (TOF) and digital subtraction angiography (DSA). Magn. Reson. Imaging 2012;30:869–877. doi: 10.1016/j.mri.2012.02.027.

92. Jang J, Schmitt P, Kim BY, Choi HS, Jung SL, Ahn KJ, Kim I, Paek M, Kim BS. Non-contrast-enhanced 4D MR angiography with STAR spin labeling and variable flip angle sampling: A feasibility study for the assessment of dural arteriovenous fistula. Neuroradiology 2014;56:305–314. doi: 10.1007/s00234-014-1336-0.

93. Lanzman RS, Kröpil P, Schmitt P, Wittsack HJ, Orzechowski D, Kuhlemann J, Buchbender C, Miese FR, Antoch G, Blondin D. Nonenhanced ECG-gated time-resolved 4D steady-state free precession (SSFP) MR angiography (MRA) of cerebral arteries: Comparison at 1.5 T and 3 T. Eur. J. Radiol. 2012;81. doi: 10.1016/j.ejrad.2011.06.044.

94. Winkelmann S, Schaeffter T, Koehler T, Eggers H, Doessel O. An optimal radial profile order based on the Golden Ratio for time-resolved MRI. IEEE Trans. Med. Imaging 2007;26:68–76.

95. Song HK, Dougherty L. k-Space weighted image contrast (KWIC) for contrast manipulation in projection reconstruction MRI. Magn. Reson. Med. 2000;44:825–832. doi: 10.1002/1522-2594(200012)44:6<825::AID-MRM2>3.0.CO;2-D.

96. Hee KS, Dougherty L. Dynamic MRI with projection reconstruction and KWIC processing for simultaneous high spatial and temporal resolution. Magn. Reson. Med. 2004;52:815–824. doi: 10.1002/mrm.20237.

97. Song HK, Yan L, Smith RX, Xue Y, Rapacchi S, Srinivasan S, Ennis DB, Hu P, Pouratian N, Wang DJJ. Noncontrast enhanced four-dimensional dynamic MRA with golden angle radial acquisition and K-space weighted image contrast (KWIC) reconstruction. Magn. Reson. Med. 2014;72:1541–1551. doi: 10.1002/mrm.25057.

98. Mostardi PM, Haider CR, Rossman PJ, Borisch EA, Riederer SJ. Controlled experimental study depicting moving objects in view-shared time-resolved 3D MRA. Magn. Reson. Med. 2009;62:85–95. doi: 10.1002/mrm.21993.

99. Johnson CP, Polley TW, Glockner JF, Young PM, Riederer SJ. Buildup of image quality in view-shared time-resolved 3D CE-MRA. Magn. Reson. Med. 2013;70:348–357. doi: 10.1002/mrm.24466.

100. Feng L, Xu J, Kim D, Axel L, Sodickson DK, Otazo R. Combination of Compressed Sensing, Parallel Imaging and Partial Fourier for Highly-Accelerated 3D First-Pass Cardiac Perfusion MRI. Proc. 19th Sci. Meet. Int. Soc. Magn. Reson. Med. 2011;19:4368.

101. Kim D, Dyvorne HA, Otazo R, Feng L, Sodickson DK, Lee VS. Accelerated phase-contrast cine MRI using k-t SPARSE-SENSE. Magn. Reson. Med. 2012;67:1054–1064. doi: 10.1002/mrm.23088.

102. Feng L, Grimm R, Tobias Block K, Chandarana H, Kim S, Xu J, Axel L, Sodickson DK, Otazo R. Golden-angle radial sparse parallel MRI: Combination of compressed sensing, parallel imaging, and golden-angle radial sampling for fast and flexible dynamic volumetric MRI. Magn. Reson. Med. 2013;72:707–717.

103. Han PK, Ye JC, Kim EY, Choi SH, Park SH. Whole-brain perfusion imaging with balanced steady-state free precession arterial spin labeling. NMR Biomed. 2016;29:264–274. doi: 10.1002/nbm.3463.

104. Zhao L, Fielden SW, Feng X, Wintermark M, Mugler JP, Meyer CH. Rapid 3D dynamic arterial spin labeling with a sparse model-based image reconstruction. Neuroimage 2015;121:205–216. doi: 10.1016/j.neuroimage.2015.07.018.

105. Koktzoglou I, Sheehan JJ, Dunkle EE, Breuer FA, Edelman RR. Highly accelerated contrast-enhanced MR angiography: Improved reconstruction accuracy and reduced noise amplification with complex subtraction. Magn. Reson. Med. 2010;64:1843–1848. doi: 10.1002/mrm.22567.

106. Trzasko JD, Haider CR, Borisch EA, Campeau NG, Glockner JF, Riederer SJ, Manduca A. Sparse-CAPR: Highly accelerated 4D CE-MRA with parallel imaging and nonconvex compressive sensing. Magn. Reson. Med. 2011;66:1019–1032. doi: 10.1002/mrm.22892.

107. Beatty PJ, Nishimura DG, Pauly JM. Rapid gridding reconstruction with a minimal oversampling ratio. IEEE Trans. Med. Imaging 2005;24:799–808. doi: 10.1109/TMI.2005.848376.

108. Rapacchi S, Natsuaki Y, Plotnik A, Gabriel S, Laub G, Finn JP, Hu P. Reducing view-sharing using compressed sensing in time-resolved contrast-enhanced magnetic resonance angiography. Magn. Reson. Med. 2015;74:474–481. doi: 10.1002/mrm.25414.

109. Borden JA, Wu JK, Shucart WA. A proposed classification for spinal and cranial dural arteriovenous fistulous malformations and implications for treatment. J. Neurosurg. [Internet] 1995;82:166–179. doi: 10.3171/jns.1995.82.2.0166.

110. Tsai CM, Nishimura DG. Reduced aliasing artifacts using variable-density k-space sampling trajectories. Magn. Reson. Med. 2000;43:452–458. doi: 10.1002/(SICI)1522-2594(200003)43:3<452::AID-MRM18>3.0.CO;2-B.

111. Yutzy SR, Seiberlich N, Duerk JL, Griswold MA. Improvements in multislice parallel imaging using radial CAIPIRINHA. Magn. Reson. Med. 2011;65:1630–1637. doi: 10.1002/mrm.22752.

112. Peters DC, Korosec FR, Grist TM, Block WF, Holden JE, Vigen KK, Mistretta CA. Undersampled projection reconstruction applied to MR angiography. Magn. Reson. Med. 2000;43:91–101. doi: 10.1002/(SICI)1522-2594(200001)43:1<91::AID-MRM11>3.0.CO;2-4.

113. Duyn JH, Yang Y, Frank JA, Van Der Veen JW. Simple Correction Method for k-Space Trajectory Deviations in MRI. J. Magn. Reson. 1998;132:150–153. doi: 10.1006/jmre.1998.1396.

114. Peters DC, Derbyshire JA, McVeigh ER. Centering the projection reconstruction trajectory: Reducing gradient delay errors. Magn. Reson. Med. 2003;50:1–6. doi: 10.1002/mrm.10501.

115. Tobias Block K, Uecker M. Simple Method for Adaptive Gradient-Delay Compensation in Radial MRI. Int. Soc. Magn. Reson. Med. 2011;19:2816.

116. Jackson JI, Meyer CH, Nishimura DG, Macovski A. Selection of a Convolution Function for Fourier Inversion Using Gridding. IEEE Trans. Med. Imaging 1991;10:473–478. doi: 10.1109/42.97598.

117. Barger A V., Block WF, Toropov Y, Grist TM, Mistretta CA. Time-resolved contrast-enhanced imaging with isotropic resolution and broad coverage using an undersampled 3D projection trajectory. Magn. Reson. Med. 2002;48:297–305. doi: 10.1002/mrm.10212.

118. Stehning C, B??rnert P, Nehrke K, Eggers H, D??ssel O. Fast isotropic volumetric coronary MR angiography using free-breathing 3D radial balanced FFE acquisition. Magn. Reson. Med. 2004;52:197–203. doi: 10.1002/mrm.20128.

119. Gu T, Korosec FR, Block WF, Fain SB, Turk Q, Lum D, Zhou Y, Grist TM, Haughton V, Mistretta CA. PC VIPR: A high-speed 3D phase-contrast method for flow quantification and high-resolution angiography. Am. J. Neuroradiol. 2005;26:743–749. doi: 26/4/743 [pii].

120. Chandarana H, Block TK, Rosenkrantz AB, Lim RP, Kim D, Mossa DJ, Babb JS, Kiefer B, Lee VS. Free-breathing radial 3D fat-suppressed T1-weighted gradient echo sequence: A viable alternative for contrast-enhanced liver imaging in patients unable to suspend respiration. Invest. Radiol. 2011;46:648–653. doi: 10.1097/RLI.0b013e31821eea45.

121. Cashen TA, Jeong H, Shah MK, Bhatt HM, Shin W, Carr JC, Walker MT, Batjer HH, Carroll TJ. 4D radial contrast-enhanced MR angiography with sliding subtraction. Magn. Reson. Med. 2007;58:962–972. doi: 10.1002/mrm.21364.

122. Chen L, Adluru G, Schabel MC, McGann CJ, Dibella EVR. Myocardial perfusion MRI with an undersampled 3D stack-of-stars sequence. Med. Phys. 2012;39:5204–5211. doi: 10.1118/1.4738965.

123. Wech T, Pickl W, Tran-Gia J, Ritter C, Beer M, Hahn D, Köstler H. Whole-heart cine MRI in a single breath-hold - A compressed sensing accelerated 3D acquisition technique for assessment of cardiac function. RoFo Fortschritte auf dem Gebiet der Rontgenstrahlen und der Bildgeb. Verfahren 2014;186:37–41. doi: 10.1055/s-0033-1350521.

124. Deng W, Zahneisen B, Stenger VA. Rotated stack-of-spirals partial acquisition for rapid volumetric parallel MRI. Magn. Reson. Med. 2016;76:127–135. doi: 10.1002/mrm.25863.

125. Wundrak S, Paul J, Ulrici J, Hell E, Rasche V. A Small Surrogate for the Golden Angle in Time-Resolved Radial MRI Based on Generalized Fibonacci Sequences. IEEE Trans. Med. Imaging 2015;34(6):1262–9.

126. Han F, Zhou Z, Rapacchi S, Nguyen KL, Finn JP, Hu P. Segmented golden ratio radial reordering with variable temporal resolution for dynamic cardiac MRI. Magn. Reson. Med. 2016;76:94–103. doi: 10.1002/mrm.25861.

127. Freiberger M, Knoll F, Bredies K, Scharfetter H, Stollberger R. The Agile Library for Biomedical Image Reconstruction Using GPU Acceleration. Comput. Sci. Eng. [Internet] 2013;15:34–44. doi: 10.1109/MCSE.2012.40.

128. Hansen MS, Sørensen TS. Gadgetron: An open source framework for medical image reconstruction. Magn. Reson. Med. 2013;69:1768–1776. doi: 10.1002/mrm.24389.

129. Shin PJ, Larson PEZ, Ohliger MA, Elad M, Pauly JM, Vigneron DB, Lustig M. Calibrationless parallel imaging reconstruction based on structured low-rank matrix completion. Magn. Reson. Med. [Internet] 2014;72:959–970. doi: 10.1002/mrm.24997.

130. Seiberlich N, Breuer F, Blaimer M, Jakob P, Griswold M. Self-calibrating GRAPPA operator gridding for radial and spiral trajectories. Magn. Reson. Med. 2008;59:930–935. doi: 10.1002/mrm.21565.

131. Lustig M, Pauly JM. SPIRiT: Iterative self-consistent parallel imaging reconstruction from arbitrary k-space. Magn. Reson. Med. 2010;64:457–71.

132. Bresch E, Kim YC, Nayak K, Byrd D, Narayanan S. Seeing speech: Capturing vocal tract shaping using real-time magnetic resonance imaging. IEEE Signal Process. Mag. 2008;25. doi: 10.1109/MSP.2008.918034.

133. Weiger M, Pruessmann KP, Boesiger P. Cardiac real-time imaging using SENSE. Magn. Reson. Med. 2000;43:177–184. doi: 10.1002/(SICI)1522-2594(200002)43:2<177::AID-MRM3>3.0.CO;2-1.

134. Cox RW, Jesmanowicz A, Hyde JS. Real-time functional magnetic resonance imaging. Magn. Reson. Med. [Internet] 1995;33:230–236. doi: 10.1016/j.mri.2007.02.007.

135. Holsinger AE, Wright RC, Riederer SJ, Farzaneh F, Grimm RC, Maier JK. Real-time interactive magnetic resonance imaging. Magn. Reson. Med. [Internet] 1990;14:547–53. doi: 10.1002/mrm.1910140312.

136. Uecker M, Zhang S, Voit D, Karaus A, Merboldt KD, Frahm J. Real-time MRI at a resolution of 20 ms. NMR Biomed. 2010;23:986–994. doi: 10.1002/nbm.1585.

137. Lingala SG, Zhu Y, Lim Y, Toutios A, Ji Y, Lo WC, Seiberlich N, Narayanan S, Nayak KS. Feasibility of through-time spiral generalized autocalibrating partial parallel acquisition for low latency accelerated real-time MRI of speech. Magn. Reson. Med. 2017;78:2275–2282. doi: 10.1002/mrm.26611.

138. Seiberlich N, Lee G, Ehses P, Duerk JL, Gilkeson R, Griswold M. Improved temporal resolution in cardiac imaging using through-time spiral GRAPPA. Magn. Reson. Med. 2011;66:1682–1688. doi: 10.1002/mrm.22952.

139. Sørensen TS, Atkinson D, Schaeffter T, Hansen MS. Real-time reconstruction of sensitivity encoded radial magnetic resonance imaging using a graphics processing unit. IEEE Trans. Med. Imaging 2009;28:1974–1985. doi: 10.1109/TMI.2009.2027118.

140. Majumdar A, Ward RK, Aboulnasr T. Compressed sensing based real-time dynamic MRI reconstruction. IEEE Trans. Med. Imaging 2012;31:2253–2266. doi: 10.1109/TMI.2012.2215921.

141. Uecker M, Zhang S, Frahm J. Nonlinear inverse reconstruction for real-time MRI of the human heart using undersampled radial FLASH. Magn. Reson. Med. 2010;63:1456–1462. doi: 10.1002/mrm.22453.

142. Xie J, Xu L, Chen E. Image Denoising and Inpainting with Deep Neural Networks. Nips [Internet] 2012:1–9.

143. Dong C, Loy CC, He K, Tang X. Image Super-Resolution Using Deep Convolutional Networks. IEEE Trans. Pattern Anal. Mach. Intell. 2014;38:295–307. doi: 10.1109/TPAMI.2015.2439281.

144. Schlemper J, Caballero J, Hajnal J V., Price A, Rueckert D. A Deep Cascade of Convolutional Neural Networks for MR Image Reconstruction. Inf. Process. Med. Imaging 2017:647–658. doi: https://doi.org/10.1007/978-3-319-59050-9_51.

145. Kulkarni K, Lohit S, Turaga P, Kerviche R, Ashok A. ReconNet: Non-Iterative Reconstruction of Images from Compressively Sensed Random Measurements. 2016. doi: 10.1109/CVPR.2016.55.

146. Kelly B, Matthews TP, Anastasio MA. Deep Learning-Guided Image Reconstruction from Incomplete Data. 2017.

147. Hyun CM, Kim HP, Lee SM, Lee S, Seo JK. Deep learning for undersampled MRI reconstruction. 2017:1–11.

148. Zhao H, Gallo O, Frosio I, Kautz J. Loss Functions for Image Restoration with Neural Networks. IEEE Trans. Comput. Imaging [Internet] 2017;3:47–57. doi: 10.1109/TCI.2016.2644865.

149. Yann L. Efficient backprop. Neural networks: tricks of the trade 1998;53:1689–1699. doi: 10.1017/CBO9781107415324.004.

150. He K, Zhang X, Ren S, Sun J. Delving deep into rectifiers: Surpassing human-level performance on imagenet classification. In: Proceedings of the IEEE International Conference on Computer Vision. Vol. 2015 International Conference on Computer Vision, ICCV 2015. ; 2015. pp. 1026–1034. doi: 10.1109/ICCV.2015.123.

151. Kingma DP, Ba JL. Adam: a Method for Stochastic Optimization. Int. Conf. Learn. Represent. 2015 2015:1–15. doi: http://doi.acm.org.ezproxy.lib.ucf.edu/10.1145/1830483.1830503.

152. Ronneberger O, Fischer P, Brox T. U-Net: Convolutional Networks for Biomedical Image Segmentation. Miccai 2015:234–241. doi: 10.1007/978-3-319-24574-4_28.